Design and Construction of an Optical Polarimeter for the Study of Ice-like Analogs using Near Zero Phase Angle Measurements

Mrunal Amin

A Thesis submitted to the Faculty of Graduate Studies in Partial Fulfillment of the Requirements for the Degree of
Masters of Science

Graduate Program in Science
York University
Toronto, Ontario

September 2018

Abstract

Previous studies for analog samples measuring polarized backscatter near zero phase angles have suggested strong presence of multiple scattering effects. Radar data for Mercury, Moon and other icy Galilean satellites exhibit high circular polarization ratios with decreasing phase angle that indicates the possible presence of icy deposits in the polar craters. An examination of powder samples with known composition and grain sizes was undertaken to try and further understand the interaction of polarized light with closely packed particulate medium. The goal of this research was to construct and test a long arm Goniometric optical instrument capable of measuring polarization ratios in the range from 0-5 degree phase angle for understanding and differentiating the scattering effects that occur near zero phase angle. Measuring signal intensity and circular polarization ratios with the newly setup optical polarimeter for various analog samples will provide a framework for understanding the characteristics of embedded scatterers within the icy regoliths.

Dedication

Dedicated to my grandparents and parents who taught me I could do anything I put my mind to, And to Mansi, for being there to remind me they were right

Acknowledgments

First and foremost, with immense gratitude I would like to thank the help of my supervisor Professor Michael Daly, Associate Professor in the Department of Earth and Space Science and Engineering and co-supervisor Professor Regina Lee, Associate Professor in the Department of Earth and Space Science and Engineering at York University, as well as their steadfast support over the course of this project. I would like to thank Dr. David T. Blewett, Applied Physics Laboratory at John Hopkins University for providing previous data, analog samples and continuous support throughout the research.

To all my fellow colleagues, I would like to convey my deepest appreciation for all the support and encouragement throughout my project. I am highly grateful to Kati Balachandran, Undergraduate at York University for all the help assembling the instrument. Special thanks to Amy Shaw for teaching and guiding me on the Goniometric instrument.

I would like to express my gratitude to all my teachers at York University who put their faith in me and urged me to do better.

Table of Contents

List of Figures

List of Tables

List of Acronyms

CBOE Coherent Backscattering Opposition Effect

CPR Circular Polarization Ratio

DOCP Degree of Circular Polarization

DOP Degree of Polarization

LHCP Left Handed Circular Polarization

LP Linear Polarizer

LPR Linear Polarization Ratio

LRO Lunar Reconnaissance Orbiter

MAGI Multi-Axis Goniometric Instrument

Mini-RF Miniature Radio Frequency

Nd:YAG Neodymium-Doped Yttrium Aluminum Garnet

NDF Neutral Density Filter

OC Opposite Circular Polarization state

QWP Quarter Wave Plate

RHCP Right Handed Circular Polarization

RQWP Rotating Quarter Wave Plate

SC Same Circular Polarization state

SHOE Shadow Hiding Opposition Effect

1 Introduction

1.1 Historical Summary

Radar remote sensing is an important tool for probing the surface and sub-surface features of Solar System bodies for possible presence of water ice. [10] Planetary radar techniques have been able to differentiate radar scattering properties between dry/rocky surfaces of inner Solar system bodies and their polar regions. Regions such as the poles of Mars, polar craters of Mercury, Earth glaciers and icy Galilean satellites of Jupiter exhibit high radar reflectivity compared to the low quasi-specular reflections from rough surfaces. [40] The main differentiating factors present among the highly reflective radar data for polar regions and rocky regions are the differences in the linear polarization ratios and circular polarization ratios. Circular polarization ratio (CPR) indicates the difference in power received in the same sense of polarization as incident versus the power received in the opposite sense of polarization for the region under study. Linear polarization ratio (LPR) is the ratio of the reflectance in the cross-polarized sense to that in the same-polarized sense as incident. Single scattering causes a flip in the polarization state of the incident signal, whereas multiple scattering tends to randomize the polarization state often causing the return signal to be polarized in the same sense as incident. The differences in radar data for polar and rocky regions are explained by observing polarization ratios for different types of scattering. The most plausible explanation for high polarization ratios is volume scattering within a weakly absorbing medium in which embedded scatterers are of the sizes close to the radar wavelength. As ice weakly absorbs the incoming radiation at planetary radar wavelengths the voids, cracks, density variations or rocks would act as

scatterers. Incident radiation on an icy surface with embedded scatterers would undergo multiple scattering within the medium and emerge coherently to produce high reflectance values. The coherent enhancement from such regions would occur at near zero phase angle due to the opposition effects.

The presence of ice in the permanently shadowed crater regions of Mercury was confirmed from the radar bright, high CPR data collected by Slade and Butler. [9] The thermal models from Paige [41] suggested that temperatures in the permanently shadowed regions of Mercury would be cold enough to trap volatiles over geological time periods which were confirmed from polar topography data that are consistent with long term retention of water ice. [41]. Further, active measurements of surface reflectance by the laser altimeter reveal areas of high and low reflectance consistent with the presence of surface ice in radar bright regions. Intuitively lunar shadowed polar regions would be considered as favorable sites for possible presence of ice due to their distance from Sun but the data is ambiguous. [31] Radar observations of lunar polar regions does not reveal areas with strongly elevated returns and CPR similar to Mercury. Many groups have reported studies of permanently shadowed polar regions that are visible to Earth based radar with high CPR values, but they were found to occur both, within and outside the permanent shadowed region. [19] [48] This raises the question whether rough, blocky ejecta or water ice is responsible for CPR enhancement.

1.2 Research Context

The objective of this study is to conduct a series of optical scaled radar measurements designed to explore key variables that contribute to the backscattering of electromagnetic radiation from icy deposits. This can be achieved by examining the key differences in the opposition effects for highly reflective analogs by observing reflectance and polarization ratio trends.

Variables such as reflectance and circular polarization ratios for various planetary bodies such as the Moon, Mars, Jupiter and Titan have been observed through radar

data. [40] [36] [27] Analog samples measuring the same variables have been observed from 0.05 - 5 degree phase angle range for highly reflective alumina samples. [37] Conducting an experimental setup capable of measuring signal intensity and CPR values of analog samples to an exact zero phase angle, would enable us to better understand the contribution of opposition effects to the CPR and reflectance phase curves. The main goal of this study is to construct a polarimeter capable of measuring polarized returns from samples similar to that from previous studies and observe any discrepancies. With the newly setup zero phase angle (defined as the angle between the observer, the observed object and the incident light) polarimeteric instrument we can further analyze different grain sizes of highly reflective and liquid samples. Polarized returns from polystyrene beads suspended in a liquid medium will provide important information regarding the size distribution of scatterers, number density of scatterers, absorption properties of the medium and absorption properties of the scatterers.

Further work into mapping out the effects of scatters and the scattering medium will provide a framework for interpreting planetary radar observations of ice-bearing and potentially ice bearing deposits. This research will help constrain factors such as the purity of ice and abundance, kind and size distribution of scatterers responsible for coherent effects. Through this research we will be able to lay a platform for integrating laboratory results from analog samples with mono and bistatic radar data for lunar polar regions acquired by Mini-RF instrument [45] on the Lunar Reconnaissance Orbiter (LRO) spacecraft for better understanding of the nature of lunar areas that may contain ice deposits. [47] [16]

Previous studies by Nelson and Hapke [37], [38], [23] involved measuring reflectance in eight senses of polarization states and summing them to calculate the linear and circular polarization ratios. In this research the Stokes parameter of the backscatter signal will be calculated that provides all the information regarding the reflectance and polarization state of the signal. This method reduces the time taken for individual observations allowing for precise polarization measurements.

1.3 Research Objectives

The primary objective of this research is to construct an experimental apparatus that is capable of measuring signal intensity and polarization state of the backscattered signal near zero phase angles. We will validate the constructed polarimeter by comparing acquired data with previous analog data. The research will help us understand the polarized backscatter returns for analog samples. This would allow future studies to constrain factors such as the purity of ice and the kind, abundance and size distribution of scatterers responsible for high polarized near zero phase returns. Future work on integration of laboratory analog data with mono and bistatic radar data for lunar polar regions collected by the Mini-RF instrument on the LRO spacecraft would be highly beneficial. [45] [47]. The research will allow for better understanding in the nature of lunar areas that may contain ice and possibly help in re-interpreting published radar data for Mercurian deposits [9]. The key objectives to be achieved throughout this research are divided into primary and secondary goals listed as follows.

Primary Objectives:

1. Design an optical platform capable of measuring off-axis polarized backscatter measurements from analog samples.

2. Construct and re-iterate the design of the optical polarimeter to achieve objectives 3-6.

3. The instrument shall be capable of measuring the polarization state of the backscatter.

4. The instrument shall be capable of taking measurements from 0-5 degree phase angle.

5. The polarimeter shall be capable of acquiring measurements at exact zero phase angle.

6. Important parameters such as Linear Polarization Ratio (LPR) and Circular Polarization Ratio (CPR) shall be computed from the backscatter data.

7. Validate the constructed polarimeter by comparing CPR measurements with previous undertaken studies on analog samples.

Secondary Objectives:

1. Compute and observe CPR vs phase angle measurements for different analog sample grain sizes.

2. Compute and observe signal intensity vs phase angle measurements for different grain sizes.

3. Provide interpretations of the observed CPR and intensity phase curves.

4. Explore scattering effects responsible for backscattering from two different categories of analog samples; powdered samples and suspended beads in a liquid medium.

2 Theoretical Background

The radar scattering properties of the icy satellites have been controversial for over a decade as remote sensing remains the only way to obtain information about their surfaces. The highly reflective radar backscattering properties of the icy satellites at zero phase angles are associated with opposition effects namely Coherent Backscatter Opposition Effect (CBOE) and the Shadow Hiding Opposition Effect (SHOE). The physical cause for CBOE is due to the enhancement of radar brightness near zero phase angle by volume scattering within a low-loss medium. The magnitude and shape of the opposition peak depends on the properties of the surface such as particle size, porosity and scattering behaviour of the individual regolith particles. There have been a number of studies undertaken to determine the nature of opposition effects for icy analogs by observing the polarization state of the backscattered signal. [23]

2.1 Stokes Parameters

The polarization state of an electromagnetic radiation can be described through a vector containing four parameters called the Stokes parameters. The Stokes parameters were defined by George Gabriel Stokes in 1852 [14], where amplitudes E_x and E_y are the orthogonal components of the total electric field :

$$R = E_x^2 + E_y^2$$

$$Q = E_x^2 - E_y^2$$

$$U = 2 * E_x E_y cos(\delta_y - \delta_x)$$

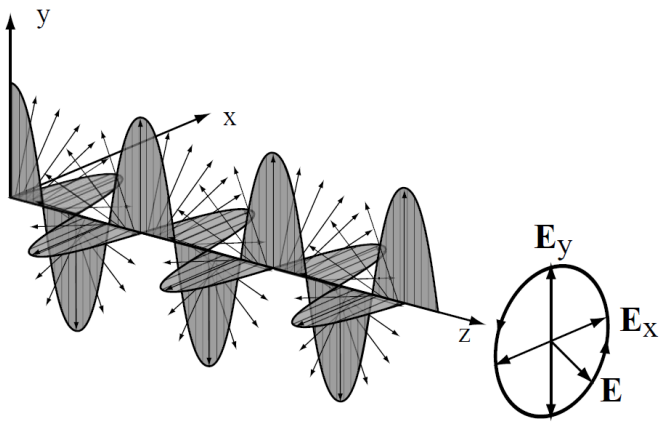

Figure 2.1: Schematic representation of a Left Handed Circularly Polarized Wave [32]

$$V = 2 * E_x E_y sin(\delta_y - \delta_x)$$

With the squared of the amplitude of the electric field being proportional to the irradiance, I. The Stokes parameters can be represented as follows:

$$S_0 = R = I_x + I_y$$

$$S_1 = Q = I_x - I_y$$

$$S_2 = U = I_{+45^\circ} - I_{-45^\circ}$$

$$S_3 = V = I_r - I_l$$

Where $I_{x,y,+45^\circ,-45^\circ,r,l}$ represents the irradiance for the polarized light according to figure 2.2. The first parameter of the Stokes vector R is the total irradiance measured in W/m^2. The second parameter of the Stokes vector Q, describes the linear polarization state in the x-direction when the value is positive and in the y-direction when the value is negative. U represents the state of polarization in +45°and -45°direction when it is positive and negative, respectively. The last parameter V describes the state of right and left circularly polarized wave when the value is positive and negative respectively. [32]

From the Stokes parameters we can determine many useful quantities such as the degree of polarization (DOP) and degree of circular polarization (DOCP).

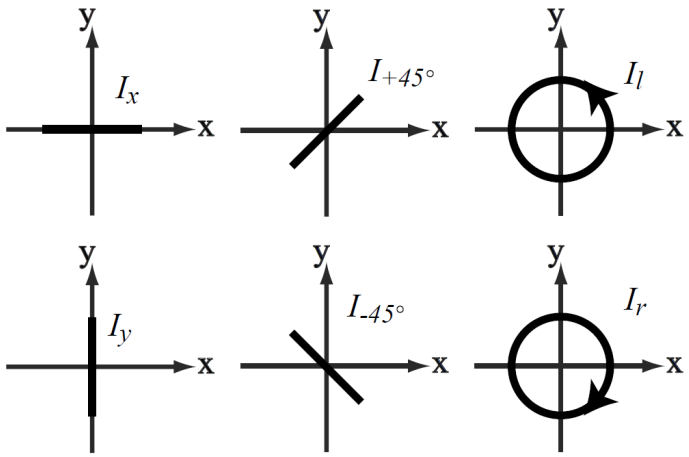

Figure 2.2: Six polarization states of a light source represented with their respective Irradiances for calculating the Stokes parameters [32]

$$Degree of Polarization = \frac{\sqrt{Q^2 + U^2 + V^2}}{R}$$

$$Degree of Circular Polarization = \frac{V}{R}$$

2.2 Polarization Ratio

2.2.1 Linear Polarization Ratio

The linear Polarization Ratio is the ratio of the received intensity in the x-axis direction to that in the y-axis direction, for an observer viewing the scattered signal in the z-axis direction.

$$\mu_L = \frac{I_{LO}}{I_{LS}}$$

For an incident signal propagating through the negative z-axis and scattering back in the positive z-axis direction, I_{LS} is the component of the radiance scattered with its electric field vector in the same direction as that of incident light while I_{LO} is the component scattered with its electric vector in the orthogonal state (90°to incident). [32] The examples

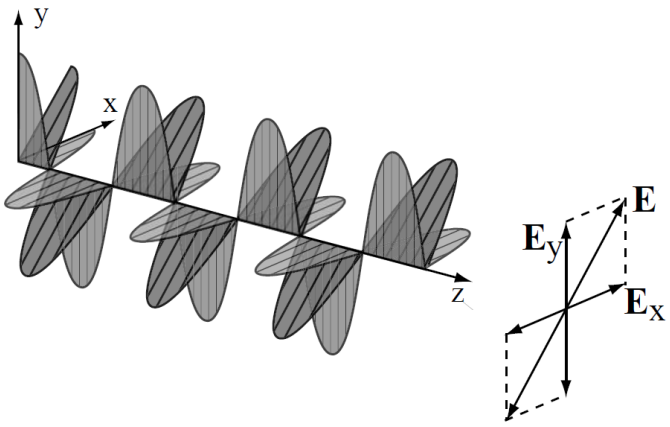

Figure 2.3: Schematic representation of a Linearly polarized wave [32]

of perfectly linear horizontally polarized light and linear vertically polarized light that can be observed from the linear polarizer are represented in terms of Stokes parameters as follows:

$$S_{LHP} = R \begin{Bmatrix} 1 \\ 1 \\ 0 \\ 0 \end{Bmatrix}; S_{LVP} = R \begin{Bmatrix} 1 \\ -1 \\ 0 \\ 0 \end{Bmatrix}$$

2.2.2 Circular Polarization Ratio

The Circular Polarization Ratio (CPR) is defined as the ratio between power reflected in the same circular polarization state (SC) as that transmitted and the power reflected in the opposite circular polarization state (OC) as that transmitted. [13] [7] The circular polarization ratio (μ_c) can be represented in terms of Stokes vector as shown in the equation below:

$$\mu_c = \frac{S_0 - S_3}{S_0 + S_3} = \frac{R - V}{R + V}$$

CPR is often the most important physical observable as it provides the best indications for wavelength-scale complexity of the surface. Typical values for CPR vary between 0 and 1, where 0 represents single bounce/mirror/specular reflection and 1 indicates a highly rough surface. Values greater than 1 are observed when there is wavelength scale roughness or presence of ice. The values are strongly modulated by roughness induced changes in scattering on or beneath the target surface. [10] [50]

For any rocky planetary body, understanding the plausible scattering geometries are directly relevant for interpreting the processes that form and modify the surface or regolith. Observing the changes in polarization ratios can explain how various geologic attributes such as rock or plate sizes, shapes, proximity, volume distribution may contribute to a strong CPR enhancement. [23]

Water ice that occurs in sheets or slabs, at least a few radar wavelengths in thickness, has very strong radar backscatter and enhanced CPR values. This behaviour arises due to scattering by sub-surface discontinuities in the ice which have intrinsically low loss. In a medium containing scatterers separated by distances in the order of wavelength, parts of waves that multiply scatter between the particles traverse the same path in opposite directions and combine coherently in the backscattering direction. [6]

2.2.3 Examples of Polarization Ratios

The polarization ratios reveal important information regarding roughness, different properties of embedded scatters and types of scattering. In this section we shall summarize some examples of polarization ratios observed by radar and analog measurements. Radar observations were performed on various solar system bodies such as Mercury, Moon and asteroids [8]. Analog polarization studies were performed for different powdered samples (alumina oxide, iron oxide, calcium carbonate) [42] and ice analogs [28].

Analog Sample Polarization

In a study conducted by R. Nelson and B. Hapke, they observed the relative reflectance and CPR values for various grain sizes of alumina samples. [37] A long arm goniopolarimeter was used by the author to acquire these measurements with the wavelength of illuminating radiation being 0.633 μm. The CPR values of alumina grain sizes at zero phase angle and the relative reflectance compared to standard reference Spectralon sample at 5°are shown below with their measurement errors:

The polarimetric apparatus used by Nelson consisted of an off-axis analyzer setup which is capable of measuring reflectance from 0.05°- 5°phase angle. The apparatus used different orientations of linear polarizers and quarter wave plates to observe the polarization state of the propagating signal. The CPR measurements from Nelson's paper shown in Table 2.1, suggests that the highest values are observed for particle sizes that are within a few wavelengths of the incident radiation. Higher reflectance values are observed for particles sizes closer to the wavelength while low reflectance values are observed for sizes much smaller to larger than the incident wavelength.

Reflectance and CPR for Alumina Samples at 0°phase angle		
Particle Size (μm)	Reflectance Relative to Spectralon at 5°	CPR
0.1	100.76 ± 0.14	1.19 ± 0.05
0.5	102.70 ± 0.65	1.19 ± 0.05
1.0	102.5 ± 1.68	1.29 ± 0.05
1.2	104.05 ± 0.71	1.25 ± 0.05
1.5	102.70 ± 0.86	1.3 ± 0.05
2.1	99.11	1.52 ± 0.05
3.2	98.61 ± 0.28	1.48 ± 0.05
4.0	97	1.39 ± 0.05
5.75	95.6 ± 1.24	1.31 ± 0.05
7.0	94.6 ± 0.7	1.31 ± 0.05
12.14	90.93 ± 1.2	1.28 ± 0.05

Table 2.1: Reflectance and CPR analog data for different grain sizes of Alumina samples observed by Nelson [38]

Radar Circular Polarization

The Green Bank Telescope measured and documented the Lunar radar data from the 12.6 cm [11] and 70 cm [12] radar transmitter located at the Arecibo Observatory. The highest CPR values were observed in the walls, floors and proximal ejecta blankets of impact craters. The roughness of the crater walls and floors are due to presence of rocky debris or lava-like impact melt sheets. The proximal ejecta are comprised of abundant surface boulders, rocks suspended within fine grained regolith and patches of rough impact melt. [10] The LPR and CPR values for the lunar radar data for the region of Southwestern Montes Cordillera deposits of Orientale Basin are shown in the figure below:

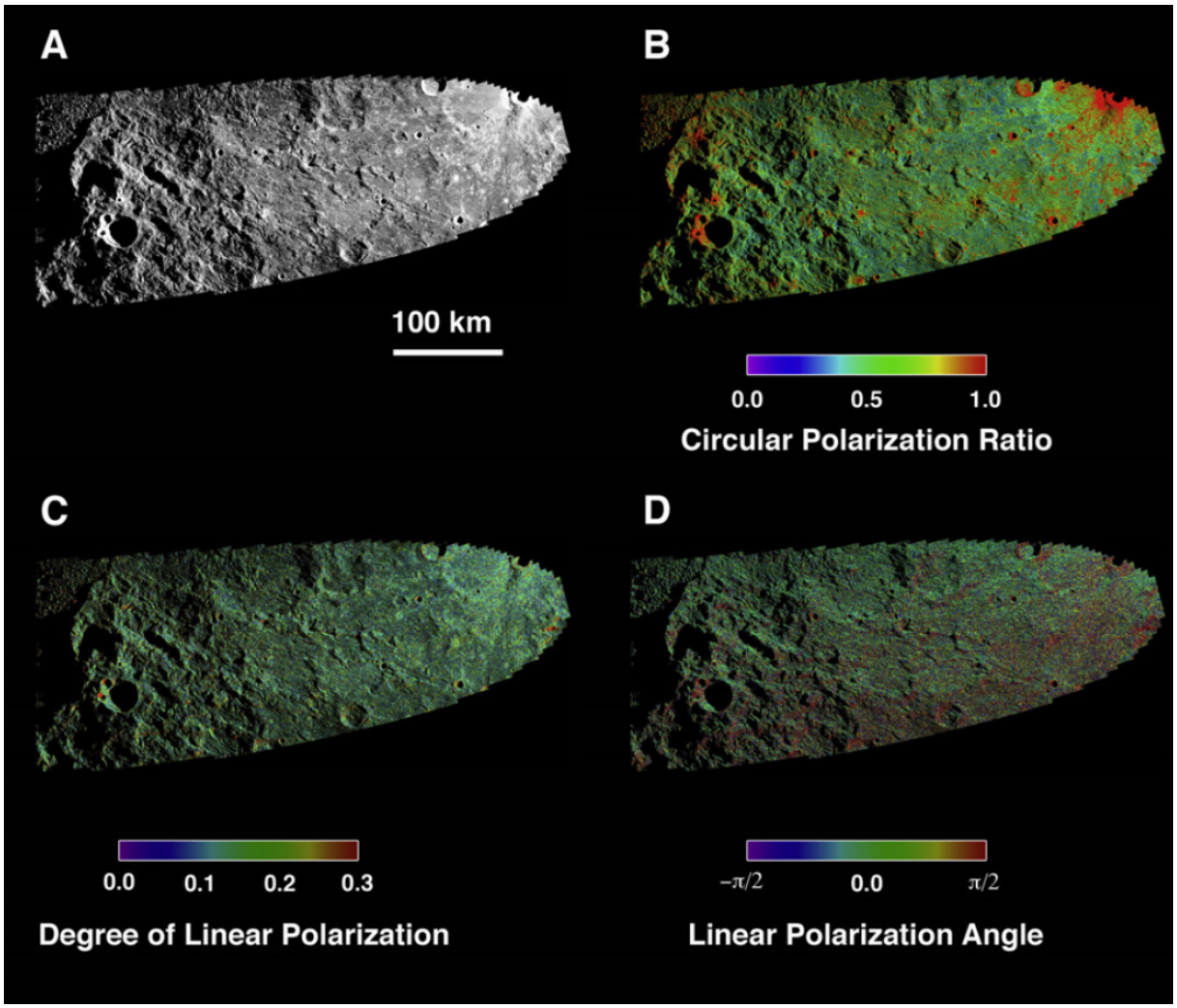

Figure 2.4: Example of (A) 12.6 cm radar image of the southwestern Montes Cordillera deposits of Orientale basin region. (B) Circular polarization ratio (C) Degree of linear polarization (D) Linear polarization angle [11]

Crater Circular Polarization

CPR values for the lunar impact craters were analyzed using the Miniature Radio Frequency (Mini-RF) radar data from the Lunar Reconnaissance Orbiter (LRO) mission. [47] The CPR data for interior and exterior crater regions are shown in the table below:

Lunar Crater		Interior CPR				Exterior CPR			
Name	Location	μ	σ	γ_1	γ_2	μ	σ	γ_1	γ_2
Hermite B	87.14°N, 86.2°W	0.97	0.50	1.75	6.12	0.60	0.33	1.95	7.70
Rozhdestvenskiy N	84°N, 156.5°W	0.93	0.50	1.83	7.66	0.57	0.35	2.63	12.42
Main L	81.44°N, 22.73°E	0.92	0.48	1.82	7.06	0.88	0.45	1.76	6.60
Schomberger A	78.61°S, 23.52°E	0.99	0.50	1.77	6.51	1.03	0.51	1.78	7.23
Cardanus E	12.8°N, 70.8°W	0.83	0.46	2.19	7.19	0.55	0.33	2.11	7.28
Byrgius C	21.2°S, 64.5°W	1.12	0.59	1.88	7.33	0.77	0.43	2.03	8.86
Dollond E	10.26°S, 15.7°E	1.00	0.53	1.85	7.00	0.93	0.50	1.93	7.47
Stevinus A	31.86°S, 51.65°E	1.04	0.56	1.93	7.95	0.99	0.53	2.06	12.11
μ: mean, σ: standard deviation, γ_1: skewness, γ_2: kurtosis									

Table 2.2: CPR values for interior and exterior Lunar crater regions from the LRO mission [16]

Among several craters observed some were selected and classified into four categories based on location and CPR characteristics by Cai as presented below: [16]

- Polar Anomalous Craters

  Hermite B is a typical anomalous crater that is located on the northern floor of crater Hermite. LRO Diviner radiometer observed that night temperatures for the southwest edge can be as low as 25 K making it the coldest place on the Moon. Due to low temperatures and permanent Sun shadow this region might be the most probable place to find ice. The interior of the crater has CPR value of 0.97 which is much higher than the CPR value of 0.60 in the outer region. Another significant change in CPR is observed in the low incident angle crater walls that tilt towards

the radar which corresponds to large SC and OC scatter resulting in a smaller CPR value. [16]

- Non-Polar Anomalous Craters

  Cardanus E is a bowl-shaped crater that is located close to the Southwest edge of Oceanus Procellarum. The crater has varying thermal conditions due to which water ice is not expected to stay stable within this region. This is reflected in the CPR values (Interior CPR =0.83, Exterior CPR = 0.55) which are lower than the polar anomalous crater regions. The large CPR differences in the interior to exterior regions are due to the slope of the crater wall which varies from 20°to 30°. The radar echoes for the crater that tilt towards the radar are twice as those for the entire interior region while echoes from crater walls that tilt away are one-third as those for interior region. [16]

- Polar Fresh Craters

  Main L is a bowl-shaped fresh crater that is located in the North Polar Region with most of its portions covered in permanent shadow except portions of the Northern rim. The CPR values for the interior (CPR = 0.92) and exterior regions (CPR = 0.88) are in close proximity to each other. The correlation between radar echo strengths and local incidence angles are very strong where large incidence angles have lower radar returns while smaller incidence angles have large radar returns and higher CPR. [16]

- Non-polar Fresh Craters

  Dollond E is a bowl-shaped crater located to the west of Mare Nectaris with significantly high CPR values in both its interior (CPR = 1.0) and exterior (CPR = 0.93) regions. The crater has high elevation differences and the slope of crater wall varies from 20°-35°. Due to these parameters we observe high CPR in comparison to the other craters types. [16]

The presented crater polarization data suggests that the primary factor for elevated CPRs in the interior regions of the anomalous craters were attributed to icy deposits due to its correlations with Lunar Prospector neutron data and thermal conditions like cold traps and permanent shadowing. The CPR values of the lunar surface depended on various parameters such as, radar frequency, incidence angle, surface roughness, surface slope, dielectric constant, size and shape of surface and sub-surface rocks and regolith thickness. Theoretical simulations from the paper suggests that from all the parameters that influenced polarization data, radar incidence angle was the most prominent factor that influenced radar echo strength and CPR value. [17] While taking the slope of crater wall into account the mean CPR of the interior region was much higher than the exterior region for anomalous crater. For fresh craters the mean CPR for crater wall that tilted towards the radar (small incidence angle) was smaller than that of the exterior region which suggests that slope of the crater wall plays an important role in determining the CPR value. In observation the polar anomalous craters had higher CPR values than the non-polar regions indicating presence of water ice however newly formed craters also possessed a higher CPR value due to the crater sloping and changes in incidence angles. Hence we can say that high CPR parameter was not only a function of icy versus non-icy regions but also depended on radar configuration and surface properties. [16]

2.3 Mueller Matrix

The polarization of light provides valuable information regarding the physical state of an optical component. [25] In high precision polarimetry, it is important to calibrate the instrumental polarization of the observing system with required accuracy. The characterization of optical components can be achieved by measuring the Mueller matrices of optical elements. A Mueller matrix is a 4 x 4 real valued matrix that characterizes the optical properties of the sample by the interaction of polarized light in either reflection or transmission configurations. [32]

The polarization state of an electromagnetic wave can be determined by measuring the Stokes vector of the signal. The electromagnetic wave would have a different emerging polarization when propagating through an optical element either by transmission reflection or combination of both. The matrix method used to determine the output polarization of an electromagnetic wave represented by a Stokes vector is called Mueller calculus. [43]

For an electromagnetic wave with initial polarization state S_i propagating through an optical component with M, Mueller matrix would have the output polarization state S_o represented as Stokes vector [43]

$$S_o = MS_i$$

The above expression can be written in matrix form as follows, where $[I, Q, U, V]$ are Stokes parameters and $M_{ij}; i, j = 1, 2, 3, 4$ are non-normalized Mueller matrix elements.

$$\begin{bmatrix} I_o \\ Q_o \\ U_o \\ V_o \end{bmatrix} = \begin{bmatrix} M_{11} & M_{12} & M_{13} & M_{14} \\ M_{21} & M_{22} & M_{23} & M_{24} \\ M_{31} & M_{32} & M_{33} & M_{34} \\ M_{41} & M_{42} & M_{43} & M_{44} \end{bmatrix} \begin{bmatrix} I_i \\ Q_i \\ U_i \\ V_i \end{bmatrix}$$

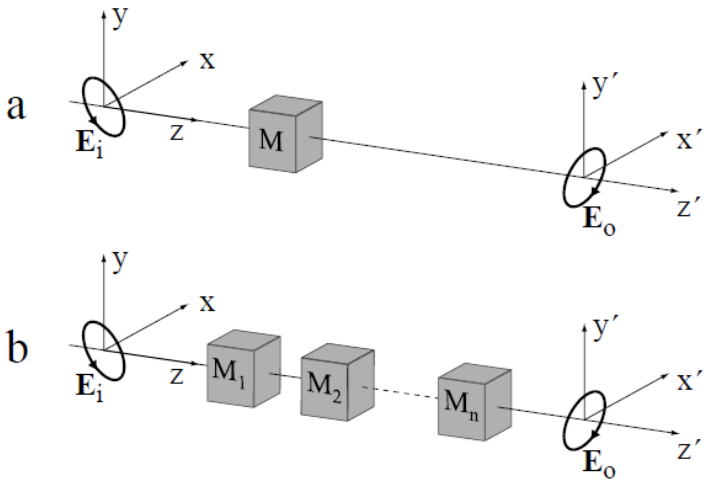

Figure 2.5: An electromagnetic wave interacting with (a) single and (b) multiple cascading optical systems with M, Mueller matrices.E_i and E_0 indicates the input and output polarization ellipse of the wave [32]

When an electromagnetic wave interacts with several optical systems in cascade as shown in figure 3.1, the polarization ellipse or Stokes vector of the emerging wave can be calculated as

$$E_o = M_n ... M_2 M_1 E_i$$

The absolute Mueller matrix elements are calculated by normalizing the Mueller matrix with its first element, $m_{ij} = M_{ij}/M_{11}$. The Normalized Mueller matrix are often used when calculating the output Stokes parameter from the input polarization state. [20]

2.3.1 Examples of Mueller Matrices for Optical Components

The Mueller matrices for a variety of optical components used in this study are listed below:

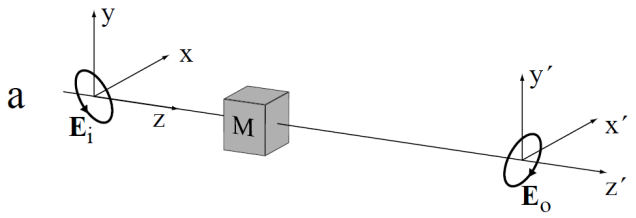

Figure 2.6: Change in polarization ellipse of an incoming radiation E_i when interacting with an optical component represented by M, Mueller matrix [32]

Linear Polarizer

The linear polarizer decreases the amplitude of the electric field in two orthogonal directions of an electromagnetic wave without changing its phase. [32] The Mueller matrix for a linear polarizer M_{LP} is:

$$M_{LP} = \frac{1}{2}\begin{bmatrix} p_x^2 + p_y^2 & p_x^2 - p_y^2 & 0 & 0 \\ p_x^2 - p_y^2 & p_x^2 + p_y^2 & 0 & 0 \\ 0 & 0 & 2p_x p_y & 0 \\ 0 & 0 & 0 & 2p_x p_y \end{bmatrix}$$

Where p_x and p_y are the real-valued amplitude transmission coefficients along orthogonal transmission axis with their values ranging between 0-1. If one of the transmission coefficients are zero we have an ideal linear polarizer in the axis orthogonal to the zero coefficient.

Retarder

The retarder causes a phase shift in the electric field between two orthogonal direc-

tions of an electromagnetic wave. The retarder comprises of slow axis with longer optical path length than the fast axis which results in a phase shift. There are generally two types of retarders, quarter wave retarder (90°retardation) and half-wave retarder (180°retardation). [32] [43] The Mueller matrix for a retarder M_R is:

$$M_R = \begin{bmatrix} 1 & 0 & 0 & 0 \\ 0 & 1 & 0 & 0 \\ 0 & 0 & cos\delta & sin\delta \\ 0 & 0 & -sin\delta & cos\delta \end{bmatrix}$$

Reflecting Surface

A specular reflecting surface such as a mirror causes the incident polarization to change its state to the opposite polarization state. When observing the arms of a wrist watch in the mirror moving clockwise we see that the watch reflection appears to be moving in anti-clockwise direction. Similar results are expected when an electromagnetic wave with right circular polarization is incident on a specular surface where the emerging polarization would be in the opposite left circular polarization, for linearly polarized light the polarization state remains the same after reflection. [32] The Mueller matrix for a specular reflecting surface such as mirror M_{MR} is:

$$M_{MR} = \begin{bmatrix} 1 & 0 & 0 & 0 \\ 0 & 1 & 0 & 0 \\ 0 & 0 & -1 & 0 \\ 0 & 0 & 0 & -1 \end{bmatrix}$$

No Sample

The Mueller matrix of an electromagnetic wave propagating without any reflection or interference is an identity matrix often represented as $m_{ij}^{'} = \delta_{ij} i_0$ where δ_{ij} is the Kronecker delta function. The no sample measurement configuration is used in the instrument calibration procedure where the polarimeter is operated with straight-through signal propagation. [20] The Mueller matrix for a no sample setup M_C is:

$$M_C = \begin{bmatrix} 1 & 0 & 0 & 0 \\ 0 & 1 & 0 & 0 \\ 0 & 0 & 1 & 0 \\ 0 & 0 & 0 & 1 \end{bmatrix}$$

2.4 Opposition Effects

The surge in brightness of a particulate medium observed near zero phase angle is called the opposition effect. [23] The opposition effect was first noted by Seeliger [21] on Saturn's rings and has since been observed on a variety of bodies including the Moon, Mars, asteroids, planetary satellites and terrestrial materials.

When observing a particulate medium at the same angle as the incidence angle of the light source there is a surge in brightness that can be attributed to the opposition effect. These effects are also observed around terrestrial regions such as forests, grass fields and deserts when the sun is directly overhead the observer. [22]

The existence of the opposition surge were first described by Tom Gehrels during his study of the reflected light from the asteroid. [18] Suggestions such that the coherent backscatter causes the opposition effects for the solar system bodies at visual wavelength and coherent effect might also account for the negative branch of polarization for planetary bodies are plausible. [35] However because the solar system objects are illuminated with natural sunlight that is unpolarized, the astronomical opposition effects have ambiguous interpretations. [24]

2.4.1 Shadow Hiding Opposition Effect

The opposition effect causing a sharp surge in brightness of an astronomical object observed near zero phase angle has generally been explained by Shadow hiding (SHOE). SHOE results when particles in a planetary regolith cast shadows on adjacent particles; those shadows are visible at larger observation angles but as we get progressively closer to the incidence angle, the shadows are hidden beneath the particles that cast them causing the regolith to appear brighter. [24]

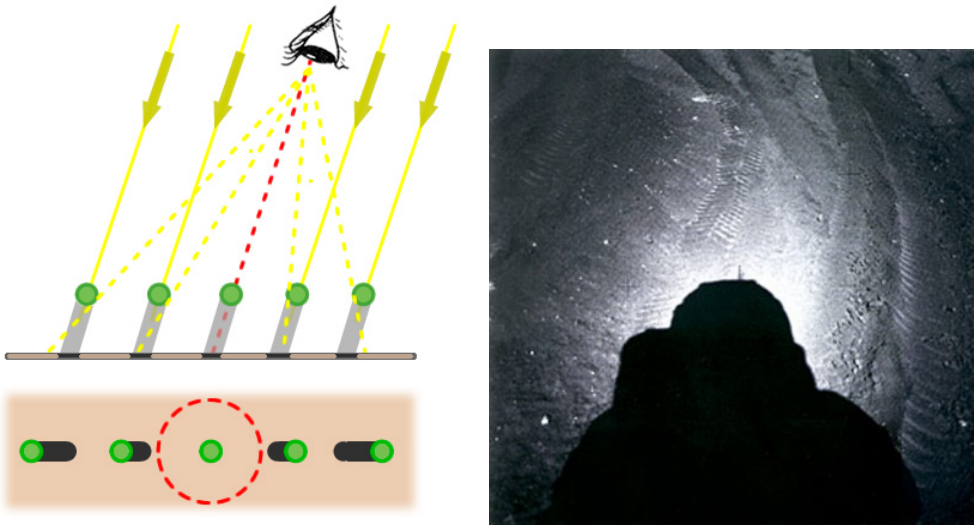

(a) Schematic of the SHOE (b) Example of the SHOE

Figure 2.7: (a) Shadows cast by the particles from the sun are not visible to the observer with Sun overhead, causing the area to appear brighter [15] (b) Example of SHOE, taken by Apollo 17 astronaut Eugene Cernan on the lunar surface [30]

From figure 2.7 we can observe that for larger observation angle the sample would appear to be darker as the particles casted shadows on the neighboring particles. Observing the sample at zero phase angle, the sample would appear brighter and result in larger reflectance values.

2.4.2 Coherent Backscattering Effect

The Coherent Backscattering Opposition effect (CBOE) also known as weak photon localization through time reversal symmetry [3] is based on the fact that portions of wave fronts that are multiple scattered within a nonuniform medium follow the same path, but those in opposite directions combine constructively at zero phase angle to produce a brightness peak. The CBOE is most prominent when the particles are of the order of wavelength in size and have high single-scattering albedos, due to constructive combination of the amplitudes of the emerging waves. The coherent backscattering effect was responsible for most of the planetary opposition surges observed in the solar system. [23] [24]

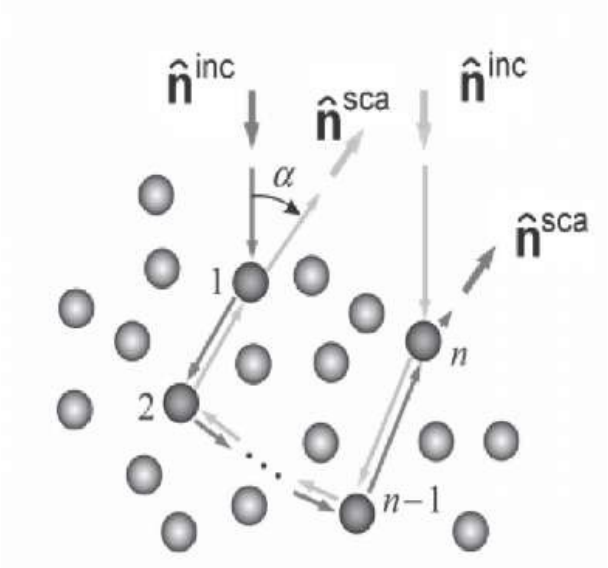

Figure 2.8: Schematic representation of the CBOE [1]

Figure 2.8 shows the schematic representation of a single electromagnetic wave indicated by $\hat{n}^{inc}$ with wavelength λ incident on a medium of n scatterers. The separation between the particles are of the order of wavelength λ. The wave is diffusely scattered in all directions by the particles in the medium. Considering two phase paths A or $\hat{n}^{inc}$, starting from 1,2..n and B $\hat{n}^{sca}$, starting from n, n-1, ..1 we can observe the emerging single electromagnetic wave $\hat{n}^{sca}$ with a phase angle α. In the medium the two portions of

the wave A and B traverse exactly the same path between 1 and n, but in opposite directions with numerous scatterings between particles along the path. The relative difference in phase between the parts of the wave that traverse along the same plane in opposite directions can be shown in equation below, with X being the distance between particles 1 and n.

$$\Delta\phi = (\hat{n}^{inc} + \hat{n}^{sca})X$$

At exact zero phase angle the phase difference $\Delta\phi$ between the two emerging waves is zero which leads to the two parts of the wave interacting constructively. If the amplitudes of the electric fields associated with the parts of the wave are E, then for random phase orientation we observe their combines intensities as $2|E|^2$. However in the exact backscattering direction the combined intensities are $4|E|^2$ for near zero phase angle. Due to high intensity coherence for near zero phase angles compared to larger phase angles the reflectance and CPR values are higher for CBOE. [23]

2.4.3 Properties of SHOE and CBOE

1. The Shadow Hiding Opposition Effect results from singly scattered light such that the height of the peak relative to the continuum brightness decreases as the reflectance of the medium increases. As CBOE depends on multiple scattered light the peak to continuum ratio increases as the reflectance increases.

2. The angular width of the SHOE peak depends on the scatterer mean separation and size distribution. While the CBOE angular width depends linearly on wavelength. The full width of the CBOE peak at half maximum (FWHM) can be calculated as:

$$\Delta g_{FWHM} = \frac{0.72\lambda}{2\pi D}$$

Where, λ is the wavelength of the incident radiation, D is the diffusion length. Nelson [37] observed very weak correlation between the theoretical predictions and

measured angular width of the phase curves for highly reflective alumina samples. The variation in particle size distribution for any given size were larger than the theoretical estimates used in the study.

3. Single reflections tend to preserve the direction of polarization for linearly polarized incident light while multiple scatterings tend to randomize them. Thus the SHOE peak is largely polarized in the same sense as the incident radiation while the light scattered in the opposite sense has no opposition surge.

4. For circularly polarized incident radiation the single reflecting events tends to change the polarization to the opposite sense while multiple scatterings tends to randomize the polarization. This results in SHOE peak having strong circular polarization in the opposite sense while CBOE contains both senses of polarization. [23]

2.4.4 Detecting Ice Regoliths

The primary objective of this study was to understand the nature of Icy regoliths by studying the presence of opposition effects in highly reflective samples. The presence of opposition effects can be detected by measuring the CPR values with decreasing phase angle reaching zero. By observing the trending properties of the CPR vs Phase angle plots we can conduct an empirical test to determine which opposition effect contributes towards the backscatter signal. The table below shows trending of CPR and LPR values with decreasing phase angle for different opposition effects.

With decreasing phase angle		
Opposition Effect	CPR (μ_C)	LPR (μ_L)
Shadow Hiding Opposition Effect (SHOE)	Decrease	Decrease
Coherent Backscattering Opposition Effect (CBOE)	Increase	Decrease
Incoherent multiple scattering	Increase	Increase

Table 2.3: CPR vs Phase angle expected trends with decreasing phase angle for opposition effects

In the shadow hiding opposition effect the brightness surges are a result of single scattering light that changes the original polarized signal which implies that μ_L and μ_C both decrease with decreasing phase angle. By contrast, the coherent backscattering opposition effect is a result of multiple scattered light combining constructively at the observer which results in partial preservation of the original polarized signal. Hence in CBOE the linear polarization ratio μ_L decreases and circular polarization ratio μ_C increases with decreasing phase angle. High reflectance values in backward direction could be caused by incoherent multiple scattering where the linear polarization ratio μ_L decreases and circular polarization ratio μ_C increases with decreasing phase angle.

Various undertaken studies have shown that CBOE are the dominating cause of opposition surge when the particles are in the size vicinity of the wavelength. For freshly prepared small-grained spherical water-ice material, the coherent backscattering effect is the dominating opposition effect but its contribution decreases when particles become more irregularly shaped and the bulk porosity increases. [28]

3 Techniques Deployed for Measuring Data

3.1 Measuring Stokes Parameters

3.1.1 Rotating Quarter Wave Plate Technique

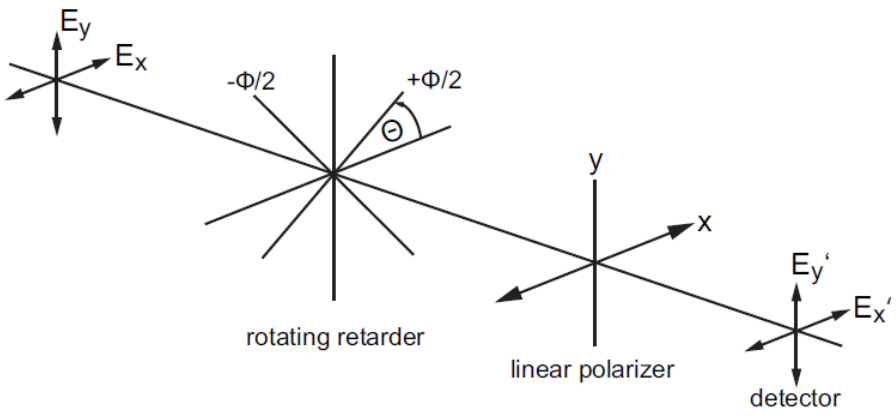

Figure 3.1: Schematic for the Rotating Quarter Wave Plate Technique [4]

Static polarimeter set-ups utilize multiple detectors with no moving optical components in the optical path. Dynamic methods are based on moving optical components in the optical path and utilize single detector. In this project we used the dynamic method called the Rotating Quarter Wave Plate Technique (RQWP). Advantages of a dynamic polarimeter include elimination of multiple detectors and the need to develop error reduction algorithms that arise in static multi-channel polarimeter. [4]

The Stokes parameter of a signal can be measured though the RQWP technique as shown in the schematic setup in Figure 3.1. The test signal is modulated by a rotating

quarter wave plate after which it passes through a linear polarizer and into the detector. The measured intensity I at the detector is a function of the quarter wave plate rotation angle θ.

$$I(\theta) = \frac{1}{2}[A - Bsin(2\theta) + Ccos(4\theta) + Dsin(4\theta)]$$

The intensity equation, $I(\theta)$ is a truncated Fourier Series whose coefficients are:

$$A = \frac{1}{\pi}\int_0^{2\pi} I(\theta)d\theta$$

$$B = \frac{2}{\pi}\int_0^{2\pi} I(\theta)sin(2\theta)d\theta$$

$$C = \frac{2}{\pi}\int_0^{2\pi} I(\theta)cos(4\theta)d\theta$$

$$D = \frac{2}{\pi}\int_0^{2\pi} I(\theta)sin(4\theta)d\theta$$

From the Fourier coefficients we can describe the Stokes parameters of an electromagnetic wave:

$$S_0 = A - C$$

$$S_1 = 2C$$

$$S_2 = 2D$$

$$S_3 = B$$

As the quarter wave plate angle is rotated from 0 to 360 degrees (0-2π) in 5 degree increments, the intensity values at each interval are recorded. The coefficients of the truncated Fourier Series are calculated by integrating the observed intensity values over the rotation angle range. The Stokes vector that describe the polarization state of a signal is derived from the coefficients as shown in the above equations.

3.2 Measuring Mueller Matrix

The polarization state of an electromagnetic wave can be determined by measuring the Stokes vector of the signal. The Stokes vector has four components that represent its total intensity and polarization state. The signal propagating through an optical medium can undergo polarization change that alters the Stokes parameters of the signal propagating outward from the medium. A circularly polarized signal can alter its polarization state to elliptically polarized light while propagating through an optical medium. We can correct for these polarization alterations by measuring the Mueller matrices of the optical medium and determining its impact on the Stokes parameters. [20]

3.2.1 Dual Rotating Quarter Wave Plate Technique

The Mueller matrix of an optical component is measured using the dual rotating quarter wave plate technique that determines its polarization properties and its impact on the propagating signal. The errors in retardance of the quarter wave plate, imperfect retardation increment and misalignment in the polarizing components can be corrected using error analysis. [4] [20]

The Dual rotating quarter wave plate technique measures a chopped signal that is modulated by rotating the polarizing optical elements. The signal is Fourier analyzed after passing through linear polarizers and dual rotating retarders to determine the Mueller matrix elements. As shown in figure the two fixed linear polarizers and rotating quarter wave plates are aligned with respect to their transmission axes and fast axes. The second retarder is rotated at five times the rate the first retarder is rotated which generates twelve harmonic frequencies in the Fourier Spectrum of the modulated intensity. [20]

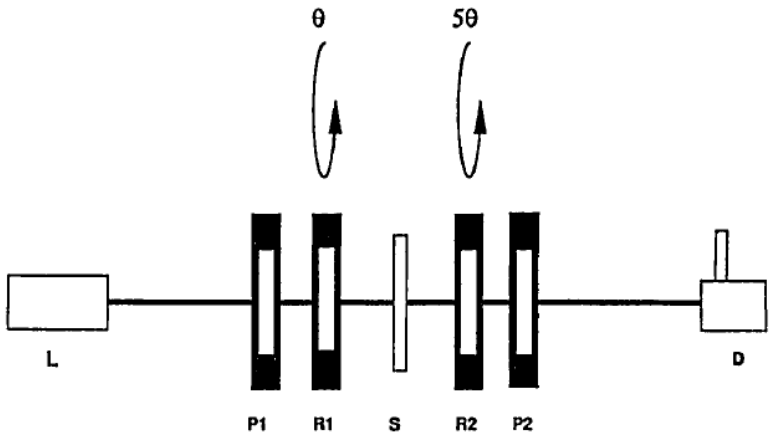

Figure 3.2: Dual Rotating Quarter Wave Plate Technique Schematic [20]

Figure 3.2 represents a schematic of the technique, L indicates the laser source while D indicates the detector. P1 and P2 are fixed linear polarizers while R1 and R2 are rotating Quarter Wave plates. S is the sample placed between the two rotating retarders. The intensity values are measured from the output signal as both the QWP's are incremented in 1:5 ratio such that the first retarder rotates through 180 degrees. The minimum number of equations required to solve for the coefficients uniquely are 25 with the first retarder rotating at 7.2 degrees through 180 degrees. There are many optimal methods to formulate the Fourier coefficients from the intensity values [46] one of which was used by Goldstein [20]was applied to the calculation.

The first retarder was incremented in 5 degree increments through 180 degree resulting in 36 equations that were solved to obtain the Fourier coefficients.

$$xa = I$$

I: vector of 36x1 intensity values

a: vector of 25 Fourier coefficients

x: matrix of 36x25 harmonic frequencies of the form shown below where θ values for each row are fast axis angle for first retarder

$$(1cos2\theta cos4\theta ...cos24\theta sin2\theta sin4\theta ...sin24\theta)$$

The solution for the formulated equation is represented as follows;

$$a = (x^T x)^{-1} x^T I$$

Solution acquired through this method was similar to the least squares solution expressed as;

$$I(\theta) = a_0 + \sum_{j=1}^{12} (a_j cos2j\theta + b_j sin2j\theta)$$

Solving the equation results in 12 sine and 12 cosine harmonic Fourier coefficients that are used to calculate the individual 4x4 Mueller matrix elements. Furthermore the Mueller matrices are normalized using its first element (m11) to acquire the normalized Mueller matrix with values ranging from $-1 < x < +1$.

4 Instrumentation and Data Acquisition Procedures

4.1 Measurement Procedure

In this experiment the samples were illuminated with 15-20mW power Nd:YAG (neodymium-doped yttrium aluminum garnet) laser at 1064nm or 1.064μm wavelength. The laser signal was generated from a multi-channel fiber coupled laser source with four available incident wavelengths. The schematic for the polarimeter assembly is shown in Figure 4.1, the dimensions for the assembly are listed in Appendix A. The incident signal generated from the laser source is fed through a fiber cable and attached to the caddy platform of the goniometric instrument after which it passes through a collimator and linear polarizer. The linearly polarized signal is chopped at a frequency of 250 Hz by using an optical chopper. Beam divergence effects of the incident radiation were eliminated by placing a focusing lens after the signal was chopped.

No.	Components	No.	Components
1	Laser Source	7	Beam Splitter
2	Optical Chopper	8	Focusing Lens
3	Focusing Lens	9	Quarter Wave Plate
4	Angled 45 degree Mirror	10	Linear Polarizer
5	Linear Polarizer	11	Si High Gain Detector
6	Quarter Wave Plate	12	Neutral Density Filter

Table 4.1: Components of the Optical Setup from Figure 4.1

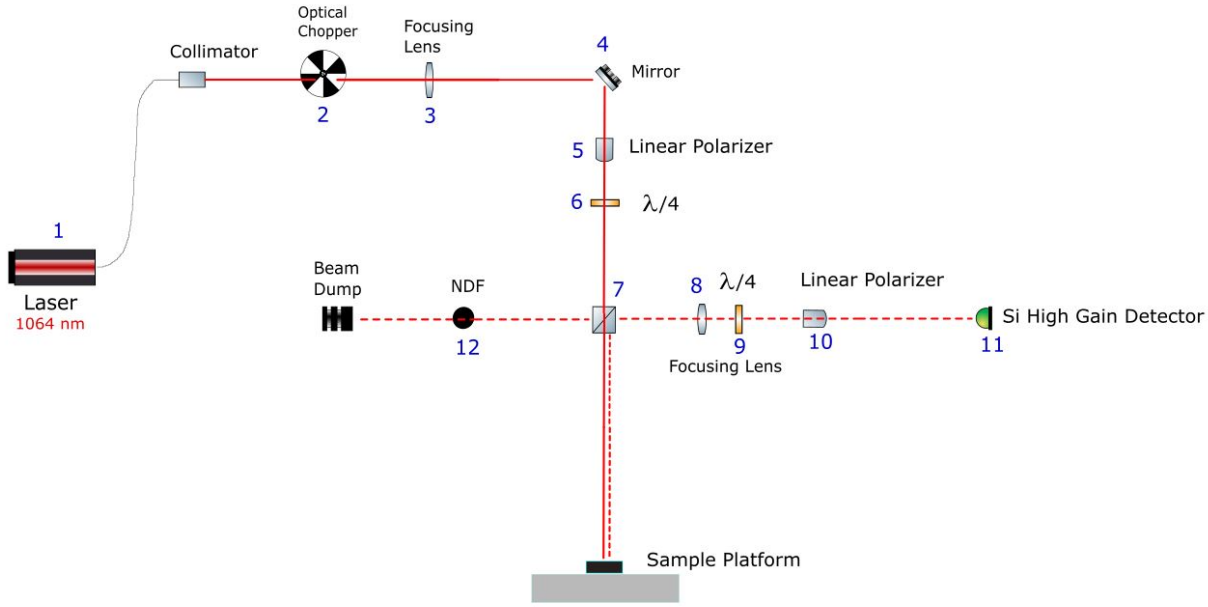

Figure 4.1: Schematic of the setup for the optical system on the MAGI for near zero phase angle measurements (Refer to Appendix A for distances between optical components)

The signal was then directed towards the sample platform by reflecting the chopped laser beam through a 45 degree mirror. Linear polarizer and quarter wave plate were inserted after the mirror reflection to change the polarized light into Circularly polarized light. The transmission axis of the linear polarized was aligned with the fast axis of the quarter wave plate at 45degrees. The rotation of QWP by 90 degrees changed the RHCP to LHCP which allowed us to measure both senses of polarized scattering.

The circularly polarized beam passed through a 50:50 beam splitter that split the incident signal into two equally powered signals without changing the polarization of transmitting beam that was incident on the sample. The secondary beam split from the beam splitter was reflected away from the instrument using a neutral density filter where the signal was contained.

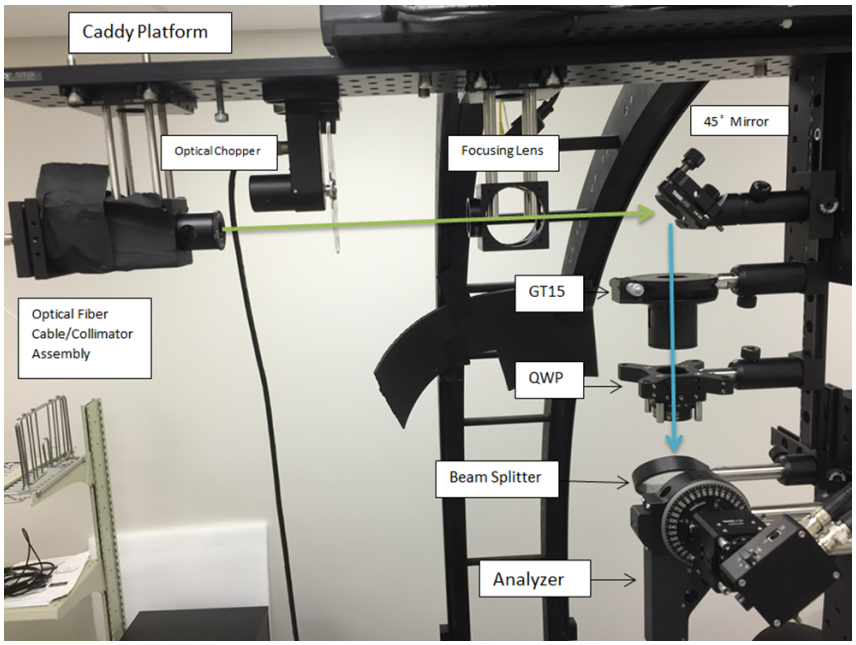

Figure 4.2: Optical components on the MAGI showing the propagation of the laser signal

The signal scattered from the sample is reflected into the analyzer by the beam splitter at any given phase angle setting. The signal scattered from the beam splitter flips the polarization of the reflected signal which is taken into account during the Stokes parameter calculation. The acquired signal is passed through rotating quarter wave plate followed by linear polarizer into the detector.

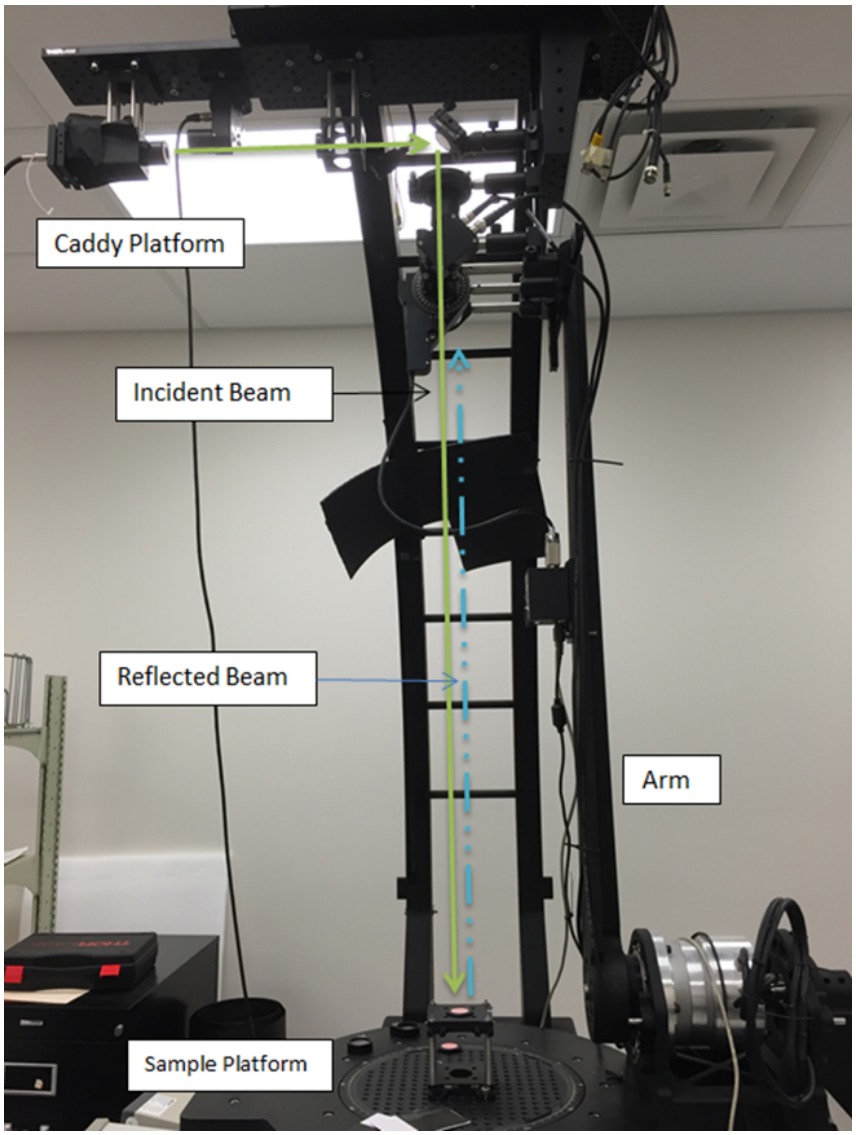

Figure 4.3: Incoming and backscattered polarized signal from the sample platform on the MAGI

4.2 Multi-Axis Goniometric Instrument

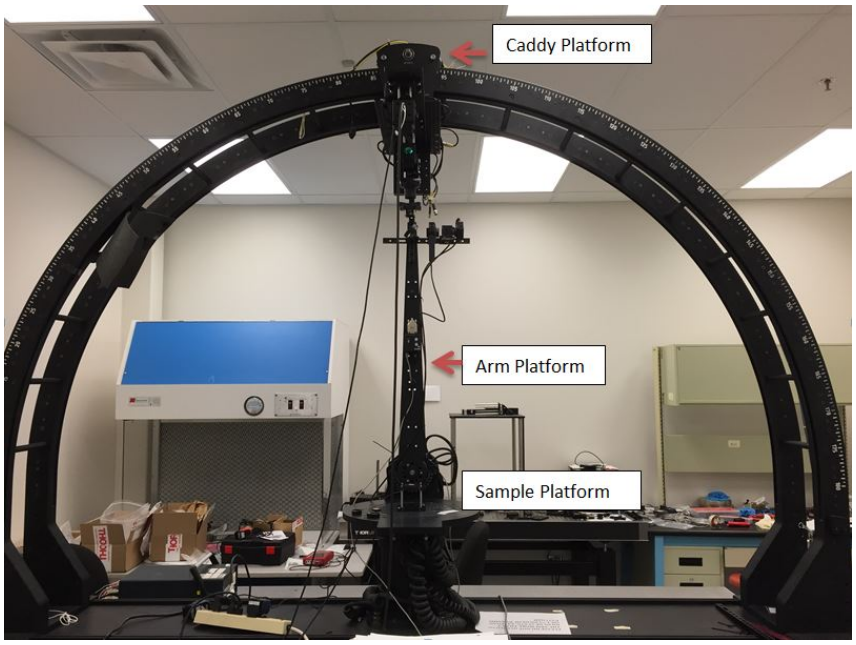

Figure 4.4: Multi-Axis Goniometric Instrument used for near zero phase angle measurements

The near zero phase angle setup is build upon the Multi Axis Goniometric Instrument (MAGI). MAGI is a long arm goniometric photopolarimeter capable of measuring backscatter over 180°region with precise 0.1°increments. The MAGI has two moving components called the caddy platform and long arm that allow for large phase angle measurements. The caddy resembles a satellite transmitter and the arm acts as the receiver enabling various incident and emergence angle orientations. The circularly polarized incident light source that illuminates the sample platform is mounted on the caddy platform. The backscatter from the sample inserted on the sample platform is received and analyzed using the components mounted on the long arm.

Near zero phase angle measurements were recorded from 0-5 degree phase angle in 0.1 degree increments. The long arm is kept in 0 degree emergence angle position as the caddy platform moves from 0-5 degree incidence angle. Similar results are expected when keeping the caddy platform stationary and moving the long arm platform. The heavy weight of the analyzer component mounted on the long arm significantly limits the arm's movement.

4.2.1 Caddy Platform

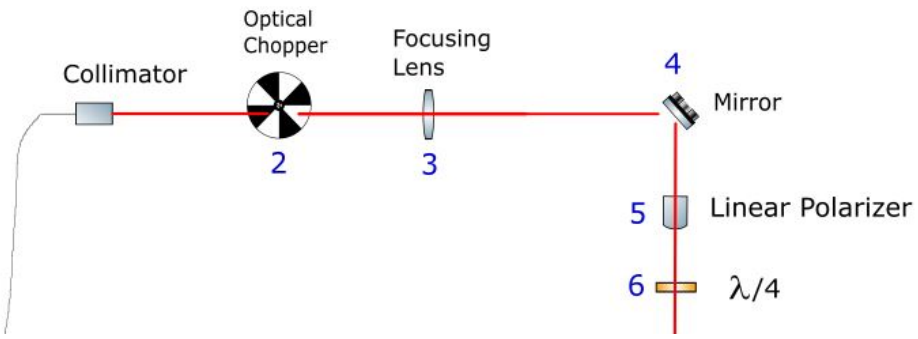

Figure 4.5: Schematic of the optical components mounted on the caddy platform

The caddy platform of the MAGI acts as a transmitting instrument that generates desired polarization state for the incident radiation. The incident laser beam was directed to the caddy platform from the laser source through an optical fiber cable followed by a collimator for low beam divergence. The laser signal was chopped by an optical chopper at a frequency setting which offers low noise input. Certain components are far apart which causes beam divergence and blurred beam spot, so focusing lens were used to ensure the beam was centered upon propagation. An angled 45°mirror was used to direct the incoming radiation towards the sample platform. The polarization state of the laser beam was random after the mirror reflection. A linear polarizer with its transmission axis parallel to the sample platform axis and a quarter wave plate with its fast axis offset by 45°s were mounted on the platform. The orientation of the LP and QWP ensured that

the incident radiation would be circularly polarized. The components mounted on the caddy platform are listed in the table below with their settings and functionality.

Caddy Platform			
No.	Components	Setting	Function
1	Laser Source	1064 nm	Nd:YAG powered Laser source
2	Optical Chopper	250 Hz	Chops the incoming signal
3	Focusing Lens	100 mm	Focuses the laser spot on the mirror
4	Angled 45 degree Mirror	Al Coated	Directs the beam on the sample platform
5	Linear Polarizer	Fast axis parallel to sample platform axis	Allows light polarized in linear direction
6	Quarter Wave Plate	Fast axis aligned with LP axis with 45 deg offset	Changed the incoming LP light to Circularly polarized light

Table 4.2: Caddy platform optical assembly components with their settings and functions

4.2.2 Arm Platform

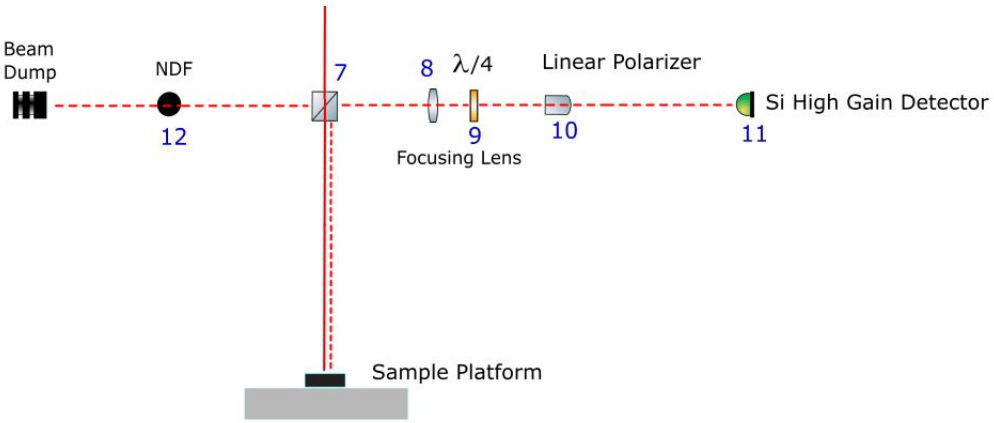

Figure 4.6: Schematic of the optical assembly on the arm platform

The arm platform of the MAGI acts as a receiving instrument that measures the backscattered signal from the sample platform. The circularly polarized signal incident from the caddy platform propagates through the beam splitter mounted on the arm platform. The 50-50 beam splitter splits the beam into primary and secondary components. The primary incident beam was directed towards the sample platform while the secondary beam was contained using a neutral density filter and beam dump. The backscattered radiation from the sample platform was focused towards the analyzer section through the 45°angled beam splitter. The analyzer section consisted of quarter wave plate and linear polarizer followed by the detector. The LP and QWP decomposed the backscattered radiation into Fourier components by using the rotating quarter wave plate technique. The components mounted on the arm platform are listed in the table below with their functionality and settings.

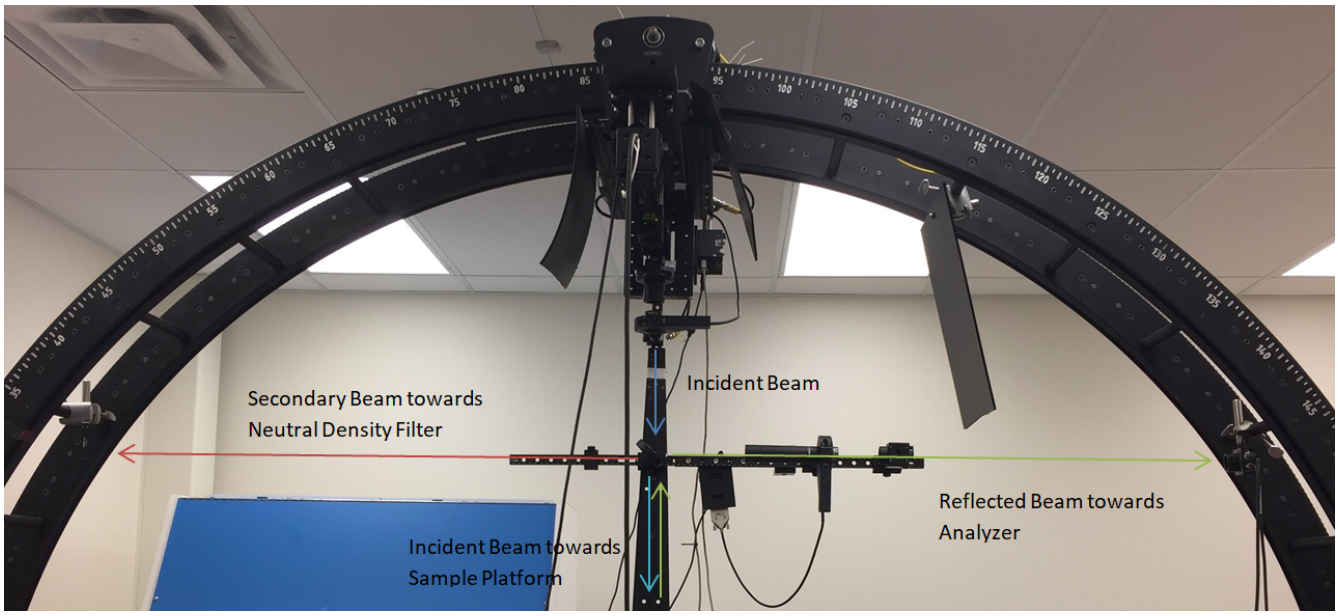

Figure 4.7: Incident and Reflected beams propagating through the arm platform

Figure 4.7 shows the propagating incident signal from the caddy platform through the beam splitter onto the samples platform. The unwanted secondary beam split from the 50-50 beam splitter was guided towards the Neutral Density Filter NDF with high optical density. The signal received from the sample platform was reflected from the 45°beam splitter towards the analyzer.

Arm Platform			
No.	Components	Setting	Function
7	Beam Splitter	50-50 s and p polarization split with anti-reflective coating	Splits the incoming circularly polarized beam into two RHCP beams
12	Neutral Density Filter	ND $>$ 6	Blocks out the secondary RHCP beam
Analyzer Setup			
Parts List	Setting	Function	
8	Focusing Lens	150 mm	Focuses the reflected beam onto the analyzer section
9	Quarter Wave Plate	Fast axis aligned with LP axis with 45 deg offset	Changed the incoming LP light to Circularly polarized light
10	Linear Polarizer	Fast axis parallel to sample platform axis	Allows light polarized in linear direction
11	Si-High Gain Detector	0$<$ Gain $<$ 10 dB	Measures the incoming signal in voltage units

Table 4.3: Optical components for the Arm platform with their settings and functions

4.3 Data Acquisition Setup

The data for near zero phase angle measurements were collected using three programmed softwares that controlled the MAGI setup parameters. The three software elements were Motor Control, Detector Control and Goniometer Control. Using the programs simultaneously we were able to perform the RQWP technique through which we acquired the Stokes parameters for a desired phase angle orientation on a sample.

From the RQWP technique described in previous section we controlled the QWP using the motor control software. Detector control software was used to display the measurements from the Lock-in amplifier that were measured using high-gain Si detector. Labview programmed script called the Goniometer control was used for the MAGI setup that controlled the caddy platform and long arm movements. In this section we shall discuss the programmed software elements and the process through which we acquired the Stokes parameters and Mueller matrices for any given sample or optical element.

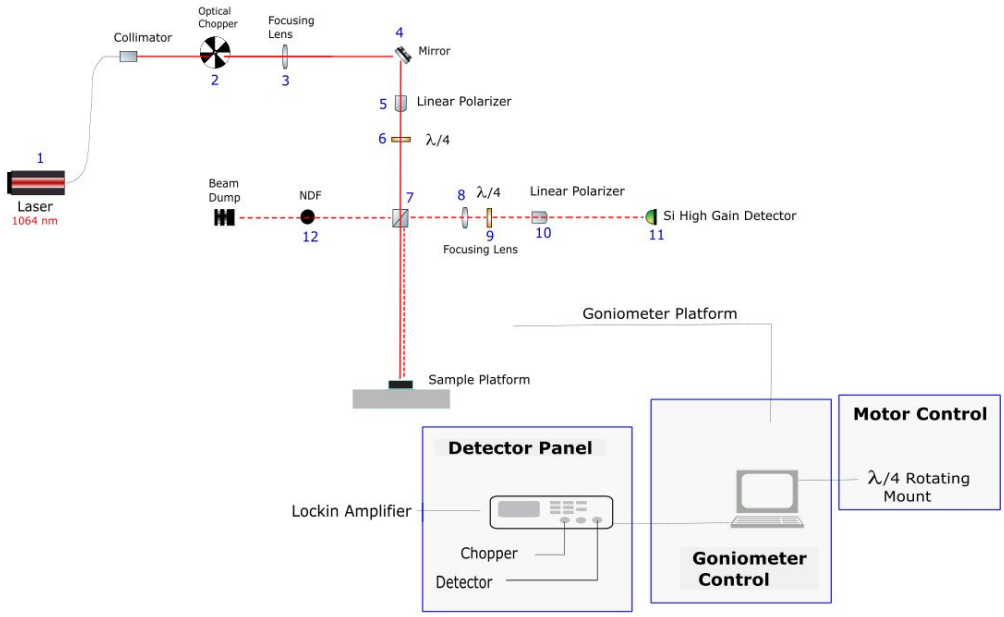

Figure 4.8: Schematic of the Data Acquisition Programs for the Optical Setup

4.3.1 Motor Control

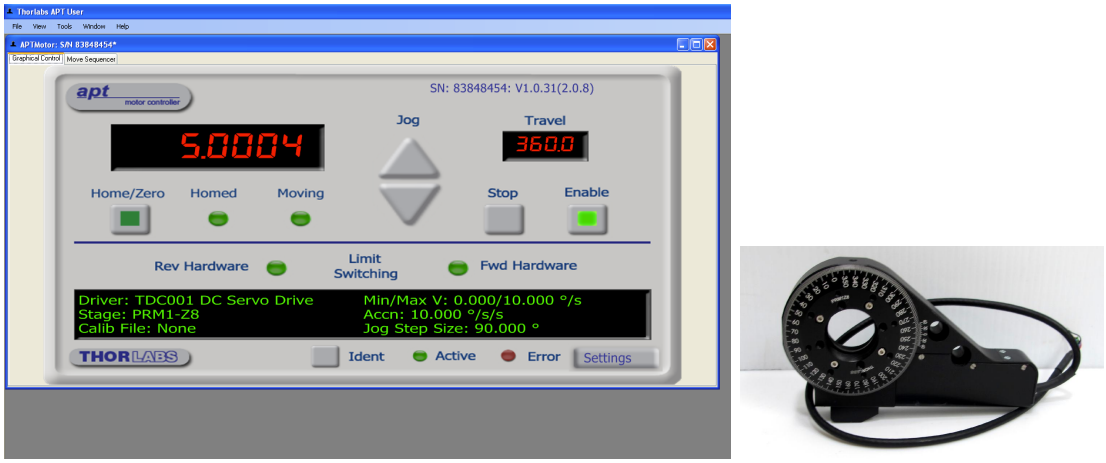

(a) MotorControl (b) Rotation Stage

Figure 4.9: (a) The motor control software used to run the (b) Rotation stage where the QWP was mounted

The motor control software was used to rotate the quarter wave plate in the analyzer section according to the rotating quarter wave plate technique. In the RQWP technique intensity values were recorded while the quarter wave plate was rotated 360 degree in 5 degree increments. The QWP rotation was controlled using the motor control program. The program enabled us to precisely rotate the QWP at an accuracy of ± 0.01 degrees. The table below shows the setting used for the Motor control application:

Motor Control		
Button	Setting	Function
Jog Step Size	5 degrees	Increments the rotation stage clockwise (Up) or counter-clockwise (Down)
Acceleration	10 degrees/sec	Speed at which the rotation stage moves
Travel	360 degrees	Overall rotation distance covered by the rotation stage

Table 4.4: Motor Control Software settings used for operating the rotation stage

4.3.2 Detector Control

The Detector control program running through the Lockin Amplifier was used to measure the voltage values of the Si-High gain detector. The intensity measurements were acquired from the Si-High gain detector (Thorlabs PDA100a) using the detector control graphical user interface. The detector control program monitored and outputted the data read from the detector via the lockin amplifier. The detector control allowed for stable measurement display with custom AC gain settings and monitored the background noise levels. The table below shows the Lockin amplifier settings used while acquiring the intensity measurements and its corresponding functionality.

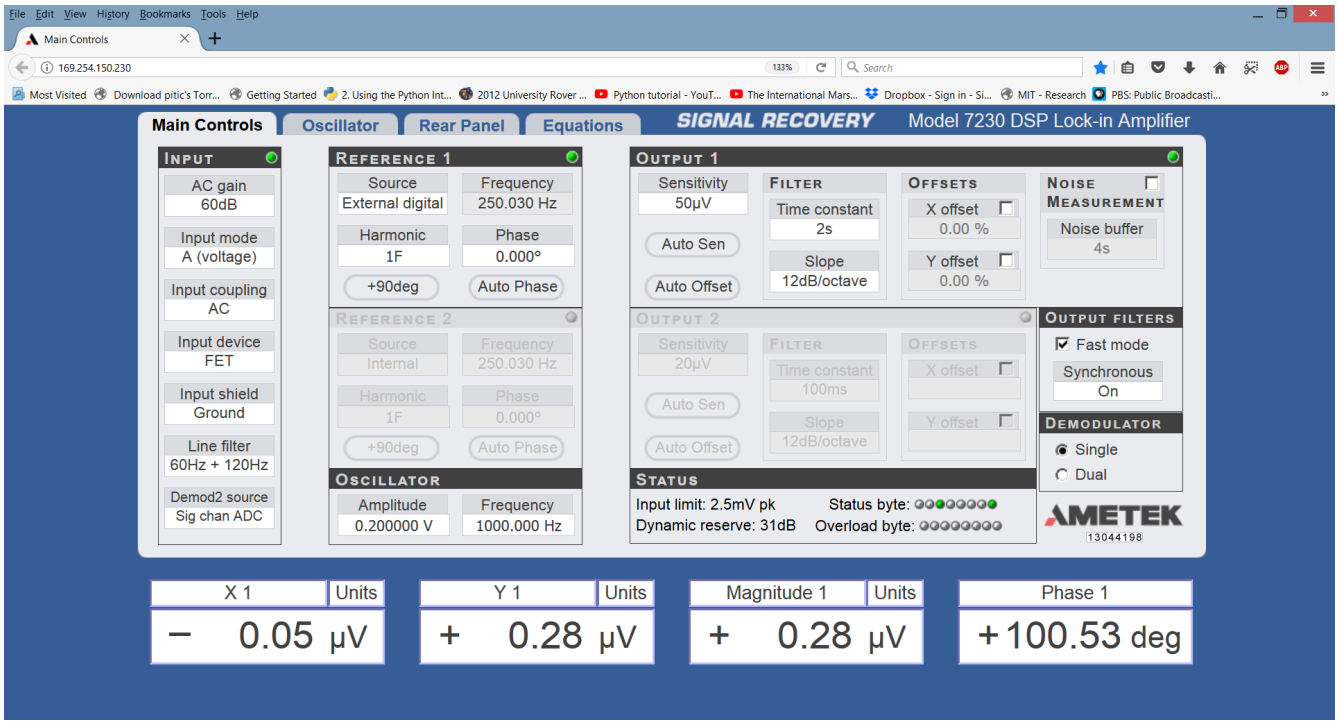

Figure 4.10: Front panel display for the detector control software run through the Lockin Amplifier

Input		
Button	Setting	Function
AC Gain	30dB - 60dB	High gain setting during acquisition of low intensity signal ($\ll 100\mu$V)
Input mode	A(voltage)	Voltage input to the BNC connector to the Lockin Amplifier
Input device	FET	Input impedance is 10MΩ
Input shield	Ground	Shells of the input connectors are connected directly to chassis ground
Line Filter	60Hz + 120 Hz	Enable 60 and 120 Hz notch filters
Reference 1		
Button	Setting	Function
Source	External digital	Reference channel is configured to accept a TTL reference source applied to the front panel via the Optical chopper
Frequency	250 Hz	Measures the frequency from the Optical Chopper
Output 1		
Button	Setting	Function
Sensitivity	Auto Sens	Adjusts the sensitivity of the amplifier for stable measurement. Auto-sensitivity operation increases the sensitivity range if the magnitude is $> 90\%$ of full scale, reducing the range when magnitude is $< 30\%$ of full scale
Time Constant	2 seconds	Setting the time constant of the output filters

Table 4.5: Lockin Amplifier Settings and functions for the detector control software

4.3.3 Goniometer Control

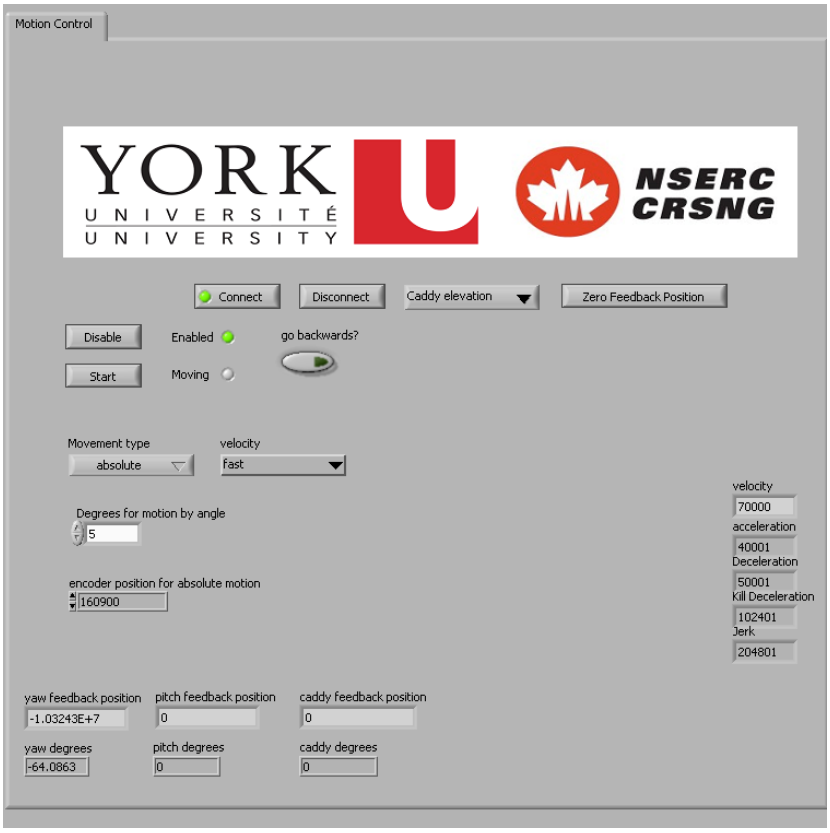

Figure 4.11: Front panel display for the MAGI control software written in Labview environment

Multi-axis goniometer instrument was controlled using the goniometer control program script as shown in the figure above. Goniometer control was programmed in labview programming environment and controlled using the graphical user interface display. The goniometer control program controlled the movements of the caddy platform and long arm platform to 0.05 degree precision.

The MAGI control was used to move the caddy and arm platforms creating difference in incidence and emergence angles starting from 0°phase angle to 5°phase angle. The settings and their functions for the goniometer control program are shown in the table below.

4.4 Data Acquisition Procedure

The three software programs were sequentially run to acquire the Stokes vector measurements for phase angles ranging from 0-5 degrees. Figure 4.12 shows the block diagram consisting of three control programs used for the acquisition of phase angle measurements. Firstly the instrument was calibrated to ensure that measurements started from zero phase angle and would be repeatable over different samples. The caddy platform on the goniometer instrument was aligned to zero reading using the Goniometer Control software such that the caddy was perpendicular to the arm platform. After the instrument was set at zero phase angle the laser signal was focused on the sample platform and corrected for any misalignment by rotating the 45 degree mirror, this ensures that the laser beam stays incident on the same spot over all the phase angles.

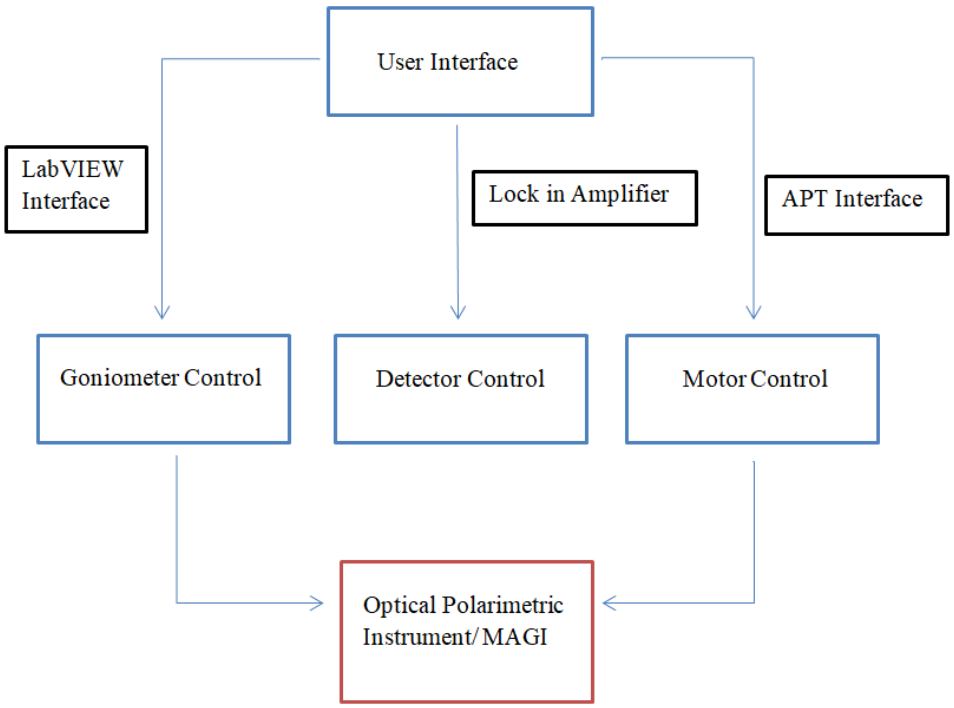

Figure 4.12: Block Diagram for the Optical Instrument control and interaction

For calibrating the analyzer section a flat mirror was placed on the sample platform that would reflect the signal back to the beam splitter. The signal reflected from the 45 degree beam-splitter was focused on the detector after it passes through the rotating quarter wave plate and linear polarizer. Small physical corrections would be made to the mounts if the beam would not propagate through the center of the optical elements. The output signal intensity for the flat mirror and sample under investigation are observed and recorded for stability check.

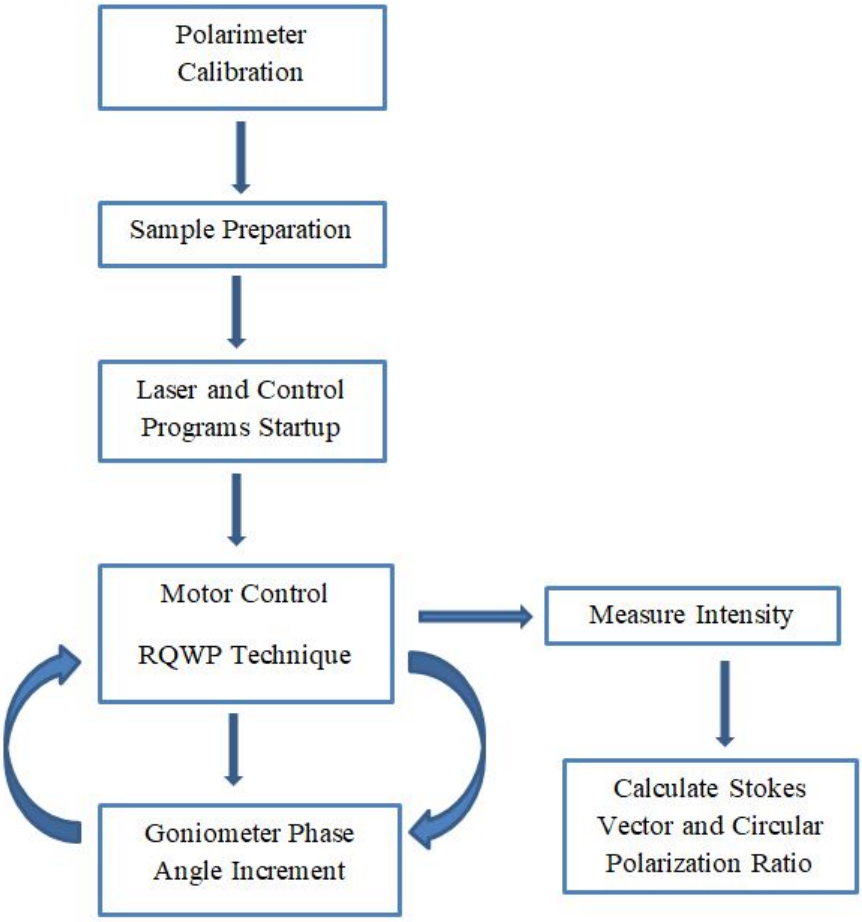

Figure 4.13: Flowchart for the Polarimetric Measurement Procedure

After calibrating the instrument and setting the caddy platform at zero phase angle the measurements are recorded by the control programs. Figure 4.13 shows a high-level flowchart describing the data acquisition procedure. Signal intensities are acquired through the lock-in amplifier by rotating the QWP over 360 degrees using the motor control program for zero phase angle. The signal intensities over 360 degrees of QWP rotation in 5 degree increments are passed through Fourier transforms to compute the Stokes parameters and CPR for the backscattered signal at zero phase angle. As the CPR for zero phase angle was acquired the caddy platform was moved in increments of 0.1 degree over range of 5 degrees using the goniometer control program. The Stokes parameters and CPR values are computed for backscattered signal of each phase angle by performing the rotating QWP method and incrementing the caddy platform. The rotating QWP method takes approximately 20 minutes to record for each phase angle signal while moving the caddy platform for each increment takes 10-20 seconds.

4.4.1 Sample Preparation

Spectralon Standard

The Standard Spectralon diffuse samples from Labsphere were studied as baseline measurements for powdered alumina samples. The Spectralon samples had varying range of reflectance values ranging from 2%-99% with true Lambertian surface features. The samples were made of pressed transparent thermoplastic particles that produce a close to true Lambertian surface reflections. [49] Figure 4.14 shows Spectralon pucks with varying reflectance values from highest to lowest used in the phase angle study.

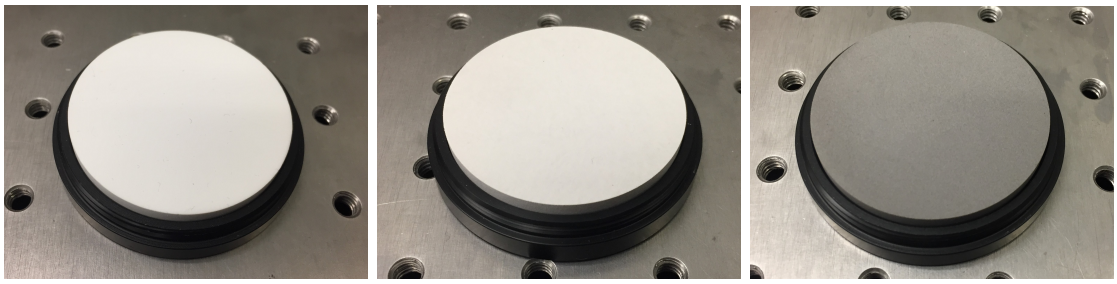

(a) Spectralon 99 % Puck (b) Spectralon 60 % Puck (c) Spectralon 20 % Puck

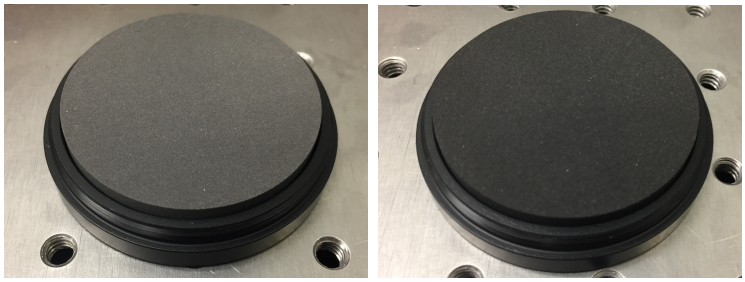

(d) Spectralon 10 % Puck (e) Spectralon 5 % Puck

Figure 4.14: Standard Spectralon Diffuse Samples from Labsphere

Powdered Aluminium Oxide

Industrial grade pure white alumina was selected as the main powdered sample for study. Alumina powder is commonly used as polishing grit due to its abrasive nature/ hardness and is the second most abundant element found on the moon. Alumina powder was studied as it is bright in color and comes in various grain sizes which enables us to measure backscatter for wavelength scaled particles. [42]

The powdered samples were gently poured into dark 2" sample cup and the cups were lightly shaken to allow for natural settling. After allowing the sample to settle the top surface was leveled by cutting through the excess sample with a glass slide. The sample was not packed in any manner instead the cups were shaken lightly to simulate a powdered surface of a planetary regolith. Similar preparation procedures were followed for all four alumina oxide samples under study such that surface deviations would not affect the measurements.

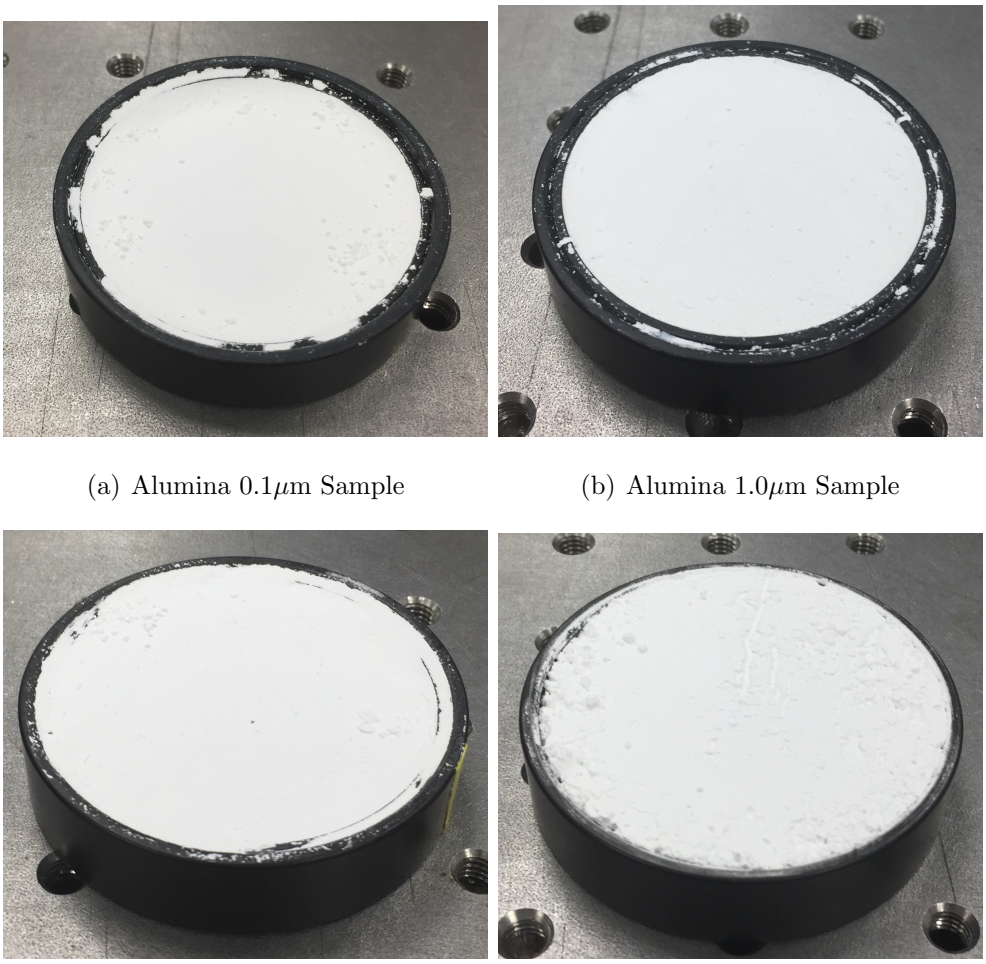

(a) Alumina 0.1μm Sample

(b) Alumina 1.0μm Sample

(c) Alumina 2.1μm Sample

(d) Alumina 4.0μm Sample

Figure 4.15: Microgrit Alumina powder prepared in a sample container

Particle Size distribution

Mishchenko [34] approximated the particle size distribution of the powdered samples by using a narrow gamma distribution as shown below:

$$N(r) = kr^{\frac{1-3b}{b}} e^{\frac{-r}{ab}}$$

Where a = grain size, b = 0.04 and k is a constant.

We used the narrow gamma distribution equation from Mishchenko's model to estimate

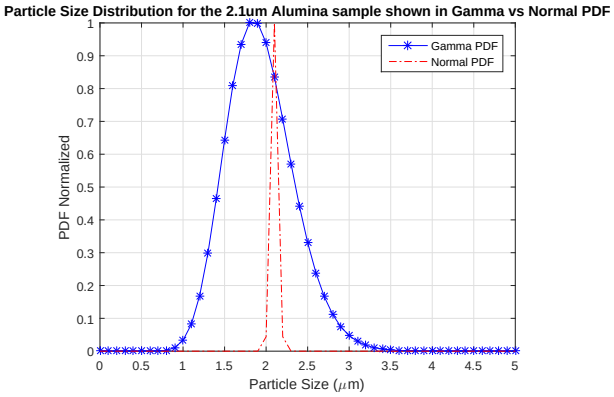

(a) Alumina 2.1μm

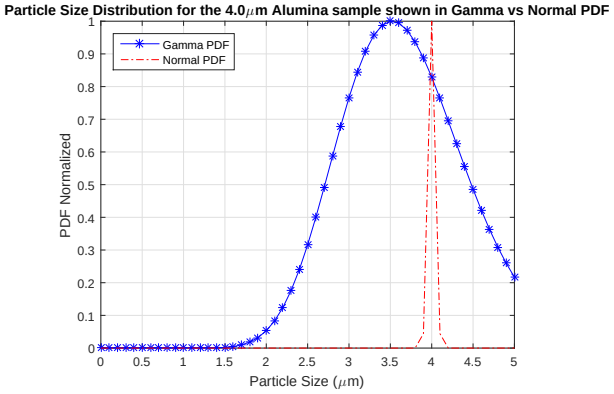

(b) Alumina 4.0μm

Figure 4.16: Particle Size Distribution for 2.1 μm Alumina sample with Gamma and Normal Probability Distribution Function

variation in particle size distribution for alumina powdered samples with 2.1 and 4.0 μm grain sizes. The normal probability distribution is calculated from a Mathlab built-in function ('normpdf') [2] that calculates the normal probability density for a standard normal distribution evaluated at particle size values.

From figure 4.16 we can observe that the estimated particle size distribution from Mischenko's model and normal distribution varied over the stated size range for both the samples. The samples used for this study were intended to be used as optical abrasives and they could vary from the theoretical particle size distribution estimates. [37] [42]

4.4.2 Liquid Samples

In order to study important parameters regarding icy regoliths we must first ensure that the experimental setup can observe signal intensity and CPR from aqueous solutions. For this study two different types of liquid samples were employed: colloidal solution of powdered alumina in a liquid medium and wavelength sized suspension of polystyrene beads.

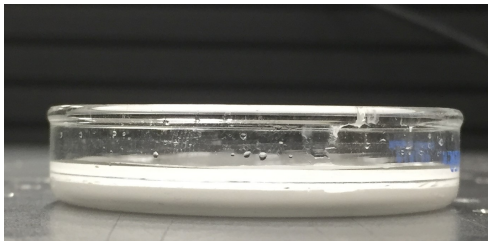

(a) Alumina 2.1μm in Liquid Glycerol

(b) Aqueous Suspended Beads Solution

Figure 4.17: Liquid Solutions for Analog Measurements

Powdered alumina sample of 2.1μm grain size was poured in a sample container after which liquid glycerol was added creating a colloidal solution. The sample was allowed to settle which resulted in sedimentation of alumina particles inside a glycerol solution as shown in figure 4.17. Glycerol is a viscous liquid with high transmission coefficient which allows the alumina particles to be suspended inside the medium and mimic a icy regolith

with cracks and rock impurities. Thermo Fisher Scientific manufactures [33] an aqueous milky white suspension containing polystyrene spheres with nominal diameters of 0.76μm. Incident signal would undergo change in wavelength propagating from vacuum λ_0 to a liquid medium λ_l with refractive index (n) resulting in the liquid wavelength of, $\lambda_l = \lambda_0/n$. For an incident wavelength of 1.064μm, the particle size to wavelength ratio (d/λ) for suspended particles in Thermo Fischer solution would be 0.71, and for glycerol/alumina colloidal solution would be 0.68 which are much smaller than the incident radiation.

5 Measurements and Dataset Analysis

5.1 Previous Studies Observing Circular Polarization Ratios

In this section we shall overview the previous studies undertaken related to the experimental near zero phase angle and the implications these studies have on our measurement setup. There have been several analog CPR and reflectance experiments performed to study and differentiate the shadow hiding effects. We shall observe some of Nelson's published papers and draw implications that are applicable to our current study. [37]

The author measured the change in reflectance and circular polarization ratio with respect to phase angle of highly reflective aluminum powders for understanding the contribution of coherent backscattering effect on the reflectance phase plots of planetary regoliths. The schematic for the experiment is shown in the figure 5.1 which utilizes a goniometric photopolarimeter with phase angle range from 0.05°-5°. The experiment measures CPR and reflectance for variety of alumina particles sizes ranging from 1μm to 30μm, illuminating the samples from a HeNe laser at 0.633μm wavelength.

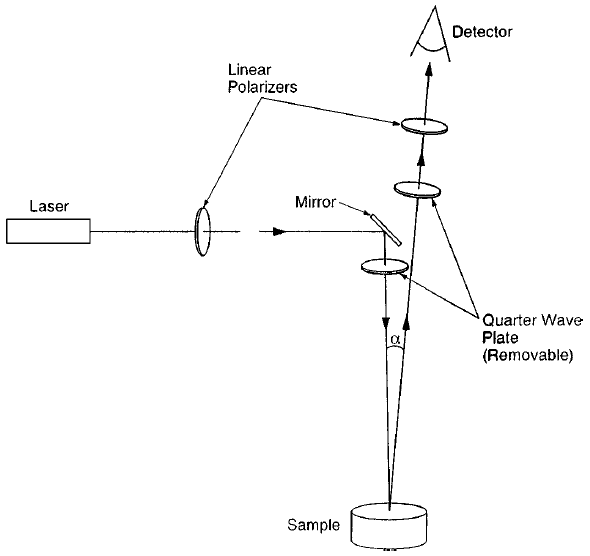

Figure 5.1: Schematic from the Nelson's experiment [37]

Nelson observed that for cases where the wavelength of the incident radiation is much larger than the sample particle size, the photons behave as if they were interacting with an ensemble of particles of size comparable to the wavelength of incident radiation. For cases where the particle sizes are much larger than the wavelength, the photons appear to be interacting primarily with wavelength sized cracks, surface asperities or irregularities in the regolith particles rather than with the particle as a whole. [37]

The alumina samples used in our study were same as the Nelson study and were taken from the Micro Abrasives Corporation of Westfield, MA. The manufacturer states that particles smaller than 1.5μm were manufactured by a process different from that of larger particles where the larger particles are platelet-shaped with each particle being an individual crystal. The smaller particles are of unspecified morphology. [37] [38] The CPR vs phase angle measurements are presented in the figures below:

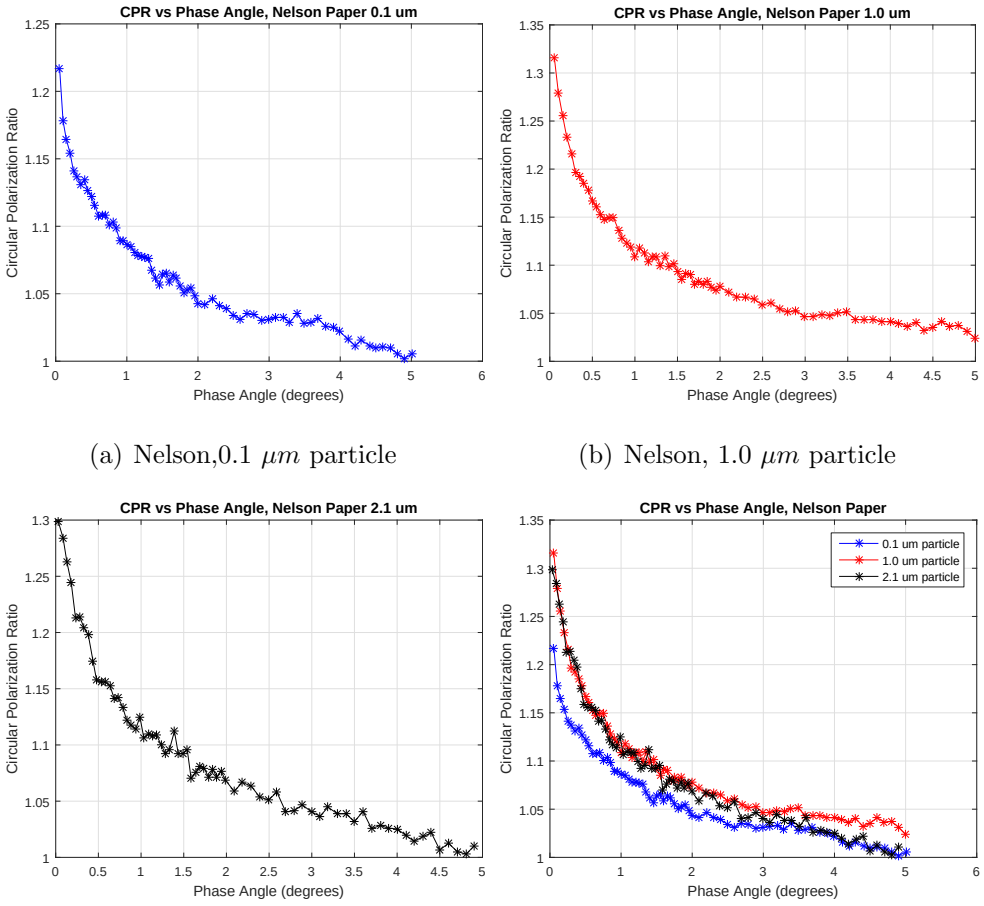

(a) Nelson,0.1 μm particle

(b) Nelson, 1.0 μm particle

(c) Nelson, 2.1 μm particle

(d) Nelson particles

Figure 5.2: CPR vs Phase Angle for highly reflective alumina sample from Nelson's experiment

Observing the CPR vs phase angle plots here were some key findings:

- The rate of increase in CPR was largest for cases where the particle size was within a few wavelength sizes of the incident radiation. This result is consistent with the hypothesis that CBOE is the principal contributor to the opposition effects. [44]
- In highly reflective particulate materials the size and shape of the phase curve near 0°is influenced by coherent backscattering process. [44]
- Coherent backscattering effects are more enhanced than theoretically predicted for particle sizes much larger and smaller than the wavelength due to variations in the size distribution of particles, irregularities on the surfaces and interiors of larger particles that act as scattering centers. [44]

5.2 Analog Measurements

The rotating quarter wave plate technique was used to measure the stokes parameters of various analog samples using the long arm goniometric data acquisition setup.

5.2.1 Stokes Parameters

In the experimental setup, a left-handed circularly polarized signal was created from a partially polarized chopped signal after passing through a linear polarizer and quarter wave plate. The fast axis of the quarter wave plate was aligned with the transmission axis of the linear polarizer and rotated 45 degrees, so that the linearly polarized signal generated from the polarizer undergoes a phase shift and changes into left handed circularly polarized light. This left handed circularly polarized signal was incident on the Spectralon 5% reflectance analog sample which diffusely scattered the incident radiation. The backscattered signal from the analog sample at exact zero degree phase was measured using the RQWP technique. The detector signal intensity values over 360˚rotation of quarter wave plate angle were recorded as shown in figure 5.3.

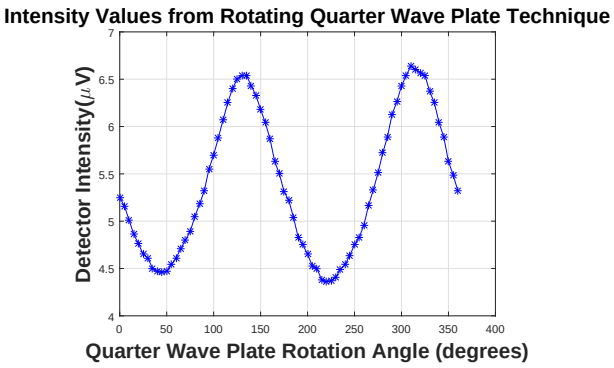

Figure 5.3: Intensity values from the detector for 360˚of quarter wave plate rotation

As the quarter wave plate was rotated in 5°increments the change in QWP angular increment, $d\theta$ remained constant to 5°or 0.0872 Radians, $I(\theta)$ represented the detector intensity values at each quarter wave plate angle starting from 0°to 360°. The Fourier coefficients listed in section 3.1.1 were calculated from the intensity values and the Stokes parameters were then acquired from the coefficients.

$$A = \frac{1}{\pi}\int_0^{2\pi} I(\theta)d\theta; B = \frac{2}{\pi}\int_0^{2\pi} I(\theta)sin(2\theta)d\theta; C = \frac{2}{\pi}\int_0^{2\pi} I(\theta)cos(4\theta)d\theta; D = \frac{2}{\pi}\int_0^{2\pi} I(\theta)sin(4\theta)d\theta$$

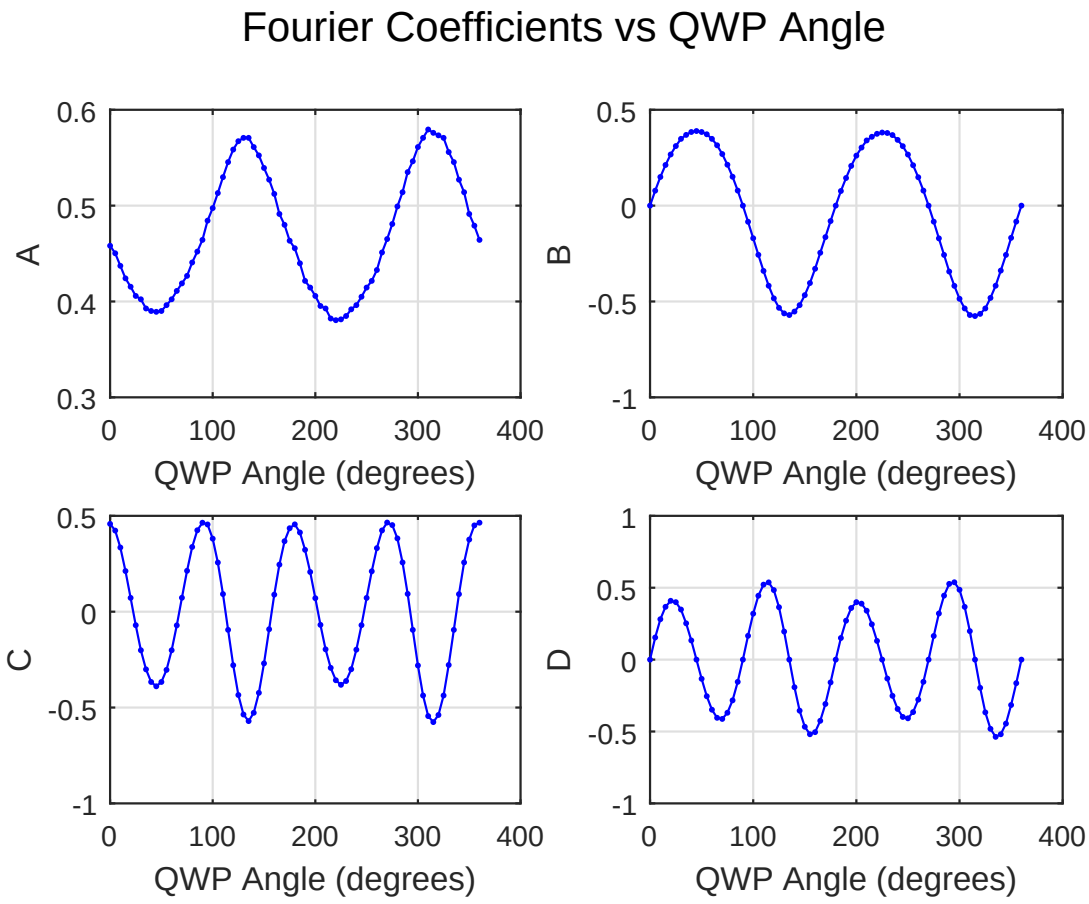

Figure 5.4: Four Fourier Coefficient values for 360°rotation of quarter wave plate

Figure 5.4 shows four Fourier coefficients values over rotating quarter wave plate angle for a circularly polarized signal. After the sampling process was completed the sampled

signal was Fourier transformed, which provided the DC, $\sin(2\theta)$, $\sin(4\theta)$, $\cos(4\theta)$ terms represented by A, B, C and D respectively.

The table below shows the calculations performed from the acquired Fourier coefficients to observe the CPR value for the backscattered signal.

Measuring Circular Polarization Ratio from Fourier Coefficients					
Fourier Coefficient	Value	Stokes Parameter	Coefficient Equation	Value	Normalized Values
A	10.933 ±0.48	S_0	A-C	10.8532 ±0.49	1
B	-2.0877 ±0.29	S_1	2C	0.1596 ±0.02	0.0147
C	0.0798 ±0.01	S_2	2D	0.0775 ±0.01	0.0071
D	0.0388 ±0.005	S_3	B	-2.0877 ±0.29	-0.1924

Table 5.1: CPR calculation from Fourier coefficients and Stokes parameters

Additional information regarding the polarization state of the received signal was calculated from the acquired Stokes parameters. The degree of polarization, degree of linear and circular polarization as well as the circular polarization ratio were calculated using the following equations:

$$Degree of Polarization(m) = \frac{\sqrt{S_1^2 + S_2^2 + S_3^2}}{S_0}$$

$$Degree of Linear Polarization(l) = \frac{\sqrt{S_1^2 + S_2^2}}{S_0}$$

$$Degree of Circular Polarization(c) = \frac{|S_3|}{S_0}$$

$$Ellipticity Angle(\chi) = \frac{1}{2} sin^{-1}(\frac{S_3}{S_0}); Rotation Angle(\psi) = \frac{1}{2} tan^{-1}(\frac{S_2}{S_1})$$

Parameters	Values
Degree of Polarization	0.1930
Degree of Linear Polarization	0.0163
Degree of Circular Polarization	0.1924
Ellipticity Angle	33.36°
Rotation Angle	24.17°

Table 5.2: Additional Polarization Parameters

The circular polarization ratio for the acquired signal was calculated using the normalized Stokes vector as follows:

$$CPR = \frac{SC}{OC} = \frac{S_0 - S_3}{S_0 + S_3}$$

As the normalized S_0 parameter is 1 the equation for the CPR reduces to the equation below with S_3 parameter representing the circular polarization value.

$$CPR = \frac{1 - S_3}{1 + S_3} = \frac{1 - (-0.1924))}{1 + (-0.1924)} = 0.6773$$

The CPR value for the acquired signal was between $0 < \text{CPR} < 1$ which indicates that the measured signal from the sample platform was diffuse in nature. The sample used for the measurement was a standard Spectralon puck with 5% reflectance of the incoming signal.

5.2.2 Spectralon Standard

The Stokes vector and CPR calculations were then performed for different Spectralon standard samples using the same technique over a range of phase angles starting from 0°to 5°with 0.1°increments.

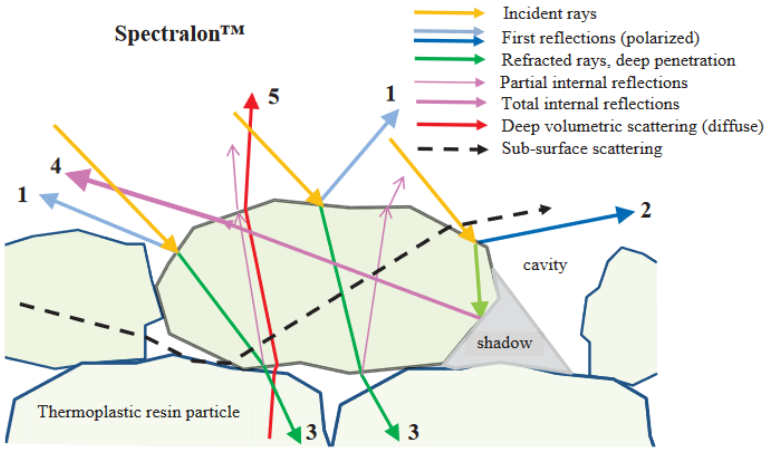

Figure 5.5: Reflection model for Thermoplastic resin particles (Spectralon Pucks) [29]

Due to limitations in the experimental setup the CPR measurements between 1.2°< Phase angle < 2.1°could not be acquired. The limited mounting capability of the beam splitter resulted in the incoming signal being blocked by the lens mount. However, using the data trends from the rest of the measurements and extrapolating the values helped us fill in the missing data points to certain degree of accuracy.

The phase angle measurements for Spectralon diffuse reflectance standard samples were performed over range of 0-5 degree. The spectralon samples were spectrally flat over the UV-VIS-NIR spectrum with the surface providing Lambertian reflections. The specifications for all the different spectralon sample pucks used for the study are listed in the table below:

Spectralon Reflectivity (%)	Intensity at 0°phase (mV)	Normalized Intensity w.r.t. 5%
99	17.57	18.89
60	12.35	13.28
20	4.83	5.19
10	2.25	2.42
5	0.93	1

Table 5.3: Spectralon Diffuse Reflective Standard Samples

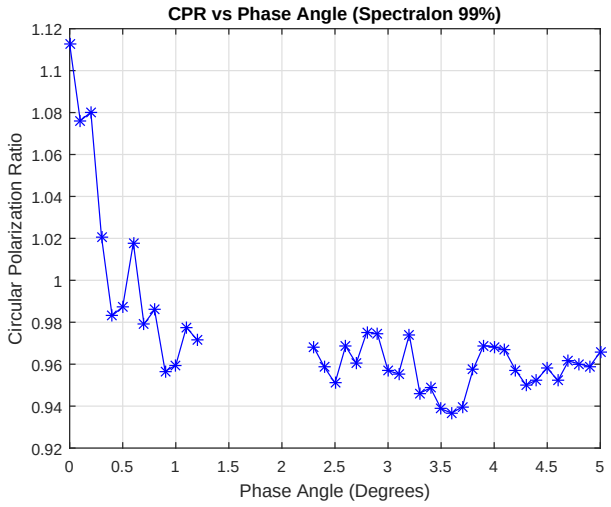

(a) Spectralon 99%

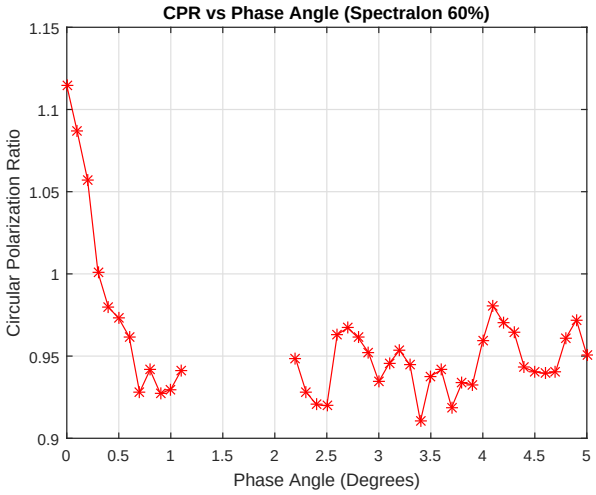

(b) Spectralon 60%

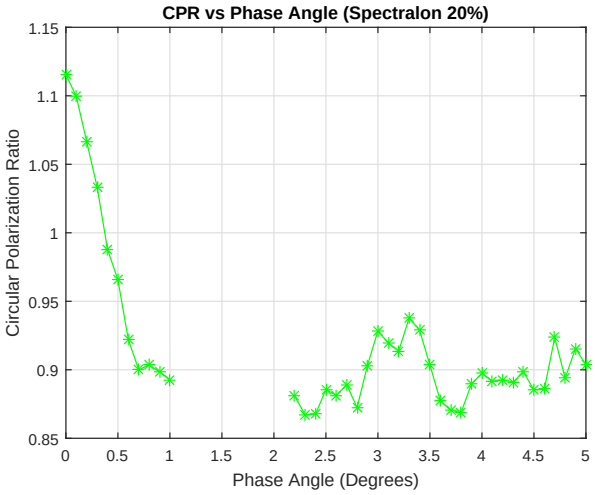

(c) Spectralon 20%

Figure 5.6: CPR vs Phase Angle for Standard Spectralon Diffuse Reflectance Pucks

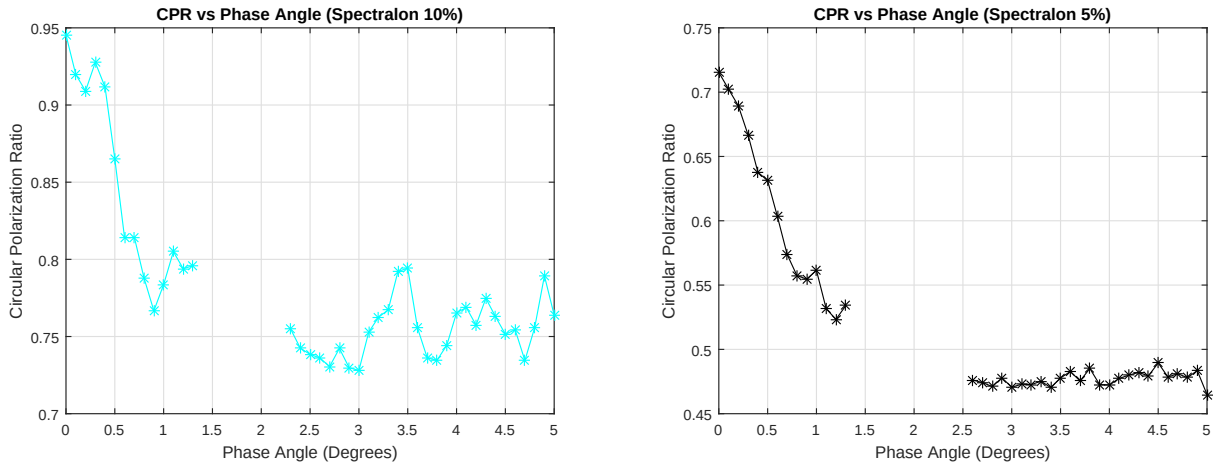

(a) Spectralon 10%

(b) Spectralon 5%

Figure 5.7: CPR vs Phase Angle for Standard Spectralon Diffuse Reflectance Pucks

Figures 5.6 and 5.7 shows the relative increase in CPR values with decreasing phase angle for all the different spectralon diffuse samples. The largest CPR values were observed for the most reflective samples while lower CPR values were observed for relatively darker analog pucks. The maximum CPR values were observed at exact zero phase angle for all the sample pucks.

For all the reflective samples, fluctuations due to systematic and random errors were observed all throughout the dataset. The CPR values for the spectralon samples were relatively noisy due to laser instability, alignment errors and small changes in the laser footprint on the sample, these issues were discussed in the chapter 'Error sources and mitigation'.

5.2.3 Alumina Samples

In this section we shall observe the CPR measurements conducted over range of near zero phase angles for powdered alumina samples. To observe wavelength scale roughness among these scatters, the particle sizes were selected to be in the vicinity of the laser source wavelength: 1.064 μm. The table below lists the wavelength to particle size ratios for different alumina samples under observation.

Laser Source Wavelength = 1064 nm or 1.064 μm		
Grain Size μm	Size to Wavelength Ratio	Intensity at 0°phase relative to 5% Spectralon
0.1	0.094	17.35
1.0	0.94	18.18
2.1	1.97	19.27
4.0	3.79	17.48

Table 5.4: Particle Size/Wavelength Comparison for Alumina Samples

From table 5.4 it can be observed that the closest grain size to the source wavelength was 1.0 μm, while the other grain sizes were relatively smaller or larger. The intensity values for the alumina grain sizes were normalized with respect to 5% Spectralon sample at zero degree phase for reflectivity comparison. The relative signal intensity of the alumina samples were in the same range as the 99% Spectralon reflectivity which indicates that the samples were highly reflective.

The analog signals were measured from the highly reflective alumina samples over a range of phase angles, the findings are shown in the figures below. The measurements were repeated several times for each individual grain size over a period of time with repeatable results.

Figure 5.8 illustrates the increase in CPR values for both $0.1\mu m$ and $1.0\mu m$ grain sizes with decreasing phase angle. The polarization ratios for both the grain sizes gradually fluctuates till 1-2°phase angle after which they increase rapidly with the maximum value at zero degree phase. With the signal wavelength of $1.064\mu m$ both the grain sizes are smaller than wavelength with particle size $1.0\mu m$ being the closest.

The estimated grain sizes $2.1\mu m$ and $4.0\mu m$ are much larger than the wavelength of the signal. The maximum CPR values are exactly at zero degree phase angle similar to other grain sizes. The largest CPR value among the alumina samples are for grain sizes that are closest or in few sizes of the wavelength. This effect can also be observed in the Nelson's study [37] for different alumina grain sizes.

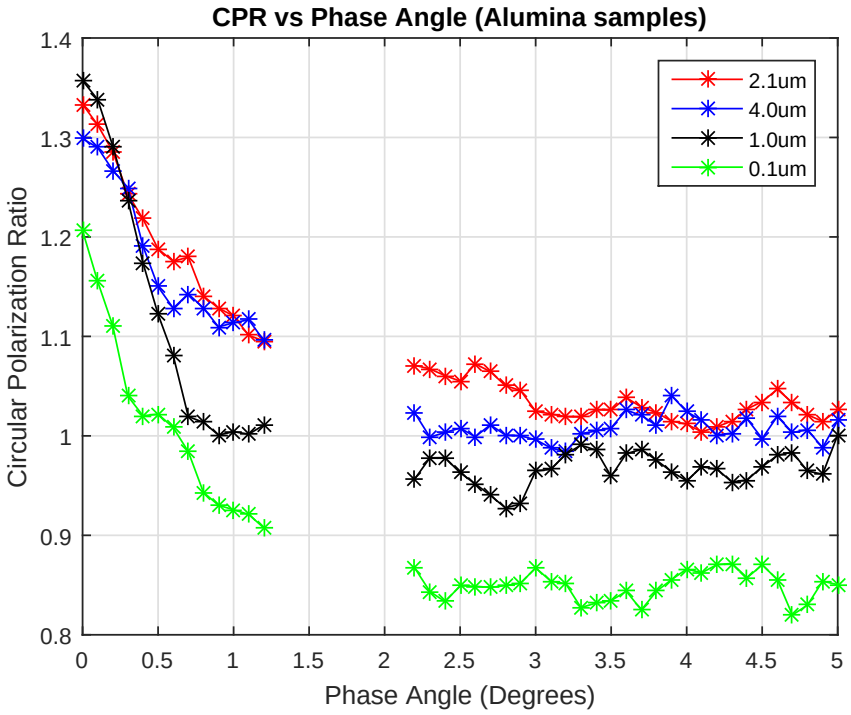

Figure 5.8: CPR vs Phase Angle for all Alumina Powdered Samples

For particle sizes much larger than the wavelength of the incident signal, the minimum CPR values are at much larger phase angles compared to the particle sizes that are close to the wavelength of the signal. For particle sizes much smaller than the incident wavelength, the minimum CPR was much lower in value than the other particle sizes. The CPR maximum was highest for the particle size closest to the wavelength of the incident signal, $1.0\mu m$ while the lowest CPR was for the smallest particle size, $0.1\mu m$.

From the observed CPR trends we can validate the presence of opposition effects mainly the coherent backscattering effect. For all the highly reflective alumina samples, large polarized opposition surges at near zero phase angle which are indicative of the opposition effects were observed. Moreover, the high CPR values near zero phase which implies that the same sense of polarized signal were observed that occur due to multiple scattering instead of single reflected light.

5.2.4 Signal Intensity for Spectralon and Alumina Samples

Spectralon Signal Intensity

The detector signal intensity for Standard Spectralon samples with decreasing phase angle were plotted in signal intensity phase curves shown below. Brighter spectralon targets had a more steeper sloping compared to darker spectralon pucks which had relatively low intensities with gradual sloping as phase angle decreased from 5-0°.

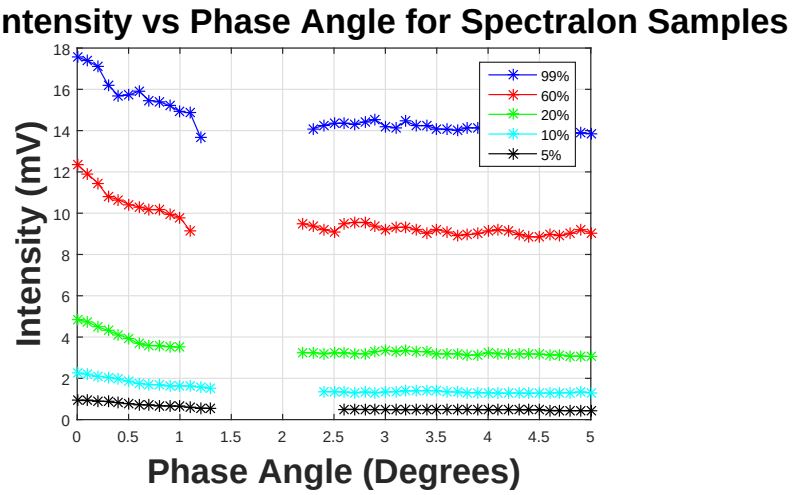

Figure 5.9: Signal Intensity vs Phase Angle for Spectralon Samples

The signal intensity values for all the Spectralon samples under study followed a general trend of increase with decreasing phase angles as shown in figure 5.9. The intensity values for brighter reflective samples were much higher than the darker samples, as expected. For phase angles less than 1.5°, the signal intensity values increased in non-linear nature compared to the linear fluctuating increase between 2.5-5°phase angle. The highest intensity values for all the samples were observed at exactly zero degree phase angle. For highly reflective samples the amount of opposition surge was higher for the brighter samples compared to the darker samples as expected. Since brighter samples reflect more, the CBOE is much easily observed in comparison to darker samples that still show opposition surge.

Alumina Signal Intensity

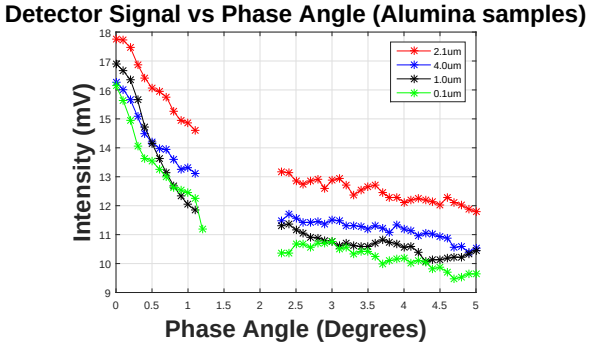

(a) Alumina Signal Intensity

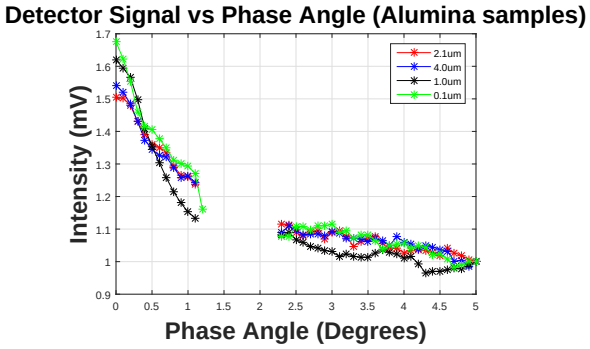

(b) Alumina Normalized Signal Intensity

Figure 5.10: Signal Intensity vs Phase Angle for Alumina Samples

Figure 5.10a shows the brightness from 0-5 degrees phase angle for different particle sizes. Opposition surges of 60% were observed for particle size fractions within a few wavelengths of the incident signal. The relative intensity of the opposition surges decrease with particle sizes much smaller or larger than the incident signal. It was observed that opposition surges increased at phase angle of 2°with the maximum value occurring at exact zero phase angle. The region between 0-2°phase angle was also where the CPR value increased with decreasing phase angle indicating the presence of Coherent Backscattering Opposition effect.

5.2.5 Liquid Samples

In this section we shall observe the CPR vs phase angle values for liquid samples presented in section 4.4.2. For this study two liquid solutions were observed: powdered alumina sol in glycerol medium and suspended beads solution. Observations from the liquid samples study would enable future measurements with similar sample sets to be undertaken helping us understand important parameters regarding the icy regoliths.

Due to large specular reflections from interactions with the incident liquid surface, the measurements for liquid samples were taken at larger incidence and emergence angles. The arm platform was moved to 15°emergence angle while the caddy platform was moved from 15°- 20°incidence angle.

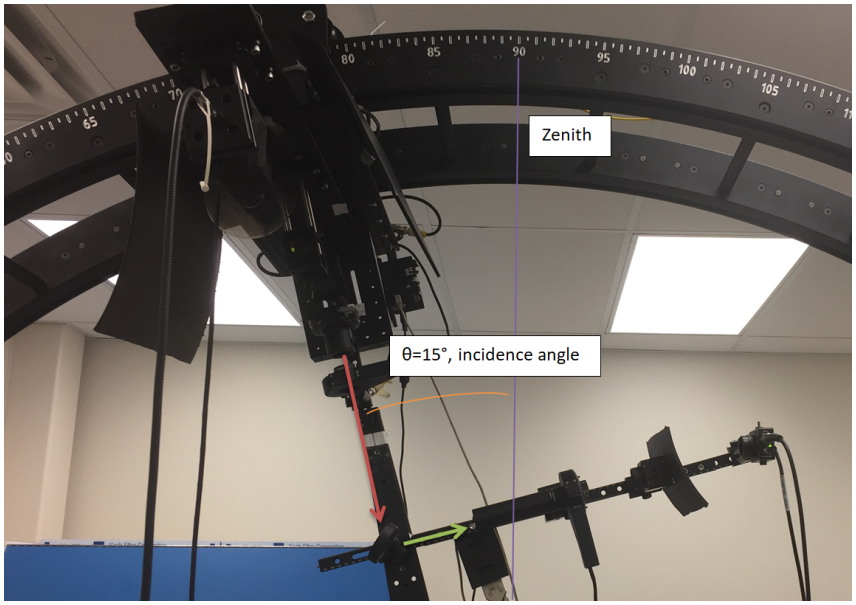

Figure 5.11: Instrumentation setup for Liquid Samples

The signal received from the liquid samples were lower in intensity compared to the powdered samples as they were observed at larger emergence angles. The intensity values decreased with increasing phase angle similar to previous powdered measurements.

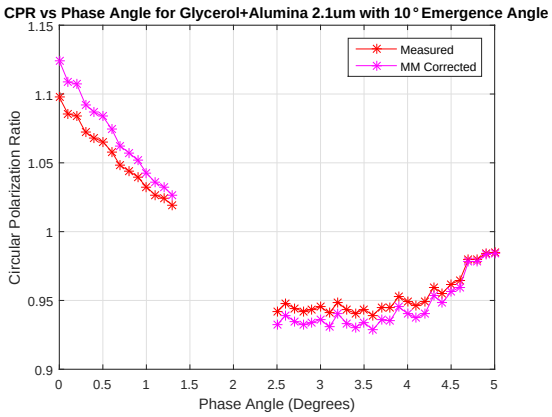

(a) 10° Emergence

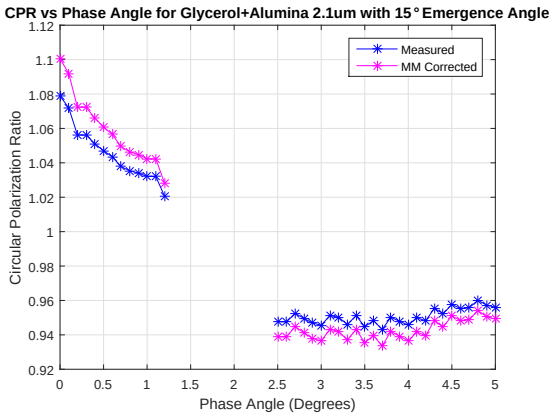

(b) 15° Emergence

Figure 5.12: CPR vs Phase Angle for Glycerol+Alumina2.1μm with 10° and 15° Emergence Angles

Figure 5.12(a) and (b) shows the CPR values with decreasing phase angle for Glycerol and Alumina solution with different emergence angles. With the change in emergence angles the incidence angles were also changed to ensure that the same 0-5 degree phase angle measurements were acquired. The plots show increasing CPR values with decreasing phase angles for both the emergence angles, indicative of presence of CBOE. The CPR values between 3-5°are relatively low compared to the higher values after 1°phase. As the incident signal propagates from air to glycerol its wavelength shortens due to change in medium. The particle size appears larger to the shorter incident wavelength compared to the powdered sample which resulted in CPR maximum values being lower.

The phase trends for the liquid sample gradually increased after 1°phase compared to the same powdered alumina sample increasing exponentially near zero. The CPR values for 15°emergence angle were lower than 10°emergence angle indicating presence of indirect specular noise component in the output signal. As the incident signal interacts with the glycerol/alumina solution it encounters a smooth glycerol surface that results in some of the incident signal reflecting in the specular direction. Surface roughness from alumina particles suspended on the smooth glycerol surface can cause some unwanted

diffuse reflections. The effects from these specular and diffuse reflections can be reduced by observing the liquid samples at larger incidence and emergence angles, such that the specular reflections are propagating opposite to the emergence angle. By performing additional measurements with smaller emergence angle increments, relation between CPR change and emission angle can be explored.

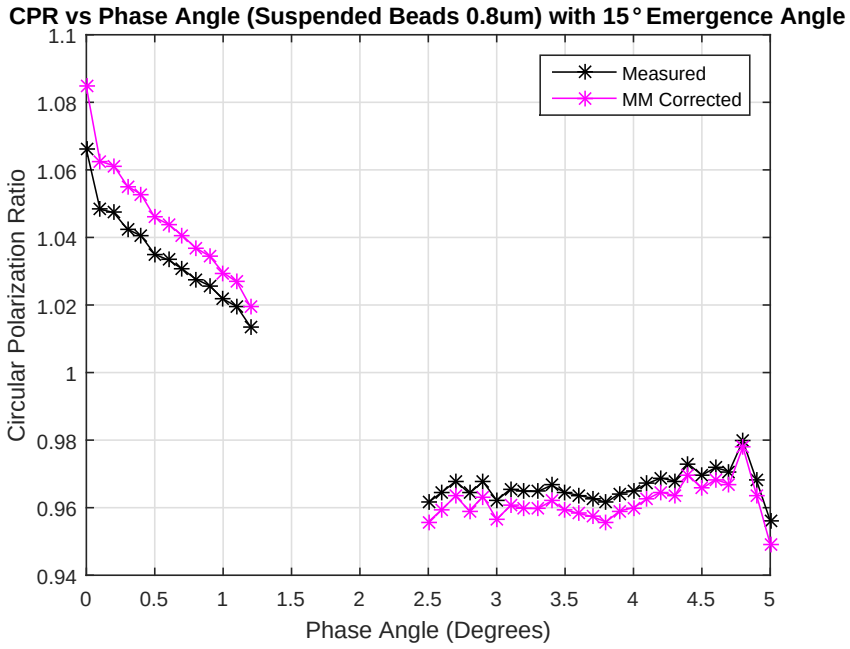

Figure 5.13: Polystyrene Beads Suspension at 15° Emergence Angle

Figure 5.13 shows the CPR versus phase angle measurements for aqueous milky white suspended beads with nominal grain size of 0.8 μm. The measurement was taken at 15°emergence angle with incidence angle going from 15-20°on the Goniometric instrument. With the changed wavelength propagating through the liquid medium the wavelength to grain size ratio was close to 1. The CPR values increased with decreasing phase angle which indicates the presence of CBOE scattering rather than SHOE. The values from 3-5°range are lower than the 0-1°phase indicating that the majority of increase in the CPR occurs during 1-2.5°.

From our previous studies on alumina samples, we observed that the multiple scattering effects are often measured near zero phase angles where the reflectance and CPR values increase rapidly. The slow nature of increase in CPR for suspended beads indicates that some specular or unwanted reflections were still observed at 10-15°emergence angles. Observing similar suspended beads data for larger emergence angles would provide us with useful information regarding the effects of multiple scattering for liquid solutions.

The suspended beads measurements were corrected with the beam splitter Mueller matrix for eliminating any polarization changing effects upon reflection. The measured and corrected values are plotted in Figure 5.15, the CPR values show small increase with decreasing phase angle after the Mueller matrix correction.

5.3 Mueller Matrix Measurements

In the experimental setup, the incoming signal was propagated and reflected through the beam splitter mounted on the arm platform. Several inconsistencies were measured from the received backscatter due to uneven s and p polarization reflections from the beam splitter. These inconsistencies would change the Stokes parameter of the signal when interacting with the beam splitter. The polarization change caused by the beam splitter on the signal was analyzed using the Mueller matrix of the beam splitter.

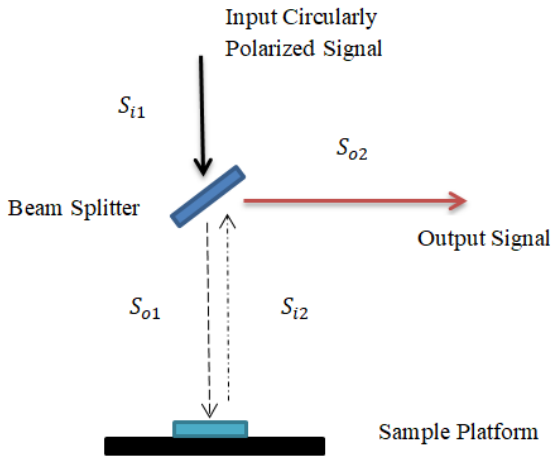

Figure 5.14: Variations in the polarized signal propagating and reflecting from the beam splitter

Figure 5.14 shows the signal propagating through the beam splitter before and after interacting with the sample platform with individual polarization states represented through different Stokes vector. The incoming signal S_{i1} was right/left handed circularly polarized which changes its polarization state after propagating through the beam splitter to S_{o1}. After diffused scattering from the sample platform the backscattered signal can be represented as an incoming signal towards the beam splitter as S_{i2}. The signal changes its polarization state to S_{o2} after reflecting from the 45°angled beam splitter. The beam splitter changes the polarization state of the signal twice, this change can be measured by

observing the Mueller matrix of the beam splitter. The relationship between the different polarization states of the signal are as follows:

$$S_{o1} = M_1 * S_{i1}; \qquad S_{i1} = inv(M_1) * S_{o1}$$

$$S_{o2} = M_2 * S_{i2}; \qquad S_{i2} = inv(M_2) * S_{o2}$$

Where M_1 and M_2 are Mueller matrices of the beam splitter.

The Mueller matrix of the beam splitter was calculated for the first case where the incoming signal propagated through the beam splitter and was incident on the sample platform. Using the dual rotating quarter wave plate technique the intensity values were measured and Fourier analyzed to calculate the Mueller matrix as shown in section 3.2.1.

$$M_1 = \begin{bmatrix} 1 & -0.0401 & 0.2138 & 0.0032 \\ -0.0453 & 0.7694 & -0.0033 & -0.0003 \\ 0.0017 & -0.0033 & 0.7601 & 0.0008 \\ 0.0069 & 0.0112 & -0.0165 & 0.8763 \end{bmatrix}$$

The Mueller matrix M_1 resembles the no sample identity matrix from the calibration procedure. A signal propagating through the beam splitter would retain much of its linear and circular polarization state as the diagonal elements are positive and close to unity while the off-diagonal elements are near zero. This implies that the polarization state of the circularly polarized signal S_{o1} incident on the sample platform would be similar to the polarization state of the signal S_{i1} generated from the polarizer and quarter wave plate. For a completely circularly polarized signal propagating through the beam splitter, 87 % of the polarization state will be retained.

Secondly, using the observed backscatter signal S_{o2} and the second Mueller matrix M_2, the original diffused signal S_{i2} from the sample surface was calculated. By calculating the polarization state of the signal before it reflected from the beam splitter eliminated the effects of polarization change from the beam splitter. The method of eliminating the

polarization change from an optical element by calculating the Stokes vector before the interaction can be refereed to as Mueller matrix correction.

$$M_2 = \begin{bmatrix} 1 & -0.0233 & 0.0257 & 0.0122 \\ 0.2350 & 0.2517 & -0.7709 & -0.0832 \\ 0.0810 & -0.7794 & -0.2454 & -0.0965 \\ -0.0302 & 0.0497 & 0.1011 & -0.8539 \end{bmatrix}$$

The degree of change in the polarization state of the backscattered signal from the sample platform reflecting towards the analyzer can be represented through the second Mueller matrix M_2. The m44 element in the matrix represents the degree towards which the circular polarizations state would change. As the element is negative, it would flip the polarization state of incoming signal from right-handed circular to left-handed circular and vice-versa. The value of m44 is near unity which implies that it would allow only 85% of the original polarization state to propagate. The low values for m22 and m33 elements and high negative values for m23 and m32 indicates that the linear and 45°polarization state of the output signal would be skewed.

A signal propagating through the beam splitter would not undergo much change in the polarization state however a signal reflecting from the beam splitter would have a significantly different polarization state. This change in the state of the output signal would not allow for correct interpretation of the backscatter results. To avoid this error, the Mueller matrix correction technique was applied and the effects of the beam splitter were eliminated from which the original backscattered data was calculated. The S_{i2} signal was calculated for all the Alumina and Spectralon samples from the observed S_{o2} signal and M_2 Mueller matrix as shown below:

5.3.1 Spectralon CPR trends with Mueller Matrix Correction

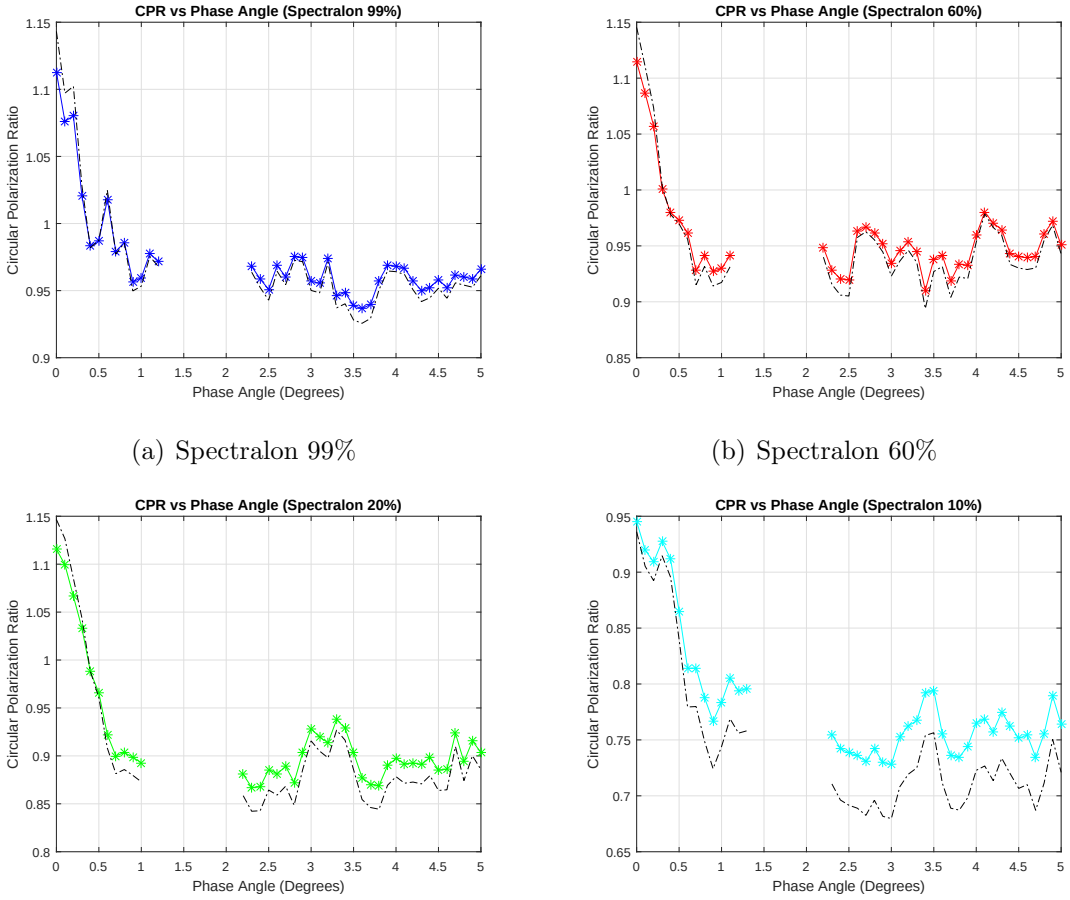

(a) Spectralon 99%

(b) Spectralon 60%

(c) Spectralon 20%

(d) Spectralon 10%

Figure 5.15: CPR vs Phase Angle for Standard Spectralon Diffuse Reflectance Pucks with Mueller Matrix Correction. Dotted line shows the corrected values while solid line shows the observed values

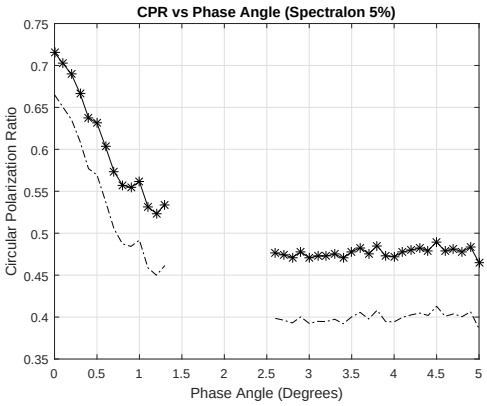

(a) Spectralon 5%

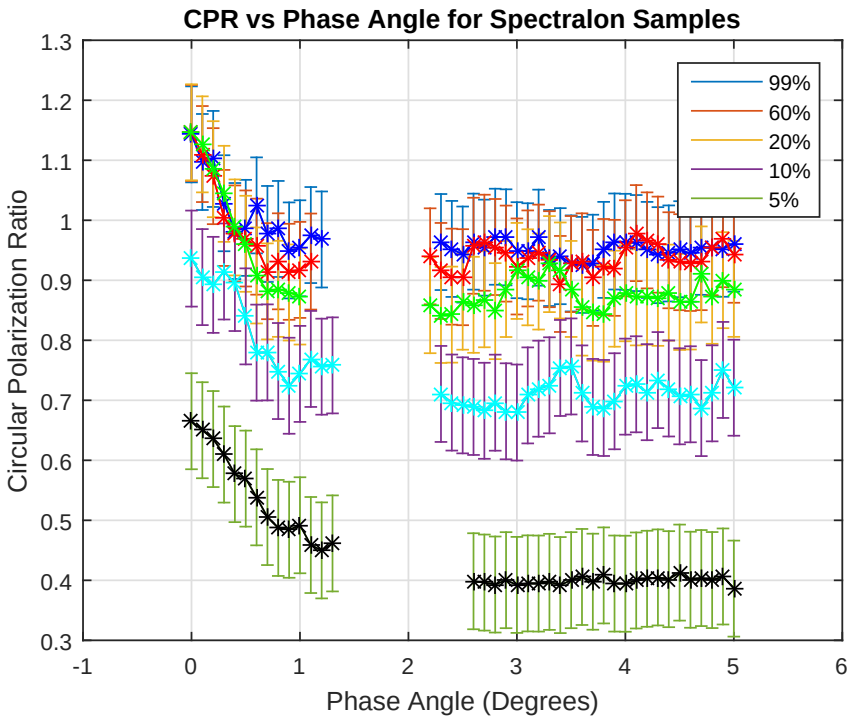

(b) Spectralon Samples

Figure 5.16: CPR vs Phase Angle for Standard Spectralon Diffuse Reflectance Pucks with Mueller Matrix Correction and Systematic errors.

Figures 5.15 and 5.16 show the CPR values for Standard Spectralon reflectance samples before and after applying the M_2 Mueller matrix correction. As the CPR value were calculated from the S_4 Stokes parameter of the backscattered signal, the relative trend for the samples remained the same. For Spectralon samples with reflectance >20% we observe the corrected CPR values at zero phase angle increase in magnitude while the minimum values are much lower. For darker Spectralon samples the corrected CPR values were much lower in comparison as their observed S_4 parameters were lower in magnitude.

Figure 5.16b shows the relative CPR values for all the Spectralon samples, with higher reflectance samples having higher polarization ratios while lower reflectance samples having much smaller polarization ratios.

5.3.2 Alumina CPR trends with Mueller Matrix Correction

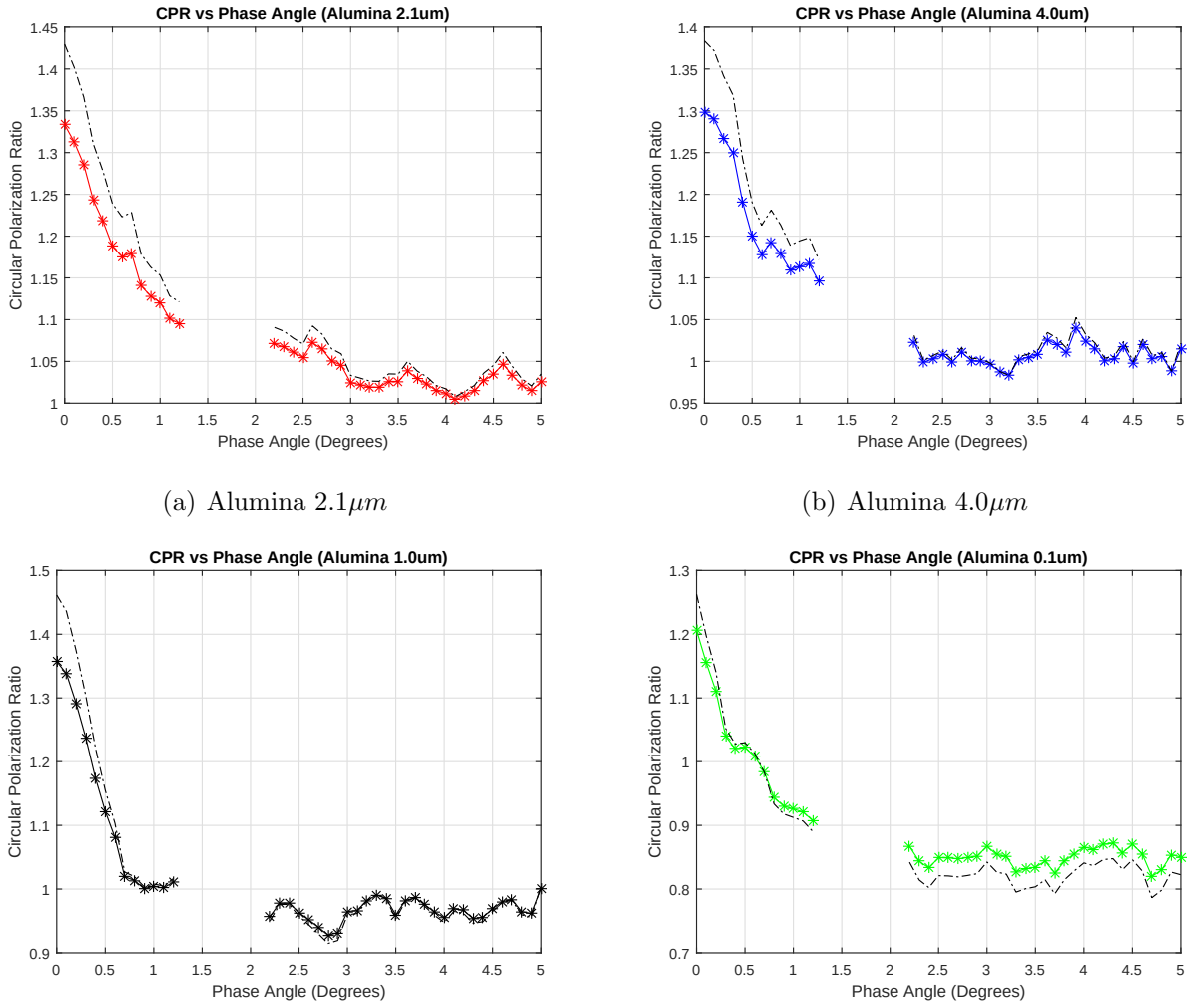

(a) Alumina 2.1μm

(b) Alumina 4.0μm

(c) Alumina 1.0μm

(d) Alumina 0.1μm

Figure 5.17: Alumina Powdered Samples with Mueller matrix correction. Dotted line shows the corrected values while solid line shows the observed values.

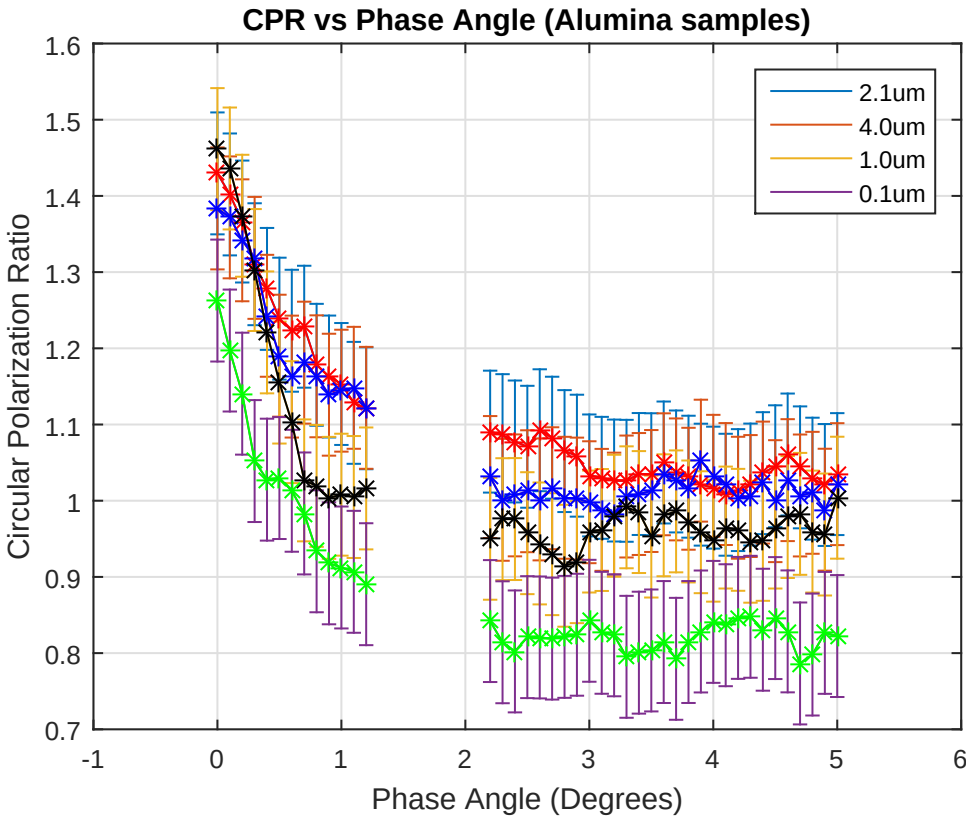

(a) Alumina Samples

Figure 5.18: CPR vs Phase Angle for Alumina Powdered Samples with Systematic Errors

Similar results were observed when applying the Mueller matrix correction to the alumina samples as compared to Spectralon pucks. The overall CPR values at zero phase angle increased for all the powdered samples while their trends remained similar to previous results. The highest CPR value was observed for grain sizes closest to the wavelength of the incident signal while lowest CPR values were observed for grain sizes much smaller than the wavelength. Figure 5.18 shows the systematic errors in our experimental setup computed through addition of different error sources as shown in the next chapter. Large variances in systematic errors and lack of repeated data did not allow us to compute the random errors in the dataset.

6 Error Sources and Mitigation

Mitigating the error sources are very important as they affect the data's repeatability and accuracy. In this chapter we shall explore the error sources encountered during the experimental setup and the data acquisition process, the mitigation techniques employed for these error sources will also be discussed.

6.1 Instrumentation Error

In this section we shall discuss the instrumentation challenges encountered while assembling the optical system on the Goniometer and various mitigation techniques applied to propagate these error sources. Instrumentation errors are often encountered when initially setting up the instrument and can cause systematic and random errors in the measurements, if not correctly mitigated. Here are some of the common instrumentation errors encountered during this experiment:

6.1.1 Laser Beam Misalignment

Misalignment of the laser beam path for an optical assembly was a common instrumentation error encountered during the initial system setup. This error originates when assembling an optical system with multiple off angle components where the beam path often undergoes reflections. In this experiment we encountered misalignment issues due to compatibility differences in the optical component mounts when initially assembling the system. Figure below shows the angling of laser source platform that impacts the location of the beam incident on the 45°mirror thereby causing misalignment.

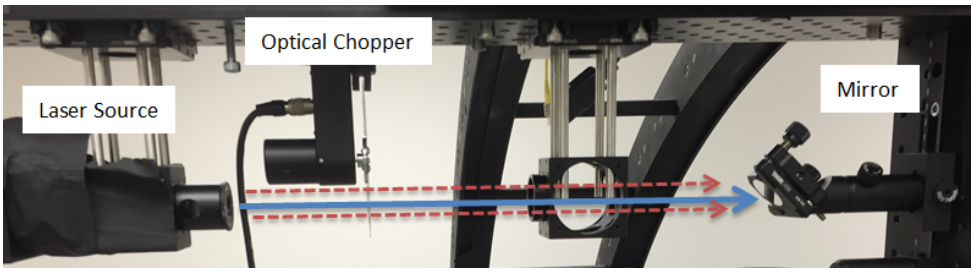

Figure 6.1: Offset Reflections resulting from Laser misalignment issues

Due to incorrect laser beam alignment the incident beam interacted with the 45°mirror at an off-center angle resulting in the beam propagating incorrectly throughout the optical component paths. Beam misalignment was easily observed by placing detector targets at the expected propagation paths and measuring their deviations from the center. Small deviations from the expected propagation paths were difficult to observe and required optical mounts to be placed with high precision.

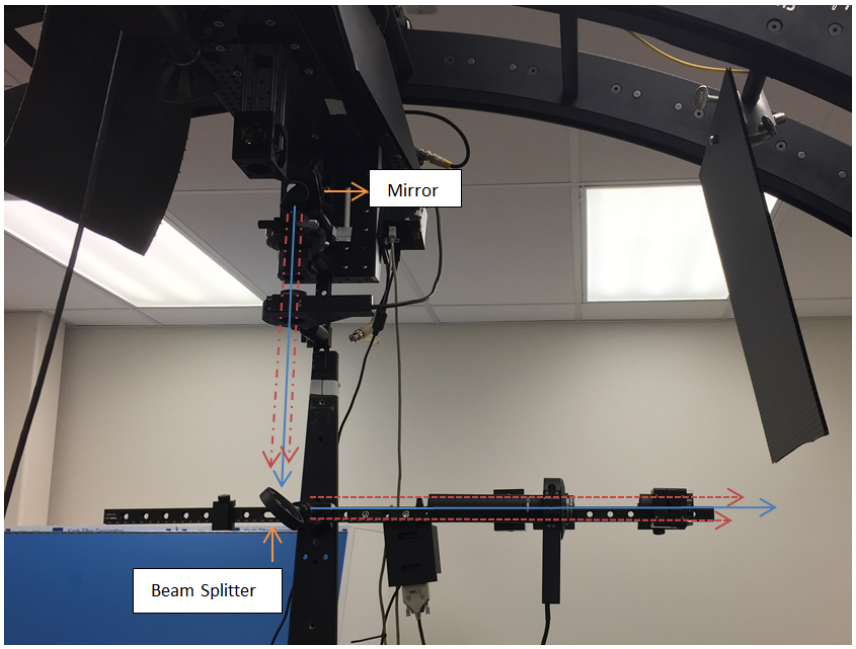

Figure 6.2: Offset Reflections propagating through incident and reflected beam paths due to Laser misalignment

Mitigation

The beam misalignment errors were mitigated by precisely measuring the beam propagation distances and angles with digital levels and vernier calipers. The optical components that reflected or interacted with the laser beam were accurately mounted on the Goniometric assembly. Target detectors were placed at sample platform and points of reflections to ensure that the beam propagation path was aligned. Focusing lens were mounted in the optical assembly so that the laser beam divergence could be avoided. Beam divergence occurs when an electromagnetic beam increases in beam diameter with distance from the optical aperture.

6.1.2 Stray Light Reflections

The Goniometric optical assembly measured near zero backscattering reflections from various samples along with secondary stray laser beam reflections from mounting surfaces. The stray reflections originated from light interacting with the outer edge mounts of the lens holders and light backscattered from sample surface reaching the detector. These effects produced random errors in the recorded measurements and would often cause outliers in the dataset.

Mitigation

The light reflections propagating into the analyzer were challenging to detect as they had different intensities and polarization states. Firstly, it was ensured that the beam propagated through the center of all the optical components and the beam width was smaller than the diameter of the optical components. Secondly we measured the changes in signal intensity for a standard sample at a fixed phase angle by individually blocking the optical components with white reflective sheets. The stray light reflections were more prominent around the beam splitter and sample surface regions as expected. These reflections were mitigated in the following ways:

- Longer rail was added on the arm platform and the analyzer components were

moved away from the beam splitter and individual analyzer components. Effects from stray reflections that propagated into the beam bath were significantly reduced as the components were apart from each other, while the longer rail added more stability.

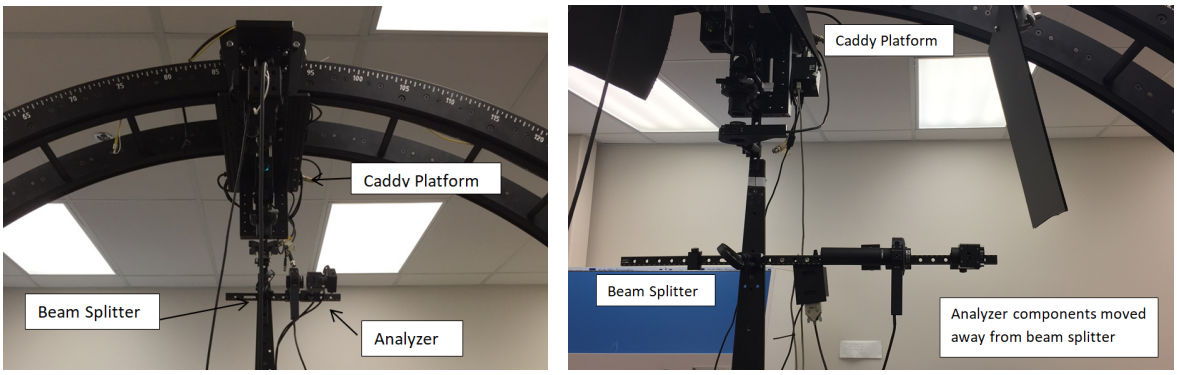

(a) Older Setup (b) Recent Setup

Figure 6.3: Comparison between old and new analyzer mounting setup

- Black absorbing blinds were mounted on locations where stray reflections were expected to propagate into the detector.
- The detector was offset by a small angle such that the reflections from the detector surface would not propagate back into the optical system on the same optical path where the backscattered signal was propagating.

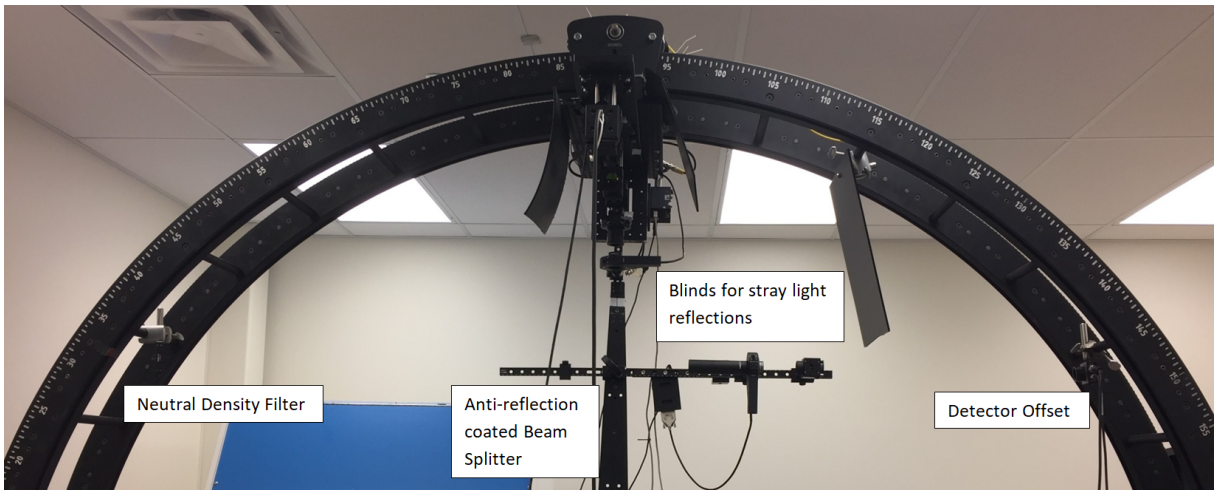

Figure 6.4: Stray light mitigation techniques employed in the instrumentation setup

- Anti-reflective coated beam splitter was used in the instrument to eliminate back reflections from the sample into the input signal.
- Neutral Density filters with high optical densities were placed at 45°angle opposite to the analyzer section for eliminating the secondary beam splitter reflections. Backscattered signal from the sample platform would split into a primary signal towards the analyzer and secondary beam that was not used.

6.1.3 Backscattering Losses

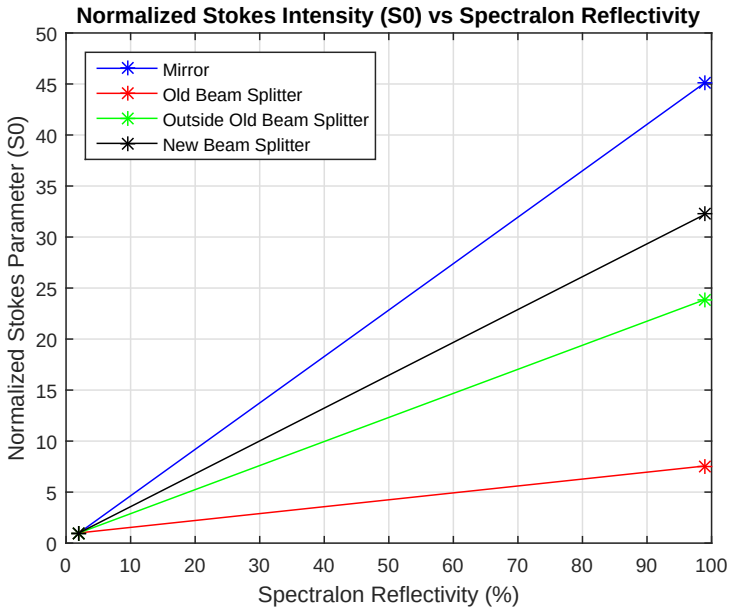

Figure 6.5: Backscattering Intensities for different reflectors with standard sample pucks

The optical component (beam splitter) that collected the backscattered radiation from the sample source and directed it towards the analyzer lost some of the diffused signal upon reflection. The normalized intensity Stokes parameter (S0) of standard spectralon pucks (99% and 2%) were measured for different optical components and plotted vs spectralon reflectivity (R). The older beam splitter had higher backscattering losses compared to the newer beam splitter due to presence of small dust specks and absence of anti-reflective coating. The beam splitter split the beam 50-50 twice, firstly upon incidence and secondly when reflecting the diffused signal towards the analyzer. Due to the inaccurate S and P polarization propagation through the beam splitter, large inaccuracies in the polarization states were encountered for the diffuse signals.

$$\frac{R_{99\%}}{R_{2\%}} = \frac{99}{2} = 49.5$$

The spectral reflectivity for both the 99% and 2% pucks were observed when the

diffused radiation were reflected from different optical components. As shown in figure 6.5, the mirror had the highest spectral reflectivity ratio of 45.13 while the beam splitters had relatively low reflectivity ratios. The relatively low spectral reflectivity for beam splitters could not be corrected however by measuring the Mueller matrices of the beam splitter, the S and P polarization inaccuracies were mitigated.

6.2 Calibration Error

In this section we shall discuss the errors that originated while calibrating the optical system before performing measurement runs. Calibration of the optical system plays a major role in obtaining repeatable measurements for a sample set over a period of time. Proper calibration of the optical instrument ensures that the datasets of CPR vs Phase angle measurements for different samples can be compared and contrasted. Some of the calibration issues encountered during this experiment and their mitigation techniques are listed below:

6.2.1 Zeroing Goniometer Instrument

The CPR and Stokes parameters for a particular sample were measured by moving the caddy platform of the Goniometer from 0°-5°angle range. Due to inherent limitations with the Goniometer program, the caddy platform had to be re-centered when turning on the goniometer. The axis marking on the Goniometer platform would only be accurate to ±0.1°as shown in the figure below. This would result in trend differences during the observation of CPR vs phase angle measurements for identical samples over large datasets.

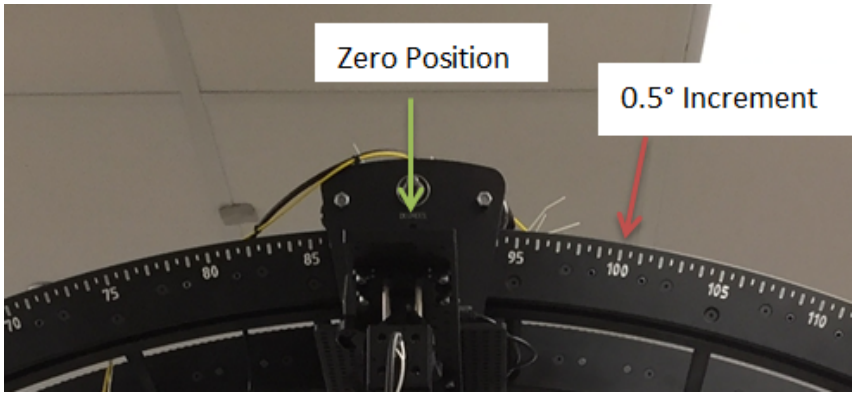

Figure 6.6: Caddy platform zero position with limited accuracy

Mitigation

The accuracy for caddy platform positioning was improved by measuring the axial tilt of the platform with respect to the sample platform by a digital level. By aligning both the platform values and centering the incident beam on the sample platform the zeroing issues were mitigated. The successive caddy calibrations were positioned to the measured level zero reading before all the measurements were performed.

6.3 Measurement Error

In this section, the uncertainties related to measurement acquisition procedures and ways to mitigate the errors are discussed. There were two main types of data acquisition errors encountered during the sample measurement, detector signal stability and motor movement. The two errors are related to the instrument and cause very small deviations in the signal.

6.3.1 Detector Signal Stability

The Goniometric photopolarimeter observes low intensity backscattering signal in the μV range from diffuse scattering off powdered samples. The high gain detector measuring the backscattered signal was designed with a built-in low-noise transimpedance amplifier (TIA) followed by a voltage amplifier. The detector was connected to a dual signal Lock-in amplifier that dictated the limited bandwidth of the detector. The detector was used in two switchable gain settings 0 dB and 10 dB as per specifications in the table below:

PDA 100a Detector				
Wavelength	Gain	Bandwidth	NEP	Noise (RMS)
340-1100 nm	0 dB	1 mHz $\leq$ F $\leq$ 50 kHz	27pW/Hz$^{1/2}$	254μV
	10 dB	1 mHz $\leq$ F $\leq$ 50 kHz	11pW/Hz$^{1/2}$	261μV

Table 6.1: PDA100A Hi-Gain Detector Specifications

The diffused signals from the sample platform were of the magnitude $\sim 100\mu V$, while the observed levels were $\sim 0.5\mu V$. The overall detector stability were improved by measuring the data under low gain settings with higher time constant of the Lock-in Amplifier.

6.3.2 Motor Movement

The quarter wave plate rotation angles were controlled using the Motor control software discussed in the Data Acquisition procedure. The DC motor utilized motor control software which inherently had a backlash error. As the angular position of the quarter wave plate was very important for measuring the correct Stokes parameters for a polarized signal we observed its impact on the measurements.

The motor control software had $\pm 0.05^{\circ}$backlash error for every 5°step size increment that translated to $\pm 0.3\mu$V detector error over $360^{\circ}$of rotation.

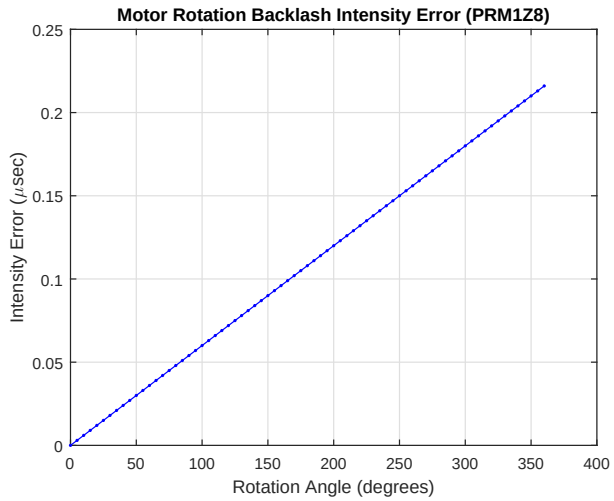

Figure 6.7: Rotation Stage Backlash Intensity Error

6.4 Computation/Correction Error

6.4.1 Mueller Matrix Error

Mueller Matrix describes the optical properties of an optical element but the true nature of the element may be obscured by errors inherent in the polarimeter optical system. Dennis Goldstein describes the error compensation method for known errors caused by the inability to align the polarizing elements precisely. Errors in orientation, alignment and nonideal retardation elements are included in this analysis. [20] [5]

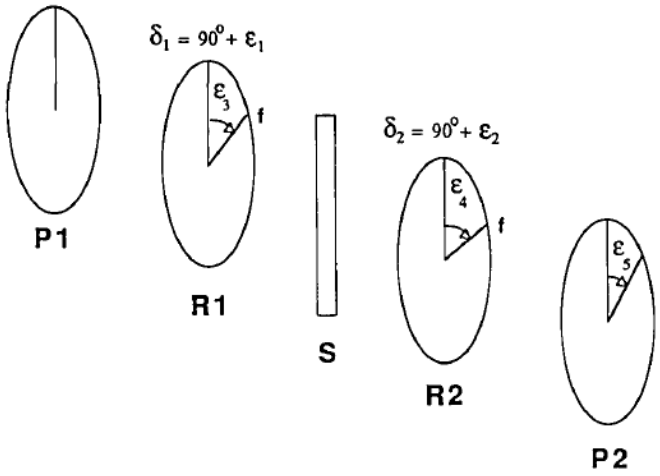

Figure 6.8: Retardation errors ϵ_1 and ϵ_2, orientation errors ϵ_3, ϵ_4, ϵ_5 from the dual rotating retarder technique

Firstly the polarimeter was operated with no sample employing the Dual rotating quarter wave plate technique. The Fourier coefficients were acquired from the measured modulated intensity from which the Mueller matrices were calculated. As no sample was present in the polarimeter, the resulting Mueller matrix was an identity matrix with all off-diagonal elements being zero. The Fourier coefficients are functions of the errors as follows:

$$a_0 = \frac{1}{4} + \frac{(1-\epsilon_1)(1-\epsilon_2)}{16}$$

$$a_2 = \frac{(1+\epsilon_1)(1-\epsilon_2)}{16} + \frac{(1+\epsilon_1)(1-\epsilon_2)\epsilon_3\epsilon_5}{2}$$

$$a_8 = \frac{(1+\epsilon_1)(1+\epsilon_2)}{16}$$

$$a_{10} = \frac{(1-\epsilon_1)(1+\epsilon_2)}{16}$$

$$b_2 = -\frac{(1+\epsilon_1)(1-\epsilon_2)\epsilon_3}{4} + \frac{(1+\epsilon_1)(1-\epsilon_2)\epsilon_5}{8}$$

$$b_4 = \frac{(\epsilon_4 - \epsilon_3 - \epsilon_5)}{4}$$

$$b_6 = \frac{(\epsilon_5 - \epsilon_3 - \epsilon_4)}{4}$$

$$b_8 = \frac{(1+\epsilon_1)(1+\epsilon_2)(2\epsilon_4 - 2\epsilon_3 - \epsilon_5)}{8}$$

$$b_{10} = -\frac{(1-\epsilon_1)(1+\epsilon_2)(2\epsilon_4 - \epsilon_5)}{8}$$

The above equations were inverted to solve for the errors in terms of Fourier coefficients with no sample measurement.

$$\epsilon_1 = 3 - 8(a_0 + a_{10})$$

$$\epsilon_2 = \frac{4(a_0 - a_{10}) - 1}{1 - 4(a_0 - a_{10})}$$

$$\epsilon_3 = -2(b_4 + b_6)$$

$$\epsilon_5 = \frac{8b_2}{(1+\epsilon_1)1-\epsilon_2)} + 2\epsilon_3$$

$$\epsilon_4 = \epsilon_5 + 2(b_4 - b_6)$$

Secondly, using the error-compensation equations and the known Fourier coefficients from no sample measurement the values for errors in the polarimeter were calculated. Lastly the systematic errors in the Fourier coefficients arising from imperfections are compensated by using the error-compensated equations with experimentally determined error values to obtain the error compensated sample Mueller matrix elements as a function of measured Fourier coefficients.

Systematic Errors	
Error	Value
ϵ_1	-1.26°
ϵ_2	-1°
ϵ_3	0.17°
ϵ_4	-0.32°
ϵ_5	-0.26°

Table 6.2: Alignment Errors from Mueller matrix calibration

Table 6.2 shows that ϵ_1 and ϵ_2 errors associated with the retardance of the quarter wave plate are the main sources of error in calculating Muller matrices. Other orientation error components such as quarter wave plate misalignment relative to measurement axis and polarizer misalignment are relatively smaller in magnitude.

6.4.2 True Retardance Error

The true retardance of the rotating quarter wave plate was calculated by using the cross-polarized method. The fast axis of the quarter wave plate was aligned to 45°and placed after the linear polarizer to generate RHCP or LHCP. Misalignment or inherent errors in the quarter wave plate would skew the circular polarization into elliptical polarization if the true retardance was not known. Using the cross-polarized method suggested by Goldstein, the quarter wave plate was inserted between two crossed linear polarizers. From the markings on the quarter wave plate the fast axis was moved 45°on either clockwise or counter-clockwise direction. When the angle between the fast axis of the wave plate and the X-direction is at 45°, the intensity after the analyzer can be expressed as a function of the retardance δ of the wave plate and angle α of the analyzer transmission axis with the x direction:

$$I(\alpha, \delta) = \frac{I_0}{4}(1 + cos(\delta)cos(2\alpha))$$

Measuring the intensity at 0°and 90°angle of analyzing polarizer the true retardance can be calculated as:

$$cos(\delta) = \frac{I(0°, \delta) - I(90°, \delta)}{I(0°, \delta) + I(90°, \delta)}$$

The primary advantage with the cross-polarized method was that it was independent of the source intensity. Using high precision rotation mounts for the linear polarizer and quarter wave plate allowed for precise measurements.

6.4.3 Least Squares Estimate

Due to the limitation in our experimental setup we were unable to acquire data between the intervals of 1.3°-2.2° phase angles. Using the method of least squares we interpolated a fit for the signal intensity and CPR phase curve. The fitted least squares approximation were interpolated from existing values before and after the missing dataset region. Using the least squares approximation we acquired very close approximations to what is expected in the missing regions.

Least squares interpolation was applied from five measurement before and after the missing phase angle region. The Matlab software implements a 1D interpolation function as shown below [26]:

$$y = interp1(x, m, xq, method, extrapolation)$$

Where y are the interpolated values, x are the data points, m are the missing values and method specifies the interpolation technique, in this case a 5th order polynomial was used to fit the phase curve.

$$y = a_0 + a_1 x + a_2 x^2 + a_3 x^3 + a_4 x^4 + a_5 x^5$$

The missing coefficient values for $a_0..a_5$ were calculated such that the sum of squares of the deviations were minimum,

$$R = \sum_{1}^{N} (y_i - (a_0 + a_1 x_i + a_2 x_i^2 + a_3 x_i^3 + a_4 x_i^4 + a_5 x_i^5))^2$$

The resulting least squares estimate were included in the Signal Intensity/CPR phase curves and plotted with increasing phase angle. Utilization of different degrees of polynomial resulted in different estimates for the missing values. The estimates were highly reliant on the acquired phase curve measurements and small deviations in the values would change the resulting estimates. The least squares estimate were solely for visual representation of the complete 0-5 degree phase curves and does not reflect the true nature of the behavior for the analog samples.

6.5 Error Analysis

In the previous sections we discussed various types of error sources encountered during the measurement procedure from which the calibration and computation uncertainties could not be completely eliminated. Partial derivative analysis can be used to calculate the absolute error in CPR and phase angle angle measurements as shown below. The main errors that affected the CPR data were uncertainties in intensity values caused by polarizer and retarder position (x), detector signal stability (y), retarder increment precision(z), sample spot variance (m) and goniometer calibration (n).

The function I = f(x, y, z, m, n) is a set of non-linear combination of variables x, y, z, m and n. Neglecting correlations and assuming independent variables leads to a common variance equation:

$$\partial I = \sqrt{(\frac{\partial I}{\partial x}\delta_x)^2 + (\frac{\partial I}{\partial y}\delta_y)^2 + (\frac{\partial I}{\partial z}\delta_z)^2 + (\frac{\partial I}{\partial m}\delta_m)^2 + (\frac{\partial I}{\partial n}\delta_n)^2}$$

Where, $\partial I/\partial x, \partial I/\partial y, \partial I/\partial z, \partial I/\partial m, \partial I/\partial n$ are errors in detector signal intensity caused by the listed uncertainties and $\delta_x, \delta_y, \delta_z, \delta_m, \delta_n$ are standard deviations for each respective variable. As the errors x, y, z, m, n are assumed to be independent the associated covariance terms in the above equation are zero.

As the CPR was calculated from the Stokes parameters that were computed from the intensity values as shown below:

$$\mu_C = \frac{S_0 - S_3}{S_0 + S_3}$$

$$\mu_C = \frac{I_{45}}{I_{135}}$$

By computing the errors in the intensity values and then propagating them into the CPR data we can compute the uncertainties in CPR measurements.

$$\partial C = \sqrt{(\partial I_{45})^2 + (\partial I_{135})^2}$$

Uncertainties in Intensity		
Error Source	Term	Value
Polarizer and Retarder Position	x	$\pm 0.5 \mu V$
Detector Signal Stability	y	$\pm 0.05 \mu V$
Rotating Retarder Increment	z	$\pm 0.05 \mu V$
Sample Spot Variance	m	$\pm 1 \mu V$
Goniometer Calibration	n	$\pm 0.5 \mu V$

Table 6.3: Uncertainties from various sources

The uncertainties in intensity values for different error sources are what causes the uncertainties in CPR data , with improved mounting techniques and more datasets we can better compute the standard deviations and errors for these measurements. Precision mounting tools exist that can measure polarizer and retarder position by ± 0.1 accuracy, addition of second detector can help normalize the intensity fluctuations caused due to laser source. Uncertainties in laser spot incident on different sample positions can be eliminated by positioning sample puck in a fixed mounting platform. The errors calculated above were systematic errors, random errors can be computed by performing several phase angle measurements for a single grain size and observing the outliers.

7 Assessment of Analog Observations

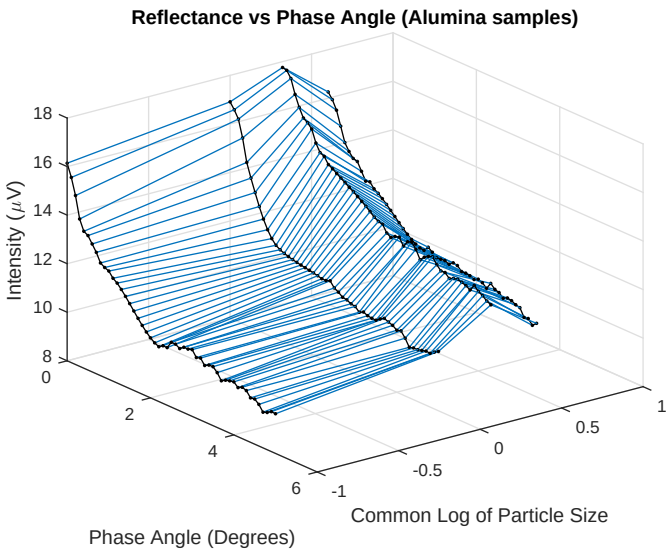

Figure 7.1: Reflectance vs Phase Angle for all Alumina Powdered Samples

The detector signal phase curves for all 4 different particle sizes of alumina oxide are shown in Figure 7.1. The detector signal of all the phase curves increases with decreasing phase angle with the maximum intensity at exact zero degree phase. The highest intensity values are observed for particle sizes that are close to the wavelength of the incident radiation. Particles sizes much smaller or larger than the wavelength have relatively low intensity values. Comparing the laboratory results with previous studies [37] on similar samples reveals close agreement between phase curve trends. Performing similar measurements for a larger variety of grain sizes would provide more information and allow for better understanding of signal intensity trends as a function of phase angle.

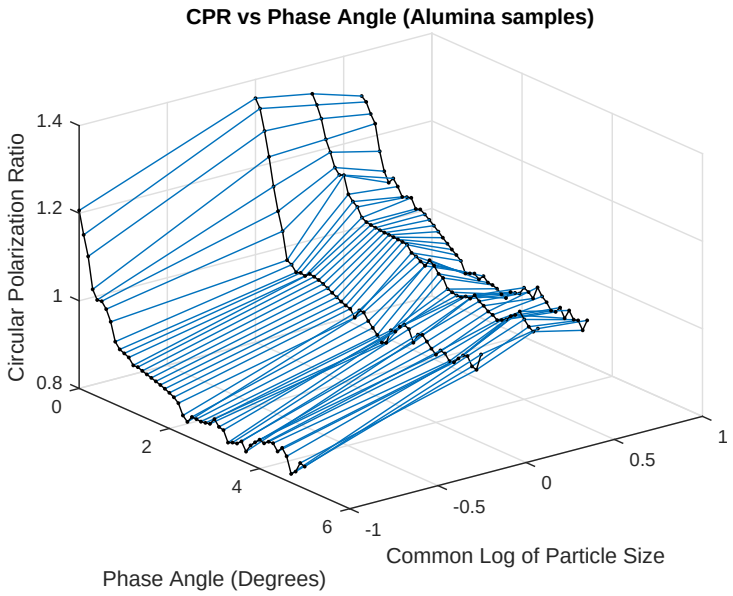

Figure 7.2: CPR vs Phase Angle for all Alumina Powdered Samples

The Circular polarization ratio phase curves for 4 different alumina oxide powdered grain sizes are shown in Figure 7.2. Similar trends in comparison to previous studies were observed from the laboratory measurements indicating the polarimeter was correctly setup. The highest CPR values were observed for particles sizes closest to the wavelength of the incident signal. CPR phase curves for all the samples were increasing from a minimum value with decreasing phase angle between 0-1 ˚which indicates the presence of coherent backscattering opposition effect. The shadow hiding opposition effects can be observed between the range of 1-5˚where the polarization values were relatively low before reaching a minimum and increasing thereafter.

Under presence of only SHOE the CPR phase curve would decrease with increasing phase angle till the minimum value was achieved. An increasing CPR trend was observed near zero phase angle which is indicative of the presence of coherent multiple scattering for highly reflective samples with grain sizes near the wavelength range.

Near zero phase angle the CPR values increased with decreasing phase angle for all the alumina grain sizes. Between 0-1°the CPR phase curve decreases before reaching a minimum and then continues to increase near zero phase angle. This drop in CPR is only observed under the presence of CBOE and results due to scattering for wavelength scaled or larger particles sizes.

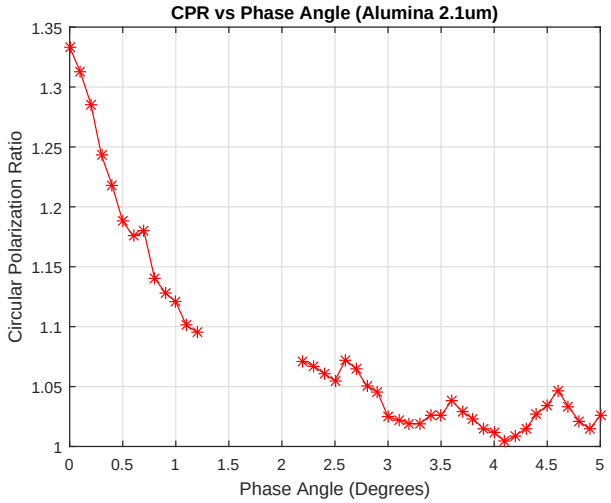

(a) Alumina 2.1μm

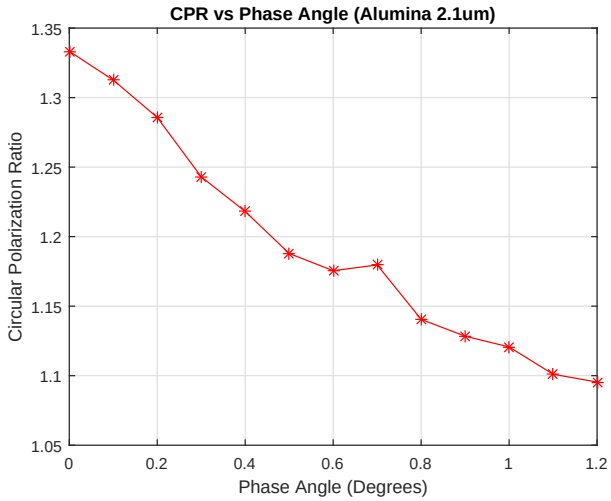

(b) Alumina 2.1μm Decrease Near Zero Phase Angle

Figure 7.3: CPR decrease near zero phase angle for alumina 2.1um grain size

A strong correlation between the location of minimum in the CPR phase curve as a function of particle size was observed. [44] The location of the first minimum value in the CPR phase curve was observed between the 0-1°phase angle where the decreasing phase curve would increase after a minimum value and decrease again. The particles sizes closer to the wavelength had CPR minimum at much larger phase angle compared to the particles sizes that were much larger than the wavelength. For particle sizes much smaller than the wavelength, the CPR minimum was observed at much smaller phase angles and the value itself was smaller compared to other grain sizes. Here are the details from the alumina samples:

Alumina CPR Phase Curves for 1.064 μm wavelength			
Grain Size	CPR Maximum Value	CPR Minimum Value	Minimum Location
2.1 μm	1.43	1.22	0.6°
4.0 μm	1.38	1.16	0.6°
1.0 μm	1.46	1.00	0.9°
0.1 μm	1.26	1.02	0.4°

Table 7.1: Maximum and minimum CPR values from Alumina phase curves

Observations from the alumina phase curves strongly agree with the previous undertaken studies related to the opposition effects and general behavior of the highly reflective samples.

8 Conclusion

The aim of this thesis has been to firstly design and construct an optical polarimeter capable of measuring polarization state of backscattered signal from analog samples and secondly to observe the properties of the analog samples and infer important information regarding the backscattering properties for highly reflective wavelength-scaled particles.

Chapter 2 provided a theoretical background related to the polarization state of an electromagnetic signal and important parameters that can be acquired from the polarized phase curves. Chapter 3 explored the different techniques through which the polarization state of a signal can be acquired and changed by optical components. Chapter 4 demonstrated the measurement procedure and optical setup employed on the long arm goniometric instrument for measuring polarized backscatter signal. Using the polarimetric instrument several analog measurements from different samples were acquired and corrected for polarization changes as listed in chapter 5. Errors associated with the instrumentation, calibration, measurement and computation are listed and mitigated in the error sources and mitigation section. The research objectives for this study were intended to guide the construction of the polarimetric setup and deduce important information related to the analog samples from the polarized backscattered signal.

The primary objective of the undertaken research was addressed by designing and assembling an experimental setup capable of measuring detector signal and Stokes vector for a backscattering signal over 0-5 degree phase angles. The detector signal and polarization measurements allowed us to calculate circular polarization ratio through which we observed the presence of opposition effects near zero phase angle. Coherent backscattering opposition effects were observed for all the highly reflective alumina grain sizes along

with the standard spectralon samples. From the near zero opposition surge we observed the dependence of the wavelength and particle size on the coherent backscattering trends.

For our second research objective, a rotating quarter wave plate technique was employed on the goniometeric instrument that was capable of measuring Stokes vector of a backscattered wave. By using different orientations of the linear polarizer and quarter wave plate with precision mounts we were able to provide highly polarized right and left circular incident signal on the sample platform for measuring the resulting backscatter. The Stokes vector of the backscattered signal provided important information regarding the polarization state of the wave with high accuracy.

For achieving the instrument capability of performing backscatter measurements over 0-5 degree range ,we employed a beam splitter that allowed for exact zero phase angle measurements. Due to mounting limitations phase angles from 1.3-2.2°could not be successfully acquired. Future work on eliminating mounting restrictions will allow us to measure seamless backscatter data from 0-5 degree phase. Uncertainties occurring through uneven beam-splitter reflections into the analyzer affected the polarization state of the measured data. To eliminate this uncertainty, Mueller matrices for the reflecting optical component were acquired and applied to the Stokes vector of the measured signal to eliminate the polarization change from the beam splitter.

From the acquired Stokes vector over a 5 degree phase range, important parameters such as the circular polarization ratio and linear polarization ratio were calculated. The detector signal phase curves indicated the presence of opposition surge as the backscatter intensity increased at near zero phase angles. Further calculation of the polarization ratios enabled us to differentiate between the two opposition effects. SHOE primarily was a single scattering effect where the CPR was expected to decrease as the phase angle decreased, however due to presence of CBOE the CPR values increased with decreasing phase angle. The presence of CBOE agreed with previous undertaken studies and provided evidence that potential highly reflective ice bearing deposits would have similar occurring phenomenon but more future work on the liquid samples are required.

The fifth research objective was to explore the key variables such as size and size distribution of the scatterers, the number density of the scatterers, the absorption properties of the medium hosting the scatterers, and the absorption properties of the scatterers themselves. Polystyrene beads the size approximately equal to the wavelength of the incident radiation were suspended in a milky liquid solution and the backscatter signal were observed. Specular reflections from the initial contact of the polarized signal with the liquid medium required us to observe the backscatter at large incidence angles. Although the liquid suspension was a low-loss medium, very weak and noisy backscattering signal was observed. The suspended beads in the liquid medium would settle through the polarization measurement procedure which would further affect the repeatability of the measurements. The objectives related to the size distribution of scatterers, absorption properties of the medium and of the scatterers could not be achieved. Future work on preparing a more stable measurement technique for liquid beads is required before the absorption and scattering properties can be calculated.

I accomplished the primary objectives of the research by designing, constructing and re-iterating the design of the polarimeter according to the given objectives. The instrument was validated by measuring the CPR and signal intensity values over 0-5°phase angle region and comparing those values to the Nelson (2000) [37] study. Although the Nelson study used different wavelength compared to my study. I was able to observe similar trends for CPR and intensity values with decreasing phase angle. The trends were also observed for some liquid analog samples suggesting that multiple scattering effects can be studied through this instrument. Future work involving a variety of liquid samples and possibly icy analogs using the MAGI polarimeter would provide more evidence on the behavior of scatters, scattering medium and nature of scatterers.

9 Future Work

Although the results presented here have demonstrated the capability for acquisition of polarized backscatter at near zero phase angles and the presence of opposition effects for highly reflective samples, it can be further improved. Future work for developing two main aspects of the experiment; instrumentation and sample utilization will help improve the understanding for the detection of icy regoliths.

Instrumentation

- The overall time for acquisition of a single Stokes vector for a backscattered signal was >20 minutes, while the acquisition of CPR values over 0-5 degree phase angle were >45 minutes. Future work to integrate and automate the Stokes vector acquisition and Goniometer movement software would help reduce the data acquisition time. This provides sufficient time to prevent the liquid suspension from settling and allow for a stable measurement.

- Signal stability and low signal to noise ratios are believed to be the biggest contributors to uncertainties in the data acquisition procedure. Measuring the stability of the laser for a low intensity signal would help circumvent the uncertainty issues by applying proper corrections. Acquisition of signal over different IR and visible wavelengths would help us understand the effects of wavelength on CPR trends and reflectance values.

- The data points between 1.3-2.2°range could not be acquired due to mounting restrictions on the beam splitter. New approaches for mounting the beam splitter on the arm platform with a 45°rail, would enable acquisition of measurements over 0-5 degree without any setup restrictions. The mounted beam splitter would be able to move along the rail platform but the platform would have to be very precisely mounted as any small deviation in the angle would cause the backscattered signal to miss the analyzer.

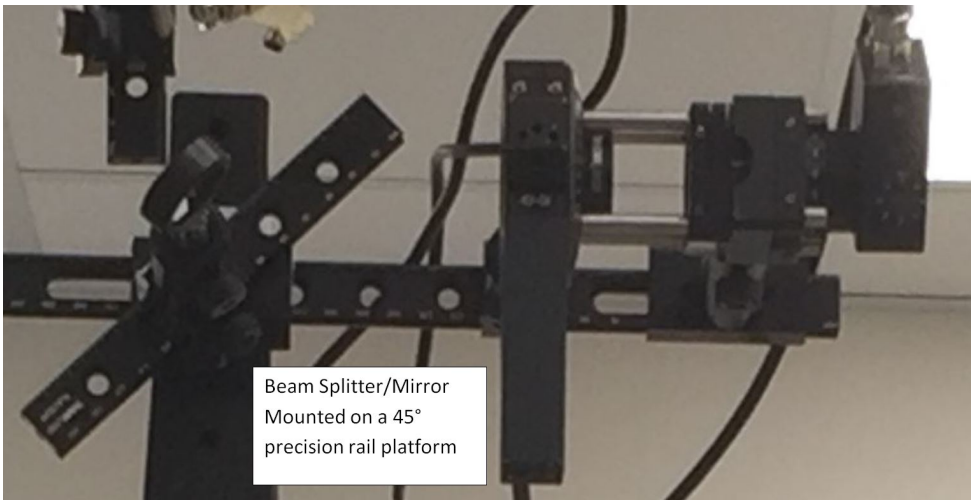

Figure 9.1: New beam splitter mounting technique

Future Samples

- The phase angle measurements were performed for four different highly reflective alumina samples with grain sizes higher, lower and similar to the wavelength of the incident signal. Future data measurements for alumina samples with more diverse set of grain sizes would help develop a complete phase curve map.

- The analogs used for this study were mainly powdered alumina samples and standard Spectralon pucks. To better understand the behaviour of icy regoliths, single sample of aqueous suspension with polystyrene beads from Thermo Fisher Scientific manufacturer [33] and Alumina ($2.1\mu m$)/Glycerol colloidal solution were studied and analyzed at different emergence angles. Future measurements on a variety of suspended bead solutions with different particle sizes in the range of the wavelength of the signal would help understand the behavior of scatterers embedded in low loss medium.

Bibliography

[1] Effects of interaction of electromagnetic waves in complex particles. URL: http://what-when-how.com/electromagnetic-waves.htm [cited 10.05.2018].

[2] Normal probability density function, 2018. URL: https://www.mathworks.com/help/stats/normpdf.html.

[3] E. Akkermans, P. E. Wolf, and R. Maynard. Coherent backscattering of light by disordered media: Analysis of the peak line shape. *Phys. Rev. Lett.*, 56:1471–1474, Apr 1986. URL: https://link.aps.org/doi/10.1103/PhysRevLett.56.1471, doi:10.1103/PhysRevLett.56.1471.

[4] Von Sebastian Arnoldt. Rotating quarter-wave plate stokes polarimeter. 2011. URL: http://quantum-technologies.iap.uni-bonn.de/en/diplom-theses.html?task=download&file=216&token=294e84a6672a486d881880d560973c68.

[5] R. M. A. Azzam. Photopolarimetric measurement of the mueller matrix by fourier analysis of a single detected signal. *Opt. Lett.*, 2(6):148–150, Jun 1978. URL: http://ol.osa.org/abstract.cfm?URI=ol-2-6-148, doi:10.1364/OL.2.000148.

[6] D. Blewett B. Hapke. Coherent backscatter model for the unusual radar reflectivity of icy satellites. *Nature*, 352:46–47, 1991. doi:10.1038/352046a0.

[7] Malvin Carl Teich Bahaa E.A. Saleh. *Polarization and Crystal Optics*. Wiley-Blackwell, 2001. URL: https://onlinelibrary.wiley.com/doi/abs/10.1002/0471213748.ch6, doi:10.1002/0471213748.ch6.

[8] Lance A.M. Benner, Steven J. Ostro, Christopher Magri, Michael C. Nolan, Ellen S. Howell, Jon D. Giorgini, Raymond F. Jurgens, Jean-Luc Margot, Patrick A. Taylor, Michael W. Busch, and Michael K. Shepard. Near-earth asteroid surface roughness depends on compositional class. *Icarus*, 198(2):294 – 304, 2008. URL: http://www.sciencedirect.com/science/article/pii/S0019103508002522, doi:https://doi.org/10.1016/j.icarus.2008.06.010.

[9] Bryan J. Butler, Duane O. Muhleman, and Martin A. Slade. Mercury: full-disk radar images and the detection and stability of ice at the north pole. *Journal of Geophysical Research: Planets*, 98(E8):15003–15023, 1993. URL: http://dx.doi.org/10.1029/93JE01581, doi:10.1029/93JE01581.

[10] B.A. Campbell. *Radar Remote Sensing of Planetary Surfaces*. Cambridge University Press, 2002.

[11] Bruce A. Campbell, Lynn M. Carter, Donald B. Campbell, Michael Nolan, John Chandler, Rebecca R. Ghent, B. Ray Hawke, Ross F. Anderson, and Kassandra Wells. Earth-based 12.6-cm wavelength radar mapping of the moon: New views of impact melt distribution and mare physical properties. *Icarus*, 208(2):565 – 573, 2010. URL: http://www.sciencedirect.com/science/article/pii/S0019103510001132, doi:https://doi.org/10.1016/j.icarus.2010.03.011.

[12] Bruce A. Campbell, B. R. Hawke, and Donald B. Campbell. Surface morphology of domes in the marius hills and mons rümker regions of the moon from earth-based radar data. *Journal of Geophysical Research: Planets*, 114(E1):n/a–n/a, 2009. E01001. URL: http://dx.doi.org/10.1029/2008JE003253, doi:10.1029/2008JE003253.

[13] L. M. Carter, D. B. Campbell, and B. A. Campbell. Geologic studies of planetary surfaces using radar polarimetric imaging. *Proceedings of the IEEE*, 99(5):770–782, May 2011. doi:10.1109/JPROC.2010.2099090.

[14] S. Chandrasekhar. *Radiative Transfer*. Dover Books on Physics. Dover Publications, 2013. URL: https://books.google.ca/books?id=1YHCAgAAQBAJ.

[15] Les Cowley. Shadow hiding. URL: https://www.atoptics.co.uk/fz481.htm [cited 10.05.2018].

[16] Wenzhe Fa and Yuzhen Cai. Circular polarization ratio characteristics of impact craters from mini-rf observations and implications for ice detection at the polar regions of the moon. *Journal of Geophysical Research: Planets*, 118(8):1582–1608, 2013. URL: http://dx.doi.org/10.1002/jgre.20110, doi:10.1002/jgre.20110.

[17] Wenzhe Fa, Mark A. Wieczorek, and Essam Heggy. Modeling polarimetric radar scattering from the lunar surface: Study on the effect of physical properties of the regolith layer. *Journal of Geophysical Research: Planets*, 116(E3). URL: https://agupubs.onlinelibrary.wiley.com/doi/abs/10.1029/2010JE003649, arXiv:https://agupubs.onlinelibrary.wiley.com/doi/pdf/10.1029/2010JE003649, doi:10.1029/2010JE003649.

[18] T. Gehrels. Photometric Studies of Asteroids. V. The Light-Curve and Phase Function of 20 Massalia. *Astrophysics Journal*, 123:331, March 1956. doi:10.1086/146166.

[19] Rebecca R. Ghent, Bruce A. Campbell, B. Ray Hawke, and Donald B. Campbell. Earth-based radar data reveal extended deposits of the moon's orientale basin. *Geology*, 36(5):343, 2008. URL: +http://dx.doi.org/10.1130/G24325A.1, arXiv:/gsw/content_public/journal/geology/36/5/10.1130_g24325a.1/3/i0091-7613-36-5-343.pdf, doi:10.1130/G24325A.1.

[20] Dennis H. Goldstein. Mueller matrix dual-rotating retarder polarimeter. *Appl. Opt.*, 31(31):6676–6683, Nov 1992. URL: http://ao.osa.org/abstract.cfm?URI=ao-31-31-6676, doi:10.1364/AO.31.006676.

[21] K. A. Hameen-Anttila and S. Pyykko. Photometric Behaviour of Saturn's Rings as a Function of the Saturn ocentric Latitudes of the Earth and the Sun. *Astronomy and Astrophysics*, 19:235, July 1972.

[22] B. Hapke, D. Dimucci, R. Nelson, and W. Smythe. The Nature of the Opposition Effect in Frost, Vegetation and Soils. In *Lunar and Planetary Science Conference*, volume 27 of *Lunar and Planetary Science Conference*, March 1996.

[23] Bruce Hapke. Coherent backscatter and the radar characteristics of outer planet satellites. *Icarus*, 88(2):407 – 417, 1990. URL: http://www.sciencedirect.com/science/article/pii/001910359090091M, doi:https://doi.org/10.1016/0019-1035(90)90091-M.

[24] Bruce W. Hapke, Robert M. Nelson, and William D. Smythe. The opposition effect of the moon: The contribution of coherent backscatter. *Science*, 260(5107):509–511, 1993. URL: http://science.sciencemag.org/content/260/5107/509, arXiv:http://science.sciencemag.org/content/260/5107/509.full.pdf, doi:10.1126/science.260.5107.509.

[25] K. Ichimoto, K. Shinoda, T. Yamamoto, and J. Kiyohara. Photopolarimetric measurement system of Mueller matrix with dual rotating waveplates. *Publications of the National Astronomical Observatory of Japan*, 9:11–19, 2006.

[26] Least Squares Interpolation. 1d interpolation. URL: https://www.mathworks.com/help/matlab/ref/interp1.html#btwp6lt-1-x.

[27] M. A. Janssen, A. Le Gall, and L. C. Wye. Anomalous radar backscatter from Titan's surface? *Icarus*, 212:321–328, March 2011. doi:10.1016/j.icarus.2010.11.026.

[28] B. Jost, A. Pommerol, O. Poch, B. Gundlach, M. Leboeuf, M. Dadras, J. Blum, and N. Thomas. Experimental characterization of the opposition surge in fine-grained water–ice and high albedo ice analogs. *Icarus*, 264:109

– 131, 2016. URL: http://www.sciencedirect.com/science/article/pii/S001910351500425X, doi:https://doi.org/10.1016/j.icarus.2015.09.020.

[29] Dissanska M Levesque M.P. "measurement and modeling of the spectralon™ spectro-polarimetric bidirectional reflectance distribution function (brdf)", 2016.

[30] Michael Light. Opposition effects, 2002. URL: https://www.atoptics.co.uk/atoptics/oppos1.htm [cited 10.05.2018].

[31] P. G. Lucey, G. A. Neumann, M. A. Riner, E. Mazarico, D. E. Smith, M. T. Zuber, D. A. Paige, D. B. Bussey, J. T. Cahill, A. McGovern, P. Isaacson, L. M. Corley, M. H. Torrence, H. J. Melosh, J. W. Head, and E. Song. The global albedo of the moon at 1064 nm from lola. *Journal of Geophysical Research: Planets*, 119(7):1665–1679, 2014. 2013JE004592. URL: http://dx.doi.org/10.1002/2013JE004592, doi:10.1002/2013JE004592.

[32] R. Magnusson. *Mueller matrix ellipsometry studies of nanostructured materials:*. Linköping Studies in Science and Technology. Dissertations. Linköping University Electronic Press, 2014. URL: https://books.google.ca/books?id=FoxUBQAAQBAJ.

[33] Thermo Fisher Scientific Manufactures. Microspheres. URL: https://www.thermofisher.com/ca/en/home.html.

[34] M. I. Mishchenko. The angular width of the coherent back-scatter opposition effect: An application to icy outer planet satellites. *Astrophysics and Space Science*, 194(2):327–333, Aug 1992. URL: https://doi.org/10.1007/BF00644001, doi:10.1007/BF00644001.

[35] M.I. Mishchenko, V.K. Rosenbush, and N.N. Kiselev. *Polarimetric Remote Sensing of Solar System Objects*. Akademperiodika, 2010. URL: https://books.google.ca/books?id=yKBltAEACAAJ.

[36] DUANE O. MUHLEMAN, BRYAN J. BUTLER, ARIE W. GROSSMAN, and MARTIN A. SLADE. Radar images of mars. *Science*, 253(5027):1508–1513, 1991. URL: http://science.sciencemag.org/content/253/5027/1508, arXiv:http://science.sciencemag.org/content/253/5027/1508.full.pdf, doi:10.1126/science.253.5027.1508.

[37] R.M. Nelson, B.W. Hapke, W.D. Smythe, and L.J. Spilker. The opposition effect in simulated planetary regoliths. reflectance and circular polarization ratio change at small phase angle. *Icarus*, 147(2):545 – 558, 2000. URL: http://www.sciencedirect.com/science/article/pii/S0019103500964546, doi:https://doi.org/10.1006/icar.2000.6454.

[38] Robert M Nelson, William D Smythe, Bruce W Hapke, and Amy S Hale. Low phase angle laboratory studies of the opposition effect: search for wavelength dependence. *Planetary and Space Science*, 50(9):849 – 856, 2002. Space Related Laboratory Investigation: Materials, environments a nd life. URL: http://www.sciencedirect.com/science/article/pii/S0032063302000594, doi:https://doi.org/10.1016/S0032-0633(02)00059-4.

[39] S. Nozette, C. L. Lichtenberg, P. Spudis, R. Bonner, W. Ort, E. Malaret, M. Robinson, and E. M. Shoemaker. The clementine bistatic radar experiment. *Science*, 274(5292):1495–1498, 1996. URL: http://science.sciencemag.org/content/274/5292/1495, arXiv:http://science.sciencemag.org/content/274/5292/1495.full.pdf, doi:10.1126/science.274.5292.1495.

[40] S. J. Ostro, D. B. Campbell, R. A. Simpson, R. S. Hudson, J. F. Chandler, K. D. Rosema, I. I. Shapiro, E. M. Standish, R. Winkler, D. K. Yeomans, R. Velez, and R. M. Goldstein. Europa, ganymede, and callisto: New radar results from arecibo and goldstone. *Journal of Geophysical Research: Planets*, 97(E11):18227–18244, 1992. URL: http://dx.doi.org/10.1029/92JE01992, doi:10.1029/92JE01992.

[41] David A. Paige, Matthew A. Siegler, John K. Harmon, Gregory A. Neumann, Erwan M. Mazarico, David E. Smith, Maria T. Zuber, Ellen Harju, Mona L. Delitsky, and Sean C. Solomon. Thermal stability of volatiles in the north polar region of mercury. *Science*, 339(6117):300–303, 2013. URL: http://science.sciencemag.org/content/339/6117/300, arXiv:http://science.sciencemag.org/content/339/6117/300.full.pdf, doi:10.1126/science.1231106.

[42] Jennifer Lynn Piatek. Size-dependent scattering properties of planetary regolith analogs. December 2003. URL: http://d-scholarship.pitt.edu/7875/.

[43] M. R. Chipman, Bass and Optical Society of America. *Handbook of optics*. Number v. 1-2 in Handbook of Optics. McGraw-Hill, 2001. URL: https://books.google.ca/books?id=owg6AQAAIAAJ.

[44] B. W. Hapke K. S. Manatt D. O. Kroner W. D. Smythe R. M. Nelson, M. D. Boryta. Photometric properties of candidate planetary surface regolith materials at small phase angle: Relevance to small bodies in the outer solar system. *Lunar and Planetary Science Conference*, pages 2584–2585, 2015. URL: https://www.hou.usra.edu/meetings/lpsc2015/pdf/2584.pdf.

[45] R. K. Raney, P. D. Spudis, B. Bussey, J. Crusan, J. R. Jensen, W. Marinelli, P. McKerracher, C. Neish, M. Palsetia, R. Schulze, H. B. Sequeira, and H. Winters. The lunar mini-rf radars: Hybrid polarimetric architecture and initial results. *Proceedings of the IEEE*, 99(5):808–823, May 2011. doi:10.1109/JPROC.2010.2084970.

[46] Matthew H. Smith. Optimization of a dual-rotating-retarder mueller matrix polarimeter. *Appl. Opt.*, 41(13):2488–2493, May 2002. URL: http://ao.osa.org/abstract.cfm?URI=ao-41-13-2488, doi:10.1364/AO.41.002488.

[47] P. D. Spudis, D. B. J. Bussey, S. M. Baloga, J. T. S. Cahill, L. S. Glaze, G. W. Patterson, R. K. Raney, T. W. Thompson, B. J. Thomson, and E. A. Ustinov. Evidence for water ice on the moon: Results for anomalous polar craters from the lro

mini-rf imaging radar. *Journal of Geophysical Research: Planets*, 118(10):2016–2029, 2013. URL: http://dx.doi.org/10.1002/jgre.20156, doi:10.1002/jgre.20156.

[48] N. J. S. Stacy, D. B. Campbell, and P. G. Ford. Arecibo radar mapping of the lunar poles: A search for ice deposits. *Science*, 276(5318):1527–1530, 1997. URL: http://science.sciencemag.org/content/276/5318/1527, arXiv:http://science.sciencemag.org/content/276/5318/1527.full.pdf, doi:10.1126/science.276.5318.1527.

[49] Øyvind Svensen, Morten Kildemo, Jerome Maria, Jakob J. Stamnes, and Øyvind Frette. Mueller matrix measurements and modeling pertaining to spectralon white reflectance standards. *Opt. Express*, 20(14):15045–15053, Jul 2012. URL: http://www.opticsexpress.org/abstract.cfm?URI=oe-20-14-15045, doi:10.1364/OE.20.015045.

[50] A. Virkki, K. Muinonen, and A. Penttilä. Circular-Polarization Ratios and Radar Albedos: Interpretation in Terms of Near-Surface Physical Properties of Asteroids. In *Asteroids, Comets, Meteors 2012*, volume 1667 of *LPI Contributions*, page 6064, May 2012.

Appendices

Appendix A: **Experimental Setup**

The schematic and table below shows the distances between the optical components on the long arm goniometric instrument.

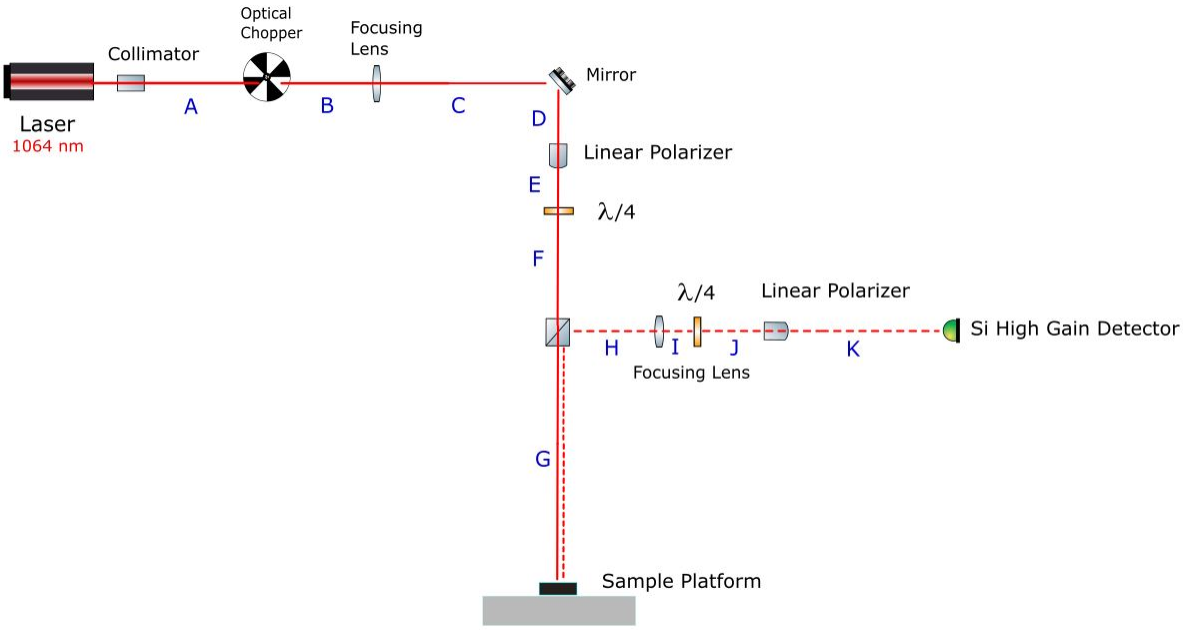

Figure A.1: Optical Instrument Setup Schematic

Measurements			
Distance	Value	Distance	Value
A	86.25 ± 1 mm	G	798 ± 1 mm
B	112.2 ± 1 mm	H	76.15 ± 1 mm
C	93.25 ± 1 mm	I	18.7 ± 1 mm
D	37 ± 1 mm	J	58.45 ± 1 mm
E	35.5 ± 1 mm	K	205 ± 1 mm
F	54.35 ± 1 mm		

Table A.1: Distance between the optical components in the polarimeter assembly

Appendix B: **Stokes and Mueller Matrix Computation Code**

The program below was written in Matlab programming language. From the experimental rotating quarter wave plate technique the intensity values were measured in an excel spreadsheet. The values are inserted into the program which then computes the stokes parameters of the measured signal. Additional parameters such as same circular signal, opposite circular signal and the circular polarization ratio are computed as well. The user can call the program as a function every time the Stokes vector needs to be computed.

```
1  %% Optical Studies of Icy Analogs using Near Zero Phase Angle
       Measurements
2  % Stokes Parameters Computation
3  % by Mrunal Amin
4
5  %% Input the Intensity data from Rotating Quarter Wave Plate
       Technique
6  user_input = input('Enter the Intensity values from RQWP
       Technique:\n', 's');
7  user = user_input;
8  user_input2 = input('Enter sheet number:\n', 's');
9  sheet = str2double(user_input2);
10 xlRange = 'B2:B74';
11
12 data = xlsread(user, sheet, xlRange);
13
```

```
14 angle = 0:5:360; %Rotation Angle of QWP
15 radians = (angle(1,:)*pi)/180.0;
16
17 %% Fourier Coefficients A,B,C and D
18 A = 0;
19 for i = 1:73
20     A = A + data(i,1);
21 end
22 A = (A * radians(1,2))/pi;
23
24 B = 0;
25 for j = 1:73
26     B = B + (data(j,1)*sin(2*radians(1,j)));
27 end
28 B = (B * radians(1,2))*(2/pi);
29
30 C = 0;
31 for m = 1:73
32     C = C + (data(m,1)*cos(4*radians(1,m)));
33 end
34 C = (C * radians(1,2))*(2/pi);
35
36 D = 0;
37 for n = 1:73
38     D = D + (data(n,1)*sin(4*radians(1,n)));
39 end
40 D = (D * radians(1,2))*(2/pi);
41
```

```
42 %% Computing Stokes parameters
43 s0 = A-C;
44 s1 = 2*C;
45 s2 = 2*D;
46 s3 = B;
47
48 % Normalizing Stokes parameters
49 S0 = s0/s0;
50 S1 = s1/s0;
51 S2 = s2/s0;
52 S3 = s3/s0;
53
54 % Plotting the measured intensity as a function of QWP angle
55 figure;
56 plot(angle, data, 'b-o');
57 xlabel('Angle(Degrees)');
58 ylabel('Intensity(V)');
59 title('Intensity vs  Quarter Wave Plate Angle');
60 grid on
61
62 %% Computing the CPR value
63
64 OC = (S0-S3);
65 SC = (S0+S3);
66
67 CPR = (SC)/(OC);
68
69 %% Stokes parameters output
```

```
70 str = {'Stokes Parameters: ';...
71       ['S0 = ' num2str(S0)];...
72       ['S1 = ' num2str(S1)];...
73       ['S2 = ' num2str(S2)];...
74       ['S3 = ' num2str(S3)];...
75       ['CPR = ', num2str(CPR)]};
76 msgbox(str);
```

Using the dual rotating quarter wave plate technique the intensity values were recorded in an excel spreadsheet. The excel file was inserted into the Mueller matrix computation program which evaluates the Fourier coefficients and calculates the Mueller matrix values. Alignment and quarter-wave plate error correction can be applied to the computed Mueller matrix by calculating the five error values through a non-sample calibration technique. The displayed Mueller matrix parameters are corrected for known errors in retardance and errors caused by the inability to align the polarizing elements precisely.

```
1 %% Mueller Matrix Calculations
2 % by Mrunal Amin
3 %
4 angle = 0:5:175; % Rotation angle
5 % Creating a 36x25 matrix with each row representing fast axis
     of first
6 % quarter wave plate
7 x = zeros(36,25);
8 x(:,1) = 1;
9 y = 2:2:24;
10 for i = 1:36
11       for j = 2:13
12           x(i,j) = cosd(y(1,j-1)*angle(1,i));
13       end
```

```
14 end
15 for i = 1:36
16     for j = 14:25
17         x(i,j) = sind(y(1,j-13)*angle(1,i));
18     end
19 end
20 % Transpose of the x matrix
21 x_t = transpose(x);
22
23 % Resulting matrix of X transpose and X multiplication
24 r1 = zeros(25,25);
25 for i = 1:25
26     for j = 1:25
27         r1(i,j) = x_t(i,:)*x(:,j);
28     end
29 end
30 r11 = x_t*x;
31
32 % Inverse of the resulting matrix
33 zx = inv(r11);
34 z = inv(r1);
35
36 r2 = zeros(25,36);
37 for i = 1:25
38     for j = 1:36
39         r2(i,j) = z(i,:)*x_t(:,j);
40     end
41 end
```

```
42 r22 = (zx*x_t);
43
44 % Reading the intensity values from the Dual Rotating Quarter
       Wave
45 % Plate Method
46 user_input = input('Enter the Intensity values from DRQWP
       Technique:\n', 's');
47 filename = user_input;
48 user_input2 = input('Enter sheet number:\n', 's');
49 sheet = str2double(user_input2); %6
50 xlRange = 'B3:B38';
51
52 I = xlsread(filename, sheet, xlRange);
53
54
55
56 %% Fourier Coefficients matrix
57 % a=zeros(25,1);
58 % for i = 1:25
59 %     a(i,1) = r2(i,:)*I(:,1);
60 % end
61 a = (r22*I)'; % Simpler method compared to loop
62 %a = a';
63
64 b = zeros(1,12);
65 for j = 14:25
66     b(1,j-13) = a(1,j);
67 end
```

```
68
69
70 % Obtaining Mueller components from the Fourier Coefficients
71 m11 = a(1,1)-a(1,3)+a(1,9)-a(1,11)+a(1,13);
72 m12 = 2*a(1,3) - 2*a(1,9) - 2*a(1,13);
73 m13 = 2*b(1,2)+2*b(1,8)-2*b(1,12);
74 m14 = b(1,1)-2*b(1,11);
75 m14x = b(1,1)+2*b(1,9);
76 m14x2 = b(1,1)+b(1,9)-b(1,11);
77 m21 = -2*a(1,9)+2*a(1,11)-2*a(1,13);
78 m22 = 4*a(1,9)+4*a(1,13);
79 m23 = -4*b(1,8)+4*b(1,12);
80 m24 = 2*(-1*b(1,9)+b(1,11));
81 m24x = -4*b(1,9);
82 m24x2 = 4*b(1,11);
83 m31 = -2*b(1,8)+2*b(1,10)-2*b(1,12);
84 m32 = 4*b(1,8)+4*b(1,12);
85 m33 = 4*a(1,9)-4*a(1,13);
86 m34 = 4*a(1,10);
87 m34x = -4*a(1,12);
88 m34x2 = 2*(a(1,10)-a(1,12));
89 m41 = 2*b(1,3)-b(1,5);
90 m41x = b(1,3)-b(1,5)+b(1,7);
91 m41x2 = -1*b(1,5)+2*b(1,7);
92 m42 = -4*b(1,7);
93 m42x = -4*b(1,3);
94 m42x2 = -2*(b(1,3)+b(1,7));
95 m43 = -4*a(1,4);
```

```
96 m43x = 4*a(1,8);
97 m43x2 = 2*(-1*a(1,4)+ a(1,8));
98 m44 = -2*a(1,5);
99 m44x = 2*a(1,7);
100 m44x2 = a(1,7)-a(1,5);
101
102 % Creating Mueller Matrix from the computed components
103 Mu = zeros(4,4);
104 Mu(1,1) = m11;
105 Mu(1,2) = m12;
106 Mu(1,3) = m13;
107 Mu(1,4) = m14;
108 Mu(2,1) = m21;
109 Mu(2,2) = m22;
110 Mu(2,3) = m23;
111 Mu(2,4) = m24;
112 Mu(3,1) = m31;
113 Mu(3,2) = m32;
114 Mu(3,3) = m33;
115 Mu(3,4) = m34;
116 Mu(4,1) = m41;
117 Mu(4,2) = m42;
118 Mu(4,3) = m43;
119 Mu(4,4) = m44x;
120 print('Non-normalized Mueller Matrix = ', Mu)
121 %% Inserting the mueller components into an M matrix and
      Normalizing
122 % with first parameter
```

```
123 M = zeros(4,4);
124 M(1,1) = m11/m11;
125 M(1,2) = m12/m11;
126 M(1,3) = m13/m11;
127 M(1,4) = m14/m11;
128 M(2,1) = m21/m11;
129 M(2,2) = m22/m11;
130 M(2,3) = m23/m11;
131 M(2,4) = m24/m11;
132 M(3,1) = m31/m11;
133 M(3,2) = m32/m11;
134 M(3,3) = m33/m11;
135 M(3,4) = m34/m11;
136 M(4,1) = m41/m11;
137 M(4,2) = m42/m11;
138 M(4,3) = m43/m11;
139 M(4,4) = m44x/m11;
140 % Outputting the result on the command window
141  print('Mueller Matrix = ', M)
142 MR = M;
143
144 %% Error Calculation
145 % Computation for no-sample error calibration
146 % e1 = 3 - 8*(a(1,1) + a(1,11));
147 % disp(['Retardation Error for QWP1 E1: ',num2str(e1)])
148 %
149 % num = (4*(a(1,1)-a(1,11))) - 1;
150 % den = 1 - (4*(a(1,1)-a(1,11)));
```

```
151 % e2 = num/den;
152 % e2x = 8*(a(1,9)+a(1,11))-1;
153 % disp(['Retardation Error for QWP2 E2: ',num2str(e2)])
154 %
155 % e3 = -2*(b(1,4) + b(1,6));
156 % disp(['Orientation Error for QWP1 E3: ',num2str(e3)])
157 %
158 % e5 = ((8*b(1,2))/((1+e1)*(1-e2)))+(2*e3);
159 % disp(['Orientation Error for LP2 E5: ',num2str(e5)])
160 %
161 % e4 = e5 + (2*(b(1,1)-b(1,6)));
162 % disp(['Orientation Error for LP2 E4: ',num2str(e4)])
163 %
164 % Computed errors
165 e1 = -1.2574;
166 e2 = -1;
167 e3 = 0.17395;
168 e4 = -0.2566;
169 e5 = -0.31704;
170
171
172 %% Error Compensation
173 disp(['A(1,1)', num2str(a(1,1))]);
174 a(1,1) = 1/4 + (((1-e1)*(1-e2))/16);
175 disp(['A(1,1) corrected ', num2str(a(1,1))]);
176
177 disp(['A(1,2)', num2str(a(1,3))]);
178 a(1,3) = ((1+e1)*(1-e2)/16)+((1+e1)*(1-e2)*e3*e5)/2;
```

```
179 disp(['A(1,2) corrected ', num2str(a(1,3))]);
180
181 disp(['A(1,8)', num2str(a(1,9))]);
182 a(1,9) = (1+e1)*(1+e2)/16;
183 disp(['A(1,8) corrected ', num2str(a(1,9))]);
184
185
186 disp(['A(1,10)', num2str(a(1,11))]);
187 a(1,11) = (1-e1)*(1+e2)/16;
188 disp(['A(1,10) corrected ', num2str(a(1,11))]);
189
190 disp(['B(1,4)', num2str(b(1,4))]);
191 b(1,4) = (e4-e3-e5)/4;
192 disp(['B(1,4) corrected ', num2str(b(1,4))]);
193
194 disp(['B(1,6)', num2str(b(1,6))]);
195 b(1,6) = (e5-e3-e4)/4;
196 disp(['B(1,6) corrected ', num2str(b(1,6))]);
197
198 disp(['B(1,8)', num2str(b(1,8))]);
199 b(1,8) = ((1+e1)*(1+e2)*(2*e4 - 2*e3-e5))/8;
200 disp(['B(1,8) corrected ', num2str(b(1,8))]);
201
202 disp(['B(1,2)', num2str(b(1,2))]);
203 b(1,2) = -(((1+e1)*(1-e2)*e3)/4) + (((1+e1)*(1-e2)*e5)/8);
204 disp(['B(1,2) corrected ', num2str(b(1,2))]);
205
206 disp(['B(1,10)', num2str(b(1,10))]);
```

```
207 b(1,10) = -((1-e1)*(1+e2)*((2*e4)-e5))/8;
208 disp(['B(1,10) corrected ', num2str(b(1,10))]);
209
210 %% Obtaining Error Compensated Mueller components from
211 % the new Fourier Coefficients
212 m11 = a(1,1)-a(1,3)+a(1,9)-a(1,11)+a(1,13);
213 m12 = 2*a(1,3) - 2*a(1,9) - 2*a(1,13);
214 m13 = 2*b(1,2)+2*b(1,8)-2*b(1,12);
215 m14 = b(1,1)-2*b(1,11);
216 m14x = b(1,1)+2*b(1,9);
217 m14x2 = b(1,1)+b(1,9)-b(1,11);
218 m21 = -2*a(1,9)+2*a(1,11)-2*a(1,13);
219 m22 = 4*a(1,9)+4*a(1,13);
220 m23 = -4*b(1,8)+4*b(1,12);
221 m24 = 2*(-1*b(1,9)+b(1,11));
222 m24x = -4*b(1,9);
223 m24x2 = 4*b(1,11);
224 m31 = -2*b(1,8)+2*b(1,10)-2*b(1,12);
225 m32 = 4*b(1,8)+4*b(1,12);
226 m33 = 4*a(1,9)-4*a(1,13);
227 m34 = 4*a(1,10);
228 m34x = -4*a(1,12);
229 m34x2 = 2*(a(1,10)-a(1,12));
230 m41 = 2*b(1,3)-b(1,5);
231 m41x = b(1,3)-b(1,5)+b(1,7);
232 m41x2 = -1*b(1,5)+2*b(1,7);
233 m42 = -4*b(1,7);
234 m42x = -4*b(1,3);
```

```
m42x2 = -2*(b(1,3)+b(1,7));
m43 = -4*a(1,4);
m43x = 4*a(1,8);
m43x2 = 2*(-1*a(1,4)+ a(1,8));
m44 = -2*a(1,5);
m44x = 2*a(1,7);
m44x2 = a(1,7)-a(1,5);
%% Normalization
Mu = zeros(4,4);
Mu(1,1) = m11;
Mu(1,2) = m12;
Mu(1,3) = m13;
Mu(1,4) = m14;
Mu(2,1) = m21;
Mu(2,2) = m22;
Mu(2,3) = m23;
Mu(2,4) = m24;
Mu(3,1) = m31;
Mu(3,2) = m32;
Mu(3,3) = m33;
Mu(3,4) = m34;
Mu(4,1) = m41;
Mu(4,2) = m42;
Mu(4,3) = m43;
Mu(4,4) = m44;
print('Non-Normalized Error Compensated Mueller Matrix = ',Mu)
%% Inserting the mueller components into an M matrix
M = zeros(4,4);
```

```
M(1,1) = m11/m11;
M(1,2) = m12/m11;
M(1,3) = m13/m11;
M(1,4) = m14/m11;
M(2,1) = m21/m11;
M(2,2) = m22/m11;
M(2,3) = m23/m11;
M(2,4) = m24/m11;
M(3,1) = m31/m11;
M(3,2) = m32/m11;
M(3,3) = m33/m11;
M(3,4) = m34/m11;
M(4,1) = m41/m11;
M(4,2) = m42/m11;
M(4,3) = m43/m11;
M(4,4) = m44/m11;
% Outputting the result on the command window
print('Normalized Error Compensated Mueller Matrix = ', M);
```

This function performs the Mueller matrix correction for the known CPR vs phase angle datasets of analog samples. The program uses Stokes vector of the entire dataset over 0-5 degree phase angles to compute the corrected Stokes vector from which CPR values are calculated. Mueller matrix parameters are used from the previous Mueller matrix computation program while Stokes vectors are acquired from the Stokes vector computation program. [39]

```
%% Mueller Matrix Correction Program
% by Mrunal Amin

% Function takes Mueller Matrix of the optical element to be
```

```
    corrected
% CPR and their respective phase angle values
function [CPRN] = MMcorrection(MM, angle, CPR)

S4 = zeros(length(angle),1);

for k = 1:length(angle)
    S4(k,1) = (1-CPR(k,1))/(1+CPR(k,1));
end

% Multiplying the inverse of Mueller matrix with output Stokes
    vector
% results in input Stokes vector
RS = zeros(length(angle),4);
for j = 1:length(angle)
    RS(j,:) = inv(MM)*[1; 0.3*S4(j,1); 0.3*S4(j,1); S4(j,1)];
end

RX = zeros(length(angle),4);
for b = 1:length(angle)
     RX(b,:) = RS(b,:)/RS(b,1);
end

% New corrected CPR values
CPRN = zeros(length(angle),1);
for l = 1:length(angle)
    CPRN(l,1) = (RX(l,1) + RX(l,4))/(RX(l,1)- RX(l,4));
end
```

```
31 end
```

```
1 % Fitting a curve to the missing data points by method of least
      squares
2 % Least Squares
3 function [LS] = LeastSquaresFit(ang, dataX, xq)
4
5 % Taking 5 meas values before and after to get the Least Squares
       Regression
6 %   Detailed explanation goes here
7 Y = dataX';
8 X = ang';
9 H=[];
10 % N states the order of the expression evaluated
11 N = 5;
12 for i = 0:N
13     H = [H,X.^i];
14 end
15 % H = [ones(length(Y),1),X,X.^2, X.^3);
16 Astar = inv(H'*H)*H'*Y;
17
18 Ytilde = H*Astar;
19
20 % R prints the residual
21 R = sum((Y-Ytilde).^2);
22 LS = interp1(X, Ytilde, xq, 'poly5', 'extrap');
23 end
```